



Pulsational Pair-instability Supernovae

S. E. Woosley

Department of Astronomy and Astrophysics, University of California, Santa Cruz, CA 95064, USA; woosley@ucolick.org

Received 2016 August 31; revised 2016 December 29; accepted 2017 January 5; published 2017 February 24

Abstract

The final evolution of stars in the mass range $70\text{--}140 M_{\odot}$ is explored. Depending upon their mass loss history and rotation rates, these stars will end their lives as pulsational pair-instability supernovae (PPISN) producing a great variety of observational transients with total durations ranging from weeks to millennia and luminosities from 10^{41} to over $10^{44} \text{ erg s}^{-1}$. No nonrotating model radiates more than $5 \times 10^{50} \text{ erg}$ of light or has a kinetic energy exceeding $5 \times 10^{51} \text{ erg}$, but greater energies are possible, in principle, in magnetar-powered explosions, which are explored. Many events resemble SNe Ibn, SNe Icn, and SNe IIIn, and some potential observational counterparts are mentioned. Some PPISN can exist in a dormant state for extended periods, producing explosions millennia after their first violent pulse. These dormant supernovae contain bright Wolf–Rayet stars, possibly embedded in bright X-ray and radio sources. The relevance of PPISN to supernova impostors like Eta Carinae, to superluminous supernovae, and to sources of gravitational radiation is discussed. No black holes between 52 and $133 M_{\odot}$ are expected from stellar evolution in close binaries.

Key words: stars: black holes – stars: evolution – gravitational waves – hydrodynamics – nuclear reactions, nucleosynthesis, abundances – supernovae: general

1. Introduction

For helium cores more massive than about $30 M_{\odot}$, post-carbon-burning stages are, initially at least, unstable (Woosley et al. 2007; Woosley & Heger 2015a, p. 199). The production of electron–positron pairs at high entropy and temperatures over about $7 \times 10^8 \text{ K}$ softens the equation of state, reducing the structural adiabatic index below 4/3. Roughly speaking, the creation of the rest mass of the pairs takes energy that might have gone into providing pressure support. A contraction to a higher temperature does not encounter as much resistance as it might have otherwise, and the star becomes unstable. This is the “pair-instability” (Fowler & Hoyle 1964; Barkat et al. 1967; Rakavy & Shaviv 1967).

This instability results in a dynamical implosion of the helium and heavy element core which, provided the mass of that core does not exceed $133 M_{\odot}$, is reversed by nuclear burning (Heger & Woosley 2002). Within this range of presupernova helium core masses, $30\text{--}133 M_{\odot}$, which corresponds to a larger, less certain range of main-sequence mass of roughly $70\text{--}260 M_{\odot}$, ignoring rotation, a diverse range of outcomes is expected. Helium cores above about $64 M_{\odot}$ experience a single violent pulse that disrupts the entire star as a “pair-instability supernova” (PISN). These events have been well studied (e.g., Ober et al. 1983; Bond et al. 1984; Glatzel et al. 1985; Heger & Woosley 2002; Umeda & Nomoto 2002; Scannapieco et al. 2005; Kasen et al. 2011), in part because they are easy to simulate. Unlike iron core-collapse supernovae, the explosion mechanism is well understood and easily calculated in 1D. The major uncertainties lie instead with the formation and evolution of the progenitor stars.

Less well studied are the “pulsational pair-instability supernovae” (PPISN) powered by the “pulsational pair-instability” (PPI). Here, the nuclear flashes are not sufficiently energetic to disrupt the entire star. Instead a series of pulsations occurs. The core contracts, ignites burning, typically of oxygen or silicon, expands and cools, then contracts and ignites burning again, either on a hydrodynamic timescale in low-mass cores or on a

Kelvin–Helmholtz timescale in higher-mass ones. In the Kelvin–Helmholtz case, pulses, followed by cooling by radiation and neutrino emission, recur until the mass and entropy of the helium and heavy element remnant are reduced sufficiently to avoid the PPI. As a result, the final core masses converge on a relatively narrow range of values in the range roughly $35\text{--}50 M_{\odot}$. These remnants complete their lives, finishing silicon burning in hydrostatic equilibrium with no further pulsing activity and mass ejection. The duration of activity, from the onset of pulsations until the iron core collapses, can span many orders of magnitude, from a few hours to 10,000 yr.

Though PPISN have also been extensively studied (Barkat et al. 1967; Woosley & Weaver 1986; Heger & Woosley 2002; Woosley et al. 2007; Chatzopoulos & Wheeler 2012; Chen et al. 2014; Woosley & Heger 2015a, Yoshida et al. 2016), these studies have not been as thorough and systematic as for PISN, and there is some confusion about how these explosions might appear. They certainly are not all superluminous. Very few light curves of pure PPISN (i.e., PPISN without an artificial core explosion) have been calculated, except for the $110 M_{\odot}$ model of Woosley et al. (2007), for example, Blinnikov (2010), or parameterized representations thereof (Moriya et al. 2013). Other studies of light curves have considered only bare helium cores (Woosley & Heger 2015a) or assumed parameterized core explosions to calculate light curves (Yoshida et al. 2016). The latter violates the common assumption (which may be wrong; Section 8) that the cores of stars that experience the PPI do not explode but collapse into black holes. The recent discovery of gravitational radiation from merging intermediate-mass black holes (Abbott et al. 2016b) has also heightened interest in the evolution of stars in this mass range (Woosley 2016) and offers new insights into their deaths.

The present paper addresses these issues. The focus is on PPISN in metal-poor stars ($10\% Z_{\odot} = 1.6 \times 10^{-3}$), primarily as a way of suppressing but not eliminating mass loss in the presupernova star. The key quantities of a PPISN progenitor are the mass of its helium and heavy element core and the mass

and radius of its hydrogen envelope, if any, when the star first encounters the PPI at central carbon depletion. Various choices of uncertain mass loss rates give similar values for these quantities for progenitors with different initial masses and compositions. For example, solar metallicity stars with greatly reduced mass loss rates also give similar results. Rotation, including the extreme case of chemically homogeneous evolution (CHE), increases the helium core mass for a given main-sequence mass and may affect the explosion mechanism, but otherwise gives similar outcomes. The same is true for stars in interacting binaries in which the envelope and part of the core may be lost or the envelope mass increased by accretion.

A great variety of light curves result from explosions of differing pulsational power and interval in progenitors of different mass and radius. Some are ultraluminous, others are quite faint, and many are relatively normal SNe IIP and SNe IIn. The nucleosynthesis is unique, however. Since it is usually assumed (though see Section 8) that the elements deep in the core all end up in a black hole, the new elements are restricted to lighter ones ejected in the pulses. He, C, N, and O are abundant, and some Ne, Na, and Mg may be ejected.

To begin our discussion, the physics of the PPI is briefly described. This includes both the physics used in the code (Section 2), especially for mass loss, as well as a brief discussion of the physics of the PPI itself (Section 3.1). Since the outcome of the PPI depends critically upon the helium core mass, some time is spent (Section 3.2) reviewing the outcome of instability and explosion in bare helium cores of constant mass. This has the advantage of removing some of the uncertainties in the mass loss rate, convection theory, rotationally induced mixing, and binary mass exchange, which affect the final helium core mass as a function of main-sequence mass. It also produces a set of models that are appropriate for hydrogen-stripped supernovae or for the products of CHE. Surveys of helium core evolution have been done before (Woosley et al. 2007; Woosley & Heger 2015a). These differ in carrying a larger nuclear reaction network, using improved stellar physics, and providing more detail on the observational outcomes.

The discussion then moves to full star models calculated for a metallicity 10% that of the sun. A grid of masses is treated that spans the range in which the PPI is observed to occur in the stars without rotation or binary interaction, $70\text{--}140 M_{\odot}$, and shows the results of varying the uncertain mass loss rate (Section 4). Attention is paid to the bolometric light curves expected for stars of different masses. These turn out to include long, low-luminosity red transients (Section 4.1), ordinary SNe II (Section 4.2), long, irregular, luminous supernovae (Section 4.3), recurrent supernovae, some ultraluminous (Section 4.4), and long transients that are not ordinary supernovae, but essentially young supernova remnants with intense circumstellar interaction (Section 4.5).

Subsequent sections explore a more limited grid of masses calculated for solar metallicity (Section 5), for low-metallicity blue progenitors (Section 6), and for rotating stars (Section 7). With a dramatic reduction in mass loss, near solar metallicity stars are capable of making PPISN virtually identical to those calculated for the low-metallicity stars. Models where a small presupernova radius is enforced show what might happen if the progenitor star is a blue supergiant (BSG) or luminous blue variable (LBV). The light curves, even for the same helium core masses, are appreciably different, especially at early times. The rotating models show a shift downward in the

main-sequence mass necessary to produce PPISN and also demonstrate that the cores of the stars are rapidly rotating when they die, which may have interesting implications for *how* they die.

None of the conservative, “first principles” models considered here produce supernovae as bright as the brightest “superluminous supernovae” (SLSN). Most stay below $10^{44} \text{ erg s}^{-1}$, and none emit more than $5 \times 10^{50} \text{ erg}$ of light, with only a few models briefly surpassing that luminosity. More speculative models are thus considered (Section 8) in which rapid rotation launches at least a partial explosion of the star when the iron core collapses. One motivation is the observation in recent 2D and 3D simulations of MHD core collapse of jet formation. It may be that leaving a large black hole remnant and producing an energetic explosion are not incompatible hypotheses. Given the freedom to invoke rotationally powered explosions *and* the ejection of large masses by the PPI, more luminous transients with smoother light curves are possible.

The next section (Section 9) discusses the (highly speculative) possibility that Eta Carinae is a PPISN in progress. The idea has appeal, but requires that Eta Carinae was a more luminous supernova and a more energetic explosion some time in the past than most people presently believe. It offers the tantalizing prospect, however, that the main “star” in Eta Carinae is actually a Wolf-Rayet remnant experiencing Kelvin-Helmholtz evolution on its way to becoming a massive black hole.

The nucleosynthesis expected from PPISN is then briefly reviewed (Section 11), and the relevance of stars in this mass range for gravitational radiation is briefly explored (Section 10). Section 12 summarizes the principal conclusions of the paper and gives a number of possible observational counterparts to PPISN in need of further study.

2. Code Physics and Assumptions

2.1. Basic Code Physics

All stars and explosions were modeled using the KEPLER code (Weaver et al. 1978; Weaver & Woosley 1993; Woosley et al. 2002). A value of 1.3 times the Buchmann (1996) rate for $^{12}\text{C}(\alpha, \gamma)^{16}\text{O}$ was employed. An additional description of the code physics is given in Woosley & Heger (2007) and Sukhbold et al. (2016). Rotationally induced mixing was treated for those models that included rotation, as described by Heger et al. (2000), and magnetic torques were included, as described by Heger et al. (2005). The use of an implicit hydrodynamics code was essential to the study of PPSN, which often required modeling cores that were still in tight hydrostatic equilibrium, while simultaneously following shock waves in tenuous, previously ejected matter. A typical calculation required from several days to a week on a single desktop CPU, with most of the time being spent in the large reaction network. Calculations employed 1200–1900 zones, continuously redistributed so as to resolve gradients in temperature, density, and composition. Typical runs took from 20,000 time steps for simple PISN to 60,000 or more steps for PPISN with several pulses. Several modifications to the standard setup were necessary to follow these events, which often made extreme excursions in density and temperature as they contracted, exploded, and then contracted repeatedly.

A nuclear reaction network of at least several hundred nuclei was directly coupled to the stellar model. Use of the “quasi-equilibrium” and “nuclear statistical equilibrium” approximations was avoided. Frequently, the cores would experience oxygen and silicon burning in their centers, producing a central region of iron, and then explode to low density and temperature, and then contract back to ignite silicon burning again later. It was important to follow the weak interactions during both the high-temperature burning and the long, cool phases where the temperature was frequently less than 10^9 K and the quasi-equilibrium network would have failed to converge. A small network would not have sufficed to follow weak interactions accurately. In all cases, the adaptive network approach proved stable and conserved mass to high accuracy. The network used was complete up to germanium ($Z = 32$), which is sufficient for following energy generation and electron capture. In several cases, the network was extended to bismuth to accurately track the weak s-process of nucleosynthesis (Section 11).

It was also important to follow convective mixing in the bound remnants, but not in shock waves or in the ejected shells, which were being carried in the same simulation. Convective mixing during the interpulse period affected the distribution of fuel for the next flash and needed to be included, but tracking convective mixing in a shock wave in the explosively ejected matter would have been unphysical and unstable. Convection extending all the way to the surface of any bound remnant gave that remnant an unphysically large luminosity during the interpulse period. The solution was simple. Convection was turned off in all zones exterior to a few tenths of a solar mass beneath the final remnant.

Shells ejected to very large radii, greater than 10^{17} cm, sometimes needed to be manually removed, especially when they became compressed and thin. Resolving fine structure in both the distant shells and a collapsing iron core required a greater precision than the code was set up to handle. The effect of these distant shells on subsequent pulses was negligible, amounting to no more than a dense interstellar medium surrounding the star. All mass that was ejected had its composition and energy added to the totals.

The opacity in the ejecta posed a special problem. The ejecting shells expanded to such low density that it was not on existing grids of stellar opacities. Treatment of the bound-free and bound-bound opacities in the presence of large-velocity shear would have posed problems. The approximation made here was to employ only electron scattering opacity everywhere after the pulsations began, and to calculate the electron abundance with an accurate Saha solver that included all ionization stages of 19 elements up to nickel. An opacity floor of $0.001\text{--}0.01 \text{ cm}^2 \text{ g}^{-1}$ was also assumed to account very approximately for other low-temperature sources of opacity besides electron scattering. This was important, for example, during the long interpulse periods when substantial matter fell back from an ejected shell and accreted, essentially at the Eddington luminosity on the core. The luminosity of the core from this accretion was substantial and opacity dependent because zoning at the accreting surface was coarse.

Particularly challenging were the (unrealistic) density spikes that developed when fast-moving shells snowplowed into ones moving slower. In a 1D code, there was no way for mixing and overturn to occur and no resistance to compression in regions with small velocity gradients, unless the density became so

high that ideal gas pressure offered some resistance. The pileup often included a large fraction of the entire ejected mass in a thin dense shell, all moving with the same speed. These density spikes could sometimes have a contrast $\Delta\rho/\rho$ with their surroundings of several orders of magnitude. In a 2D study that followed mixing instabilities (Chevalier 1982), the pileup would still exist, but not with such great contrast (Chen et al. 2014, 2016). Very tight convergence criteria on the radius (as small as $\Delta r/r = 10^{-13}$) were necessary to keep the calculation stable and, even then, often failed. Collisions of these thin, massive shells often produced unphysical spikes in the luminosity. Smearing out the spikes would broaden the peaks in the light curve due to the collisions of individual shells, while roughly preserving the total radiated energy. In cases where more than one collision occurs, the medium through which subsequent shocks propagate might be clumpy. See also Section 12.

2.2. Preexplosive Mass Loss and Opacity

The most uncertain aspect of thermonuclear PPISN is not how they explode, but how presupernova evolution produces the necessary helium core masses. A proper treatment of mass loss is critical to associating a given final behavior with a main-sequence mass. If the star loses all of its hydrogen envelope, and enough of its helium core to shrink below $30 M_\odot$, the pair-instability is avoided. This is probably the case for all stars of solar metallicity.

Mass loss in very massive stars is a subject of great interest and considerable uncertainty. Generally speaking, for single stars, the mass loss is of three varieties: line-driven mass loss, which dominates on the main sequence and for other hot stars (e.g., Vink et al. 2001; Smith & Owocki 2006; Vink et al. 2011); less well understood continuum-driven mass loss and envelope instabilities, which may play an important role in LBVs (e.g., Bestenlehner et al. 2014; Owocki 2015; Petrov et al. 2016); and mass loss where grain formation is important, as in red supergiants (RSGs; Voors et al. 2000; Groenewegen et al. 2009). Of these, line-driven mass loss is most studied and best understood. Analytic functions and routines are available to facilitate the use of such rates in computer codes.

The mass loss formula used here for the stars with hydrogen-rich envelopes is taken from Nieuwenhuijzen & de Jager (1990). Correcting a typo in the abstract, we have

$$\dot{M} = 9.63 \times 10^{-15} \left(\frac{L}{L_\odot} \right)^{1.24} \left(\frac{M}{M_\odot} \right)^{0.16} \left(\frac{R}{R_\odot} \right)^{0.81} M_\odot \text{ yr}^{-1}. \quad (1)$$

This formula is dated and of questionable accuracy, especially for the stars considered here, which lie far from the masses and metallicities for which the fit was originally calibrated. The expression is simple, however, and easily applied across the HR diagram. It was adopted, but multiplied by various constants less than one to explore the sensitivity of outcomes. It was also multiplied by $(Z/Z_\odot)^{1/2}$ to approximate its scaling with metallicity. For hot stars with line-driven winds, a better scaling might be $(Z/Z_\odot)^{0.64}$ or $(Z/Z_\odot)^{0.69}$ (Vink et al. 2001). Based upon an analysis of RSGs in the Milky Way, LMC, and SMC, Mauron & Josselin (2011) suggest a scaling of $(Z/Z_\odot)^{0.7}$, but with an uncertain factor overall of at least a factor of 4. Given the limited metallicity range studied here, the difference could be accounted for by a small shift in the overall

mass loss rate. Unfortunately, supergiant mass loss is important for many of the stars, and the scaling with metallicity there is unknown.

Using this formula and some simple approximations, one can estimate the necessary conditions for the pair-instability to occur in stars that still retain some hydrogen envelope. Because such massive stars all have luminosities near the Eddington limit, their lifetimes on the main sequence are nearly constant at 3 million yr, and their helium-burning lifetime is close to 300,000 yr (i.e., the Eddington luminosity divided by the energy release from hydrogen and helium burning assuming that the whole star burns). These numbers are validated later in the stellar models (Section 4) and are good to a factor of 2. There is some trade-off in that the luminosity is not quite Eddington and the fraction of the star's mass that burns to helium is only about 3/7. From 70 to 140 M_{\odot} , the main-sequence lifetime for nonrotating stars decreases from 3.3 to 2.5 Myr and the helium-burning lifetime varies from 330,000 to 270,000 yr. The luminosities both on the main sequence and during helium burning are, at all times, within a factor of 2 of $7 \times 10^{39} \text{ erg s}^{-1}$. For hydrogen burning, a more accurate approximation is $L_{\text{ms}} \approx 6 \times 10^{39} (M/100 M_{\odot})^{3/2} \text{ erg s}^{-1}$; for helium burning, $L_{\text{He}} \approx 9 \times 10^{39} (M/100 M_{\odot}) \text{ erg s}^{-1}$, where M is the zero-age main-sequence (ZAMS) mass of the star. Furthermore, the radius does not vary greatly on the main sequence: $R_{\text{ms}} \approx 1.0 \times 10^{12} (M/100 M_{\odot}) \text{ cm}$. The radius during helium burning does vary greatly, however, according to whether the star is a red SG, $R_{\text{He}} \approx 1-2 \times 10^{14} \text{ cm}$, or a blue one, $R_{\text{He}} \lesssim \text{few} \times 10^{13} \text{ cm}$. This variation introduces uncertainty into the estimated mass loss.

Together these approximations for L and R , an assumed hydrogen burning lifetime of 3 Myr, and a helium-burning lifetime of 0.3 Myr imply a total mass lost in solar masses of

$$\Delta M = (8 M_{100}^{2.83} + 55 R_{14}^{0.81} M_{100}^{1.40}) \left(\frac{Z}{Z_{\odot}} \right)^{1/2}, \quad (2)$$

where the first term is mass lost on the main sequence, the second term during helium burning, and R_{14} is the average radius during helium burning in units of 10^{14} cm . Assuming the mass of the envelope is 4/7 the mass of the star, the entire envelope will be lost when

$$F_{\text{env}} \approx (0.13 M_{100}^{1.83} + 0.96 M_{100}^{0.40} R_{\text{He},14}^{0.81}) \left(\frac{Z}{0.1 Z_{\odot}} \right)^{1/2}. \quad (3)$$

For solar composition, $R_{\text{He},14} \approx 2$; for 10% solar metallicity, $R_{\text{He},14}$ varies from 0.3 to 2, but is usually closer to 2. Since F_{env} must be less than 1, this equation implies that no solar metallicity star will end its life as a PPISN (or a PISN), but an appreciable fraction of stars with metallicity below 1/3 Z_{\odot} might (see also Langer et al. 2007; Georgy et al. 2013; Spera et al. 2015; Yusof et al. 2013), especially if the metallicity scaling of Vink et al. (2001) is employed instead of $Z^{0.5}$, or the mass loss rate of Nieuwenhuijzen & de Jager (1990) is an overestimate. This motivates the choice of $Z = 0.1 Z_{\odot}$ for emphasis in the present survey.

This estimate is very uncertain. The mass loss rate implied for a 100 M_{\odot} solar metallicity star with radius $2 \times 10^{14} \text{ cm}$ and luminosity $10^{6.5} L_{\odot}$ using the analytic expression above would be $10^{-3} M_{\odot} \text{ yr}^{-1}$. For the same star, Vink et al. (2001) give a mass loss rate of $2.5 \times 10^{-4} M_{\odot} \text{ yr}^{-1}$ (though the temperature

here, 4500 K, may be too cool to apply the Vink formula). Smith & Owocki (2006) estimate an upper limit to line-driven mass loss of $3 \times 10^{-4} M_{\odot} \text{ yr}^{-1}$ for a star of this luminosity (though see Müller & Vink 2008 for a different approach), and all of this theoretical work on line-driven winds neglects continuum-driven processes, instabilities, and grain formation. The default mass loss rates employed here are probably uncertain to at least a factor of a few and are likely overestimates. This affects the metallicity range where PPISN might occur, and even if they occur. To compensate for this uncertainty, the mass loss rates in the models were multiplied by various factors less than 1.

Opacity, semiconvection, and rotation also play important indirect roles in determining the mass loss. Less efficient semiconvection favors more time as an RSG and thus more mass loss. Rotational mixing affects the composition of the hydrogen envelope and its opacity, as well as the luminosity of the helium core. Higher opacities favor a larger stellar radius and hence greater mass loss. The OPAL opacities used here (Rogers & Iglesias 1992; Iglesias & Rogers 1996) have a well-known “iron bump” at low temperature that can lead to artificial density inversions in the outer envelopes of RSGs (Owocki 2015). This tends to overinflate the star and thus boost its mass loss. All of these effects need further study.

So long as the helium core is not uncovered prior to death, similar core masses and similar explosions result, including, for example, remnant masses. The exact value of the mass lost, as well as the secondary uncertainties in opacity, semiconvection, and rotation, serve to define the observational properties of the presupernova star and the metallicities that can make PPISN. To first order, though, they do not affect the explosion itself.

It also may be that the stars rotate sufficiently rapidly to experience CHE, in which case giant formation is avoided altogether and the formula of Nieuwenhuijzen & de Jager (1990) is not applicable. The treatment of mass loss for such stars is deferred to Section 7.

3. Helium Cores

Many general characteristics of PPISN can be understood from a simple study of pure helium stars evolved to the supernova stage at constant mass without rotation. Not only are the properties of PPISN most sensitive to the helium core mass at death, but often in nature, most or all of the envelope of a hydrogenic star is lost, either to a binary companion or a wind, so these models should have observable counterparts in nature. CHE (Section 7) will also produce stars whose late stages of evolution closely resemble that of bare helium cores.

3.1. General Characteristics of the Pulsational Pair-instability

In the weakest case, for the helium cores less than about 40 M_{\odot} , the PPI manifests as a small-amplitude, vibrational instability brought about by the temperature sensitivity of the nuclear reactions and the proximity of the structural adiabatic index to 4/3 (Section 3.2). As the core mass increases or the abundance of nuclear fuel declines, however, the instability becomes more pronounced. The amplitude of the pulses increases, and they become nonlinear. A major readjustment of the core structure occurs during each pulse that requires a Kelvin–Helmholtz timescale to recover. The most interesting explosions happen in this nonlinear regime.

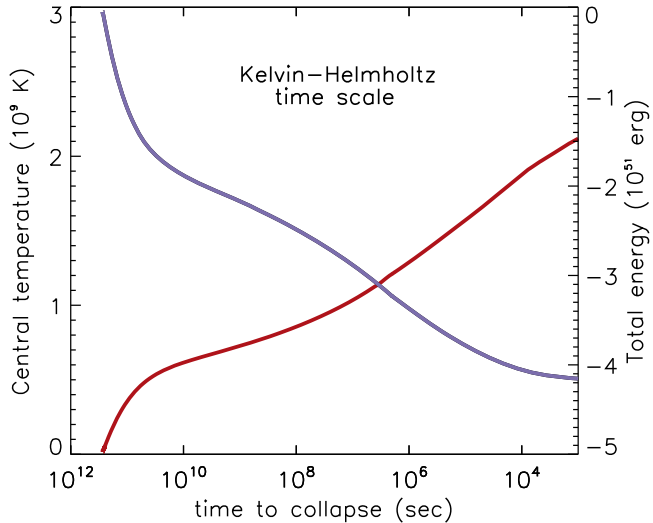


Figure 1. Kelvin–Helmholtz evolution of a $40 M_{\odot}$ helium star in which nuclear burning has been suppressed. The red curve gives the central temperature in billions of kelvins as a function of time. Time is measured backward from that point when the central temperature reaches 3×10^9 K and the core becomes dynamically unstable. Also shown is the net binding energy (internal plus gravitational binding energy) of the helium star. This is a negative number that is zero when the star is unbound. The change in slope at $\sim 10^{10}$ s ($T_9 = 0.65$, $\rho = 8000 \text{ g cm}^{-3}$) reflects the change from radiation-dominated to neutrino-dominated cooling and an acceleration of the contraction. The Kelvin–Helmholtz time starting from very low density is 2.7×10^{11} s. This is an upper bound to the recurrence time for any single pulse and an approximate upper bound to the total duration of pulsational activity. During each pulse, the total energy becomes less negative, and the core expands, cools, and moves to the left to a new point on the curve. The time between pulses is the Kelvin–Helmholtz time at this new binding energy. It is very short for weak pulses and very long for strong ones.

There, the characteristics of the PPI can be understood from an examination of the contraction, through its Kelvin–Helmholtz phase, of a helium star of constant representative mass. The relevant helium core masses for the PPI are in the range $35\text{--}65 M_{\odot}$, and final remnant masses are typically $35\text{--}45 M_{\odot}$. Figure 1 shows the evolution of a $40 M_{\odot}$ helium core in which nuclear burning, but not neutrino losses, has been suppressed. The evolution of a carbon–oxygen (CO) core of the same mass would be very similar. The pair instability has a strong onset around 3×10^9 K, and time in the figure is measured prior to that point. After reaching 3×10^9 K, the instability develops on a timescale of less than a minute.

During the explosive burning, typically of oxygen, an amount of energy is released that depends on the mass and composition of the core. More massive cores require more burning in order to reverse their implosion. Cores that have already burned some oxygen also bounce deeper and burn more, provided there is still fuel left to burn. Explosive burning leads to rapid expansion and cooling. Part of the energy released powers a shock wave that can eject matter from the edge of the core, but, qualitatively, the core’s evolution is not altered as long as its total mass stays roughly constant and nuclear reactions during the contraction are negligible. After a brief period of large-amplitude oscillation, the core settles back down into a new state of hydrostatic equilibrium at a less-negative net binding energy and commences a new stage of Kelvin–Helmholtz contraction.

The time until the next pulse depends upon the net binding energy following the prior pulse. A single pulse appreciably over 4.2×10^{51} erg in the $40 M_{\odot}$ model shown in Figure 1 would

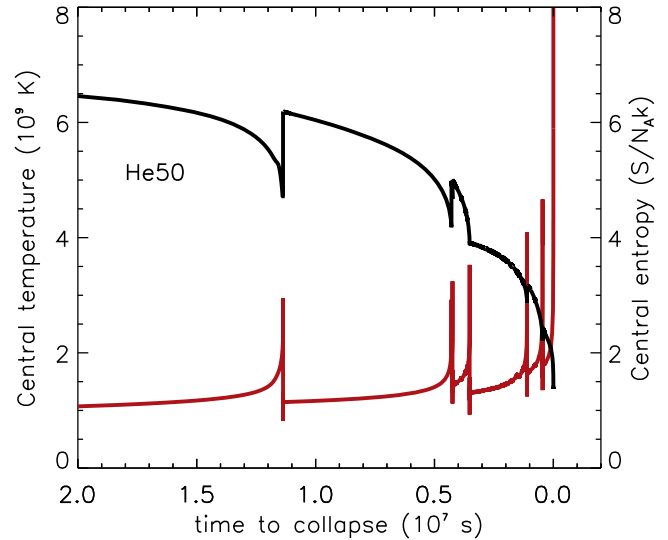


Figure 2. Central entropy (black line) and central temperature (red line) in a $50 M_{\odot}$ helium core contracting and experiencing PPI. Both quantities are plotted as a function of time until iron core collapse in units of 10^7 s. The dimensionless entropy ($S/N_A k$) rises in response to burning, but decreases due to neutrino losses. Spikes in temperature show major core pulsations. After the burning moves off-center, the central entropy no longer rises significantly during a flash, and the overall entropy continues to decline due to neutrino losses. Eventually the global entropy becomes small enough that the core becomes stable and evolves, without further flashes, to iron core collapse.

completely disrupt the core, producing a regular PISN. The abrupt generation of 2×10^{51} erg, on the other hand, would put the star back into a state similar to what existed 10^{10} s earlier. Of course, some energy would be lost to mass ejection, and the core entropy would change due to the burning and radiative losses (Figure 2), but qualitatively the evolution would be similar to the first contraction. The core explodes, stays bound, but relaxes to a less tightly bound configuration that experiences another stage of Kelvin–Helmholtz contraction until it becomes unstable again. The process repeats until all fuel is exhausted, the mass is reduced below a critical value, or the loss of entropy from repeated Kelvin–Helmholtz episodes removes the instability. Small explosions thus recur after a short time, while violent explosions initiate a longer wait. The interval between pulses is given by the energy of the prior pulse. Violent pulses also burn more fuel, so there are fewer of them before the core becomes stable.

The duration of the pulsations ranges from very short, essentially the hydrodynamic timescale of the helium core, or 10 minutes, to the Kelvin–Helmholtz time for the marginally bound core, or several thousand years (Figure 1). As we shall see, this broad range of energies and timescales results in a diverse set of observable phenomena.

Eventually, the core settles into stable silicon burning that produces an iron core of $2\text{--}3 M_{\odot}$ (Table 1) that collapses to a protoneutron star in the usual way. This final evolution is very unlike ordinary PISN, where no silicon or iron core is ever produced in hydrostatic equilibrium. In lower-mass helium cores, the PPI is mild and only afflicts the oxygen-burning shell during the last hours and days of the star’s life. For larger cores, though, violent pulses burn oxygen in roughly the inner six solar masses before the star settles into stable silicon burning. For the highest masses, some silicon has already burned to iron in the star’s center and, during the last phase, silicon burns in a shell.

Table 1
Helium Core Explosions

Mass (M_{\odot})	M_{CO} (M_{\odot})	Pulses	Duration (s)	KE-pulse (10^{51} erg)	M_{Fe} (M_{\odot})	M_{eject} (M_{\odot})	M_{remnant} (M_{\odot})
30	24.65	stable	2.34	...	30.00
32	26.30	stable	2.38	...	32.00
34	28.01	5 weak	2.3(3)	0.0012	2.51	0.13	33.87
36	29.73	33 weak	1.8(4)	0.0037	2.53	0.18	35.82
38	31.40	>100 weak	4.2(4)	0.0095	2.65	0.34	37.66
40	33.05	9 strong	7.8(4)	0.066	2.92	0.97	39.03
42	34.77	18	2.0(5)	0.26	2.68	2.65	39.35
44	36.62	11	7.7(5)	0.83	3.18	5.02	38.98
46	38.28	11	1.2(6)	0.77	2.40	5.51	40.49
48	40.16	8	3.8(6)	0.94	2.53	6.65	41.35
50	41.83	6	1.2(7)	0.86	2.76	6.31	43.69
51	42.59	6	1.9(7)	1.00	2.37	7.80	43.20
52	43.52	5	1.4(8)	0.99	2.47	7.87	44.13
53	44.34	4	7.8(8)	0.86	2.68	4.73	46.70
54	45.41	4	4.7(9)	0.94	2.16	6.85	47.15
56	47.14	3	3.4(10)	0.56	2.04	7.99	48.01
58	48.71	3	8.0(10)	1.1	2.00	12.14	45.86
60	50.54	3	8.5(10)	0.75	1.85	12.02	47.98
62	52.45	7	2.2(11)	2.3	3.19	27.82	34.18
64	54.14	1	...	4.0	...	64	...

3.2. The Evolution and Explosion of Helium Stars

Bare cores consisting initially of pure helium with masses from 30 to 64 M_{\odot} ($Z = 0$) were evolved from the helium-burning main sequence either to iron core collapse, or, in one case ($64 M_{\odot}$), to complete disruption as a PISN (Table 1). Mass loss and rotation were neglected, though the cores could have resulted from rotating stars. In all cases, most of the helium core burned to carbon and oxygen before the explosion, so the inclusion of a small amount of mass loss would have resulted in a WC or WO Wolf–Rayet star contaminated with a small fraction of helium rather than a star with a predominantly helium surface, but the explosion dynamics for the same presupernova core mass would be very similar. For zero-metallicity helium stars, the mass loss rate is expected to be small (Vink & de Koter 2005), but even for low metallicities, the mass loss from a helium star of such large mass would not be negligible (e.g., Woosley & Heger 2006). The masses considered here reflect what remains after all mass loss is finished and the star dies, not necessarily the helium core mass at the end of hydrogen burning.

Principal results are given in Table 1 and Figures 3–7 (see also Woosley et al. 2007; Woosley & Heger 2015a). The duration of the pulsing phase (Table 1) is measured from the onset of the first pulse to iron core collapse, even though, in the more massive cases, shell collisions often finished before iron core collapse or continued long afterward. The PPI first becomes noticeable near $34 M_{\odot}$, where it is encountered in the oxygen-burning shell during the last few hours of the star’s life. It begins as a series of weak flashes, each lasting about 500 s, roughly the sound-crossing time for the helium star. The central density and temperature vary only slightly during each pulse, but cumulatively, the piling up of shocks from numerous weak pulses in Model He34 results in the ejection of about $0.1 M_{\odot}$ with a kinetic energy of $\sim 10^{48}$ erg. For bare helium cores, this small ejection produces a very weak transient that would be difficult to detect. In a RSG, however, even this small amount of energy would be sufficient to eject a significant part of the hydrogen envelope and produce a faint supernova (Section 4).

In the absence of significant rotation, the remainder of the helium core collapses into a black hole, so this minor ejection would be the only observable signal of the star’s death (other than its disappearance).

For helium cores up to $40 M_{\odot}$, essentially the “linear regime,” increasing the mass shifts the onset of the PPI to earlier times, increasing the time the star spends pulsing, the number of pulses that occur, and their total energy. More mass is ejected, with the energy eventually reaching $\sim 10^{49}$ erg at $40 M_{\odot}$. Up to this point, the pulses are only minor perturbations on a monotonically increasing central temperature with $\Delta T/T \lesssim 30\%$ (Figure 3). Starting at about $40 M_{\odot}$, a qualitative change in behavior occurs, as dozens of weak pulses give way to a series of less frequent explosions. From this point on, the “pulsations” cease to be perturbations on the core structure and become discrete explosive events, each generating a dynamic response and significant mass ejection. Each explosion is followed by relaxation oscillations and an extended period of Kelvin–Helmholtz contraction to a new unstable state (Section 3.1).

By $44 M_{\odot}$, the interval between pulses is becoming a week or more, long enough to discern the effects of individual flashes on the light curve of a SN I (Section 3.3). The combined energy in the pulses also becomes comparable to that of common supernovae. Above about $50 M_{\odot}$, the duration of the pulses exceeds the time for material coasting at a few thousand km s^{-1} to reach 10^{15} cm, a typical photospheric radius for a supernova. Shells thus collide in a region that is not very optically thick, and their differential kinetic energy can be converted into radiation without much adiabatic degradation. The time when the iron core collapses begins to lag appreciably after the onset of the light curve, opening the possibility of recurrent events and surviving stars in supernova remnants. By $50 M_{\odot}$, the total kinetic energy approaches 10^{51} erg, but this energy is shared among several pulses, and the efficiency of converting kinetic energy to light remains relatively small.

The models from $52 M_{\odot}$ to $62 M_{\odot}$ share similar characteristics (Figures 3 and 4). All have a strong first flash followed,

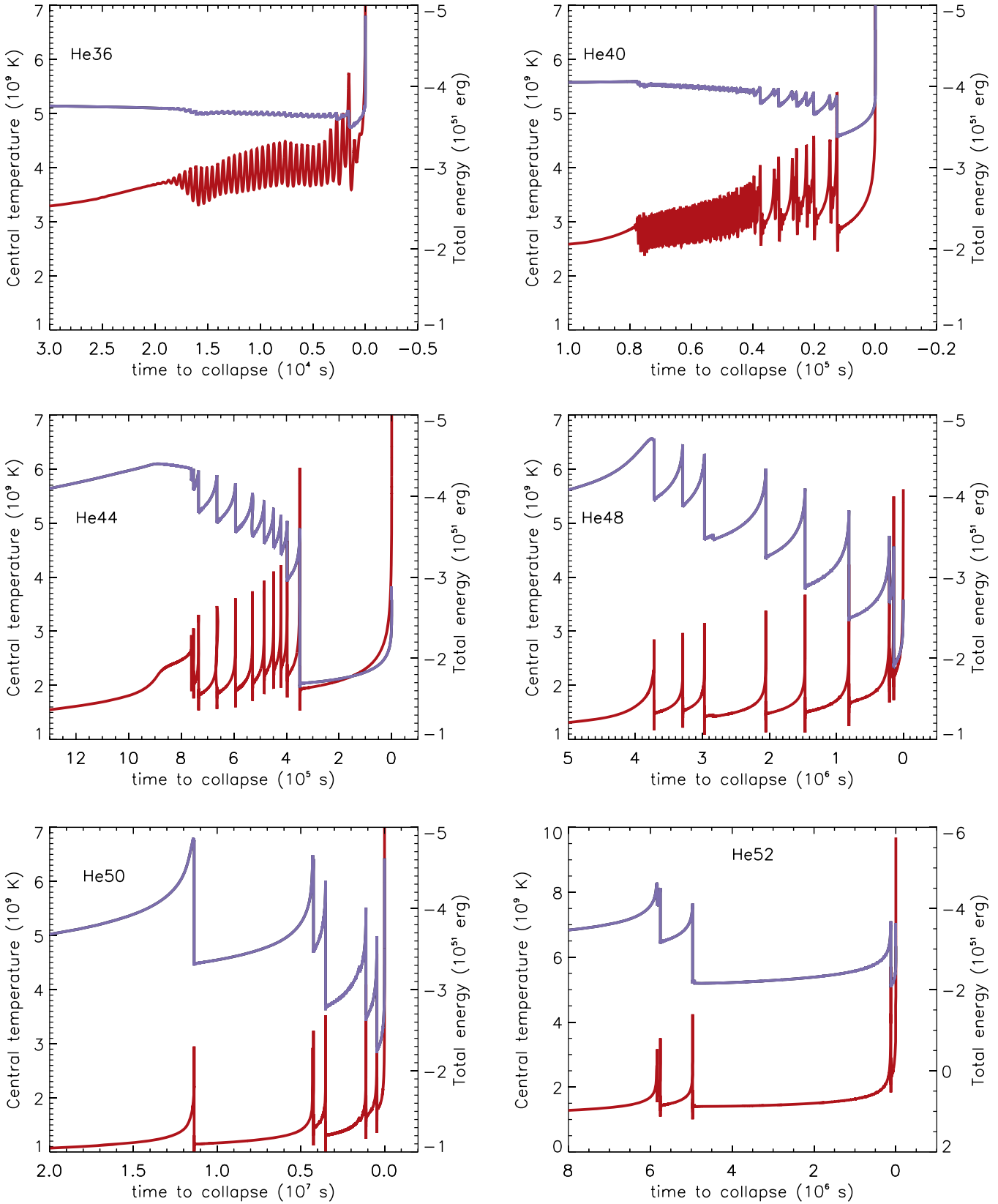


Figure 3. Pulse history in bare helium stars of $36, 40, 44, 48, 50$, and $52 M_{\odot}$. The central temperature in 10^9 K is the red line, and the net binding energy in 10^{51} erg is blue. Time, measured prior to final core collapse to a black hole, is in units of 10^4 s for the $36 M_{\odot}$ model, 10^5 s for the 40 and $44 M_{\odot}$ models, 10^6 s for the $48 M_{\odot}$ and $52 M_{\odot}$ models, and 10^7 s for the 50 model. In the $52 M_{\odot}$ model, a strong flash (not shown) occurred 4.6 yr prior to the final collapse. For that model, the panel only shows the activity during the last few months, when several pulses in rapid succession occurred toward the end.

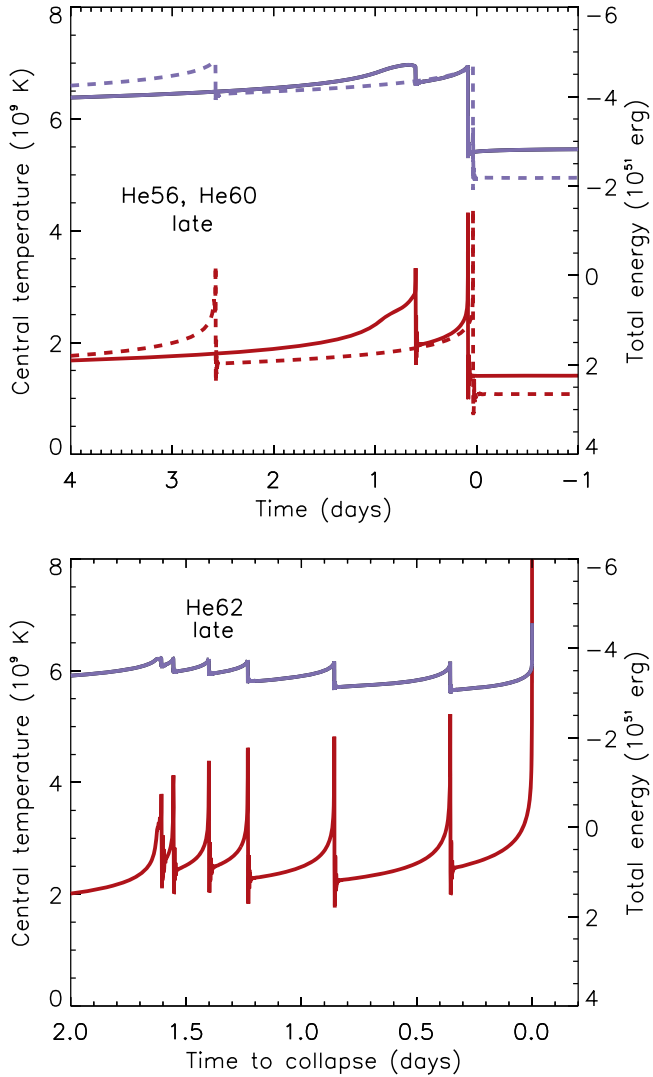


Figure 4. Top: history for the second and third pulses of helium stars of 56 and $60 M_{\odot}$. The central temperature (red) is in units of 10^9 K; the net binding energy (blue) is in units of 10^{51} erg. Time is measured with respect to the final pulse before core collapse. For the $56 M_{\odot}$ model (solid line), the two pulses commence 1060 yr after the first pulse (not shown) and end 91 days before core collapse (not shown). For the $60 M_{\odot}$ model (dashed lines), the first pulse was 2680 yr earlier, and the pulses shown here end 6.0 yr before core collapse. Weak final pulses occurred in both models at the time of core collapse. Bottom: similar final pulsing activity for Model He62. Since the first pulse ejected $36 M_{\odot}$, 7000 yr have elapsed. Only in the bottom plot is zero the time of iron core collapse.

after a long delay, by other pulses. As the mass increases, so does the energy of this first pulse. An increasingly large mass is ejected promptly, and the wait time for the next pulse increases. For $52 M_{\odot}$, the mass ejected promptly and its energy are $1.1 M_{\odot}$ and 0.80×10^{50} erg; for $54 M_{\odot}$, $2.3 M_{\odot}$ and 1.9×10^{50} erg; for $58 M_{\odot}$, $7.4 M_{\odot}$ and 6.6×10^{50} erg, and for $62 M_{\odot}$, $36 M_{\odot}$ and 2.1×10^{51} erg. In this last case, the star is very nearly unbound. Indeed, Model He62 marks the transition to a full PISN at $64 M_{\odot}$. The ejected matter carries no radioactivity though, and, neglecting any interaction with prepulsational mass loss, the light curve this first pulse makes is faint, hot, and brief.

The object left behind typically has a mass near $51 M_{\odot}$ (except for the $62 M_{\odot}$ model) with oxygen depleted in its

center. The flash has left it substantially extended and cool inside. For $54 M_{\odot}$ the central temperature after the first pulse and relaxation oscillations are over is 6.6×10^8 K; for $58 M_{\odot}$ it is 3.69×10^8 K; and for $62 M_{\odot}$ the central temperature is only 4.0×10^7 K, again showing how marginally bound the $62 M_{\odot}$ model is after its first pulse. For cores above $54 M_{\odot}$, energy loss from this extended core is dominated by radiation from the stellar surface, not by neutrinos in the core, and it takes a long time, up to 7000 yr, to become unstable again. During this time, an observer would see the remnant of a faint supernova, with a brightly glowing Wolf–Rayet star in its center. If there was appreciable prepulsational mass loss, the object might also be a bright radio or X-ray source (Chevalier 1982; Chevalier & Irwin 2012; Svirski et al. 2012). These objects, having experienced a first outburst with more to come at a much later time, will be referred to as “dormant supernovae” (a more suggestive name might be “zombie supernovae,” or supernovae Type Z). The time spent in hibernation is approximately the time required to radiate the change in binding energy of the core brought about by the first pulse at either the Eddington luminosity (radiative case) or the global neutrino loss rate in the expanded state.

In all these models from 52 to $62 M_{\odot}$, pulsational activity, consisting of two or more strong pulses in rapid succession, resumes as the star approaches its final death. These terminal pulses, which often come in pairs, are capable of producing bright transients (Section 3.3). In Model He52, pulsations resumed after 4.6 yr (Figure 3). In Models He56 and He60, activity resumed after 1060 and 2680 yr, respectively (Figure 4). There, pulses 2 and 3 ejected a combined $4.6 M_{\odot}$ with 2.5×10^{50} erg and $2.0 M_{\odot}$ with 1×10^{50} erg, respectively. Model He62 ejected $1.45 M_{\odot}$ with an energy of 2.1×10^{50} erg just before dying (Figure 4). These delays are very nearly equal to the total time of pulsational activity (Table 1). If the final iron core collapse produces no outgoing shock, these late-time pulses may be the most readily detected signals of PPISN in this mass range (though see Section 8).

The values in Table 1 suggest an upper limit to the kinetic energy of purely thermonuclear PPISN of Type I that may be shared by several pulses of $\sim 2 \times 10^{51}$ erg. Most of this energy comes out in the first pulse of Model He62, however, and, unless the star had very substantial mass loss before becoming pulsationally unstable, is not available for making radiation. For events that might produce optical supernovae, the upper bound is closer to 1×10^{51} erg. Full star models in Section 4 show a larger upper bound of about 4×10^{51} erg because of the efficient coupling of the large-amplitude bounce to more matter and the stronger secondary explosions caused by the increased tamping. As will be discussed, the amount of light radiated is only a fraction of these kinetic energies.

All of the helium core models that did not completely disrupt as PISN produced massive iron cores (Table 1) surrounded by dense shells of silicon and oxygen that would be very difficult to explode with neutrinos. Typical net binding energies for the oxygen and silicon mantles around the iron cores were $3\text{--}5 \times 10^{51}$ erg. While very rapid rotation might still power an explosion (Section 8), it seems likely that many of these stars will make black holes. Thus stars of this mass would generate a population of $35\text{--}50 M_{\odot}$ black holes and nothing lighter or heavier.

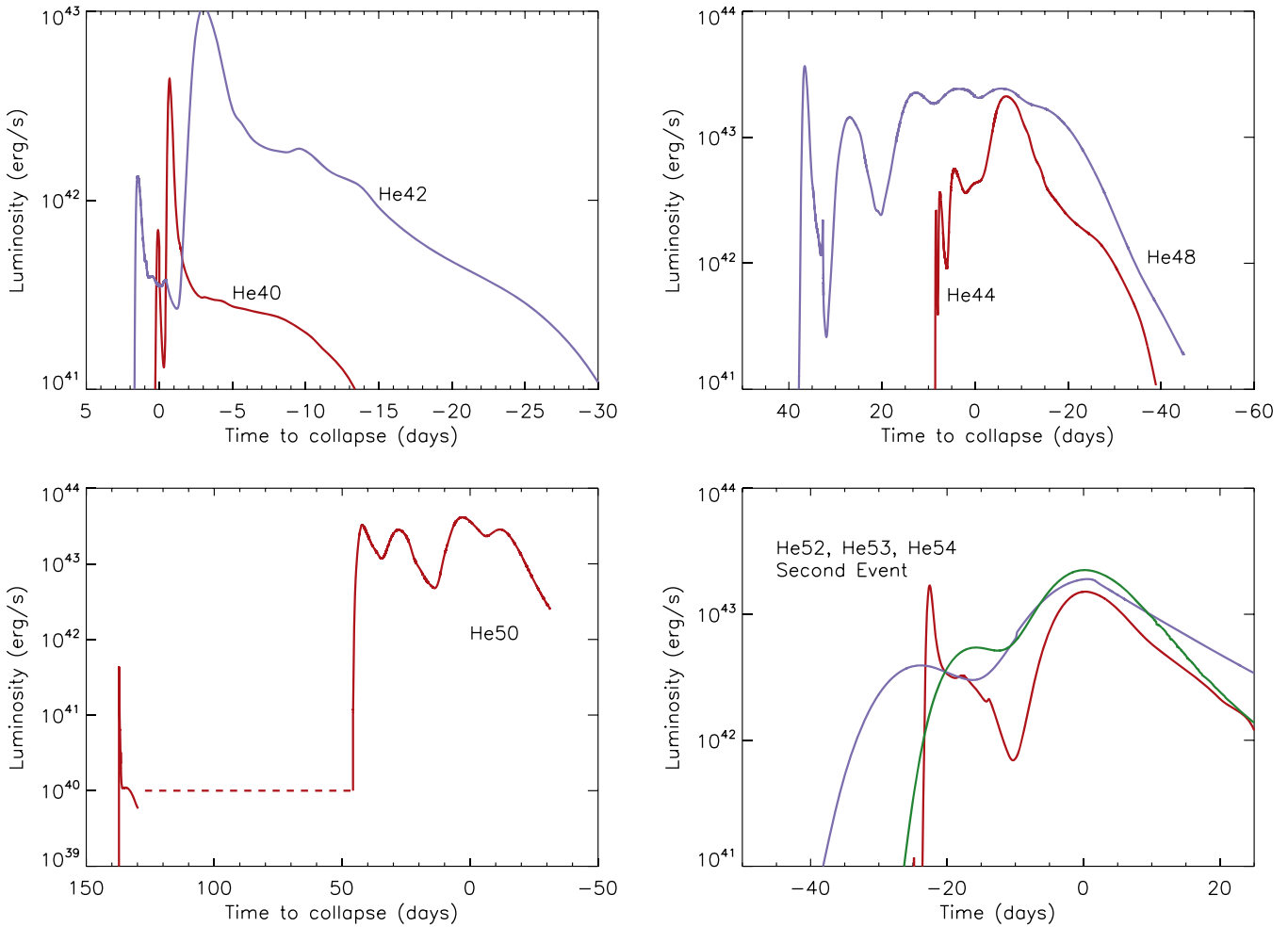


Figure 5. Bolometric light curves for the explosion of bare helium stars of various masses. See also Figures 3 and 6. In the top two and bottom left frames, time is given in units of days and measured relative to iron core collapse, with negative values indicating time elapsed after collapse. The light curve for He50 shows two components, an early plateau as the mass ejected by the first pulse expands and recombines and a brighter complex display produced by the collisions of subsequent pulses with the ejecta of the first and each other. The dashed line (not calculated) indicates an approximately Eddington luminosity for the remaining core during the two pulsationally powered outbursts. In the bottom right frame, the second, brighter outbursts are given for the $52 M_{\odot}$ (blue), $53 M_{\odot}$ (green), and $54 M_{\odot}$ (red) models, which began their pulsing activity with a faint outburst 4.6, 24.5, and 149 yr earlier. In this case, zero time arbitrarily corresponds to the light curve maximum. Below $40 M_{\odot}$, the optical transient produced by the PPI is very faint.

3.3. Helium Core Light Curves

Light curves for the exploding helium cores were calculated using the KEPLER code. KEPLER uses flux-limited radiative diffusion and operates, while conserving energy and momentum, in both optically thick and thin regimes. The bolometric light curves that KEPLER calculates have been compared favorably with those from other more powerful radiation-transport codes running similar problems (e.g., Eastman et al. 1994; Scannapieco et al. 2005; Woosley et al. 2007; Kasen et al. 2011). Unfortunately, KEPLER treats the radiation as a blackbody having a single temperature, the same as the background matter, and thus provides limited information on the brightness in various wavebands. It is also unable to calculate a realistic opacity in an optically thin region with a large Doppler shear. Here, in the ejected material, opacity is assumed to be entirely due to electron scattering with a floor assigned for recombined material of either 0.001 or $0.01 \text{ cm}^2 \text{ g}^{-1}$. The smaller value is used in recombining ejecta, the latter when fallback is important.

Sample results, given in Figures 5 and 6, reveal a broad range of possibilities. These bolometric curves may require

appreciable correction before comparing with optical light curves. Not only are the bolometric corrections frequently large, especially at early times near shock breakout, but the rapid time variations resulting from colliding shells (e.g., Models He44 and He48) would be much smoother in a multidimensional simulation where the shells would be substantially broadened by instabilities (Chen et al. 2014). Any interaction with prepulsational mass loss is ignored and might also contribute a substantial background luminosity.

Presupernova Model He40, for example, has a radius of $3.5 \times 10^{10} \text{ cm}$, so even a moderate breakout luminosity of $10^{42} \text{ erg s}^{-1}$ implies an effective emission temperature of about 10^6 K . The matter expands rapidly though, so the “plateau” stage in He40 lasts about a week at helium recombination temperatures, $\sim 10,000\text{--}20,000 \text{ K}$. Model He40 would thus appear as a fast, faint, blue transient with relatively slow photospheric speeds of $2000\text{--}3000 \text{ km s}^{-1}$. It might be categorized as a faint Type Ibn or Icn event.

For cores lighter than $48 M_{\odot}$, the pulsing activity goes on for a short time (Table 1) and, since the matter has not expanded

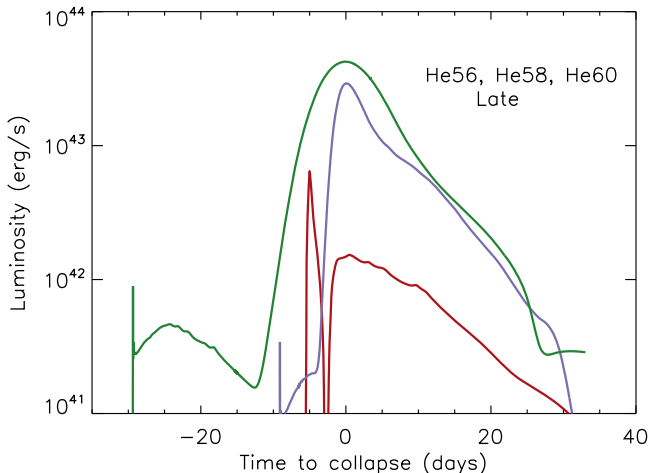


Figure 6. Light curves during the second outbursts of Models He56 (red), He58 (green), and He60 (blue) caused by pulses 2 and 3 (see Figure 4). Zero time is arbitrarily set to the postoutburst maximum of the curve. The core collapsed 84 days after zero in the plot for He56, 3.4 days later for He58, and 5.9 yr later for He60. The initial spikes caused by shock breakout are very hot and would be faint in the optical band.

greatly beyond $\sim 10^{15}$ cm, there is a well-defined photosphere during the brighter parts of the light curve. At peak luminosity after breakout, Model He42 (Figure 5) has a photospheric radius of 2×10^{14} cm and an effective temperature of 23,000 K; Model He44 has a radius of 7×10^{14} cm and a temperature of 15,000 K; and Model He48 has a radius of $\sim 10^{15}$ cm and an effective temperature of 12,000 K. Shell velocities are typically 2000–4000 km s $^{-1}$.

Most likely these events would be categorized as SNe Ibn and SNe Icn (Foley et al. 2007; Pastorello et al. 2008a, 2008b; Smith et al. 2012). Their luminosity, duration, colors, and velocities are similar, though the postpeak decline rate is difficult to predict with any accuracy in these 1D models because of mixing, circumstellar interaction, and bolometric corrections. It is interesting that SN 2006jc had a faint “LBV-like” outburst 2 yr before its major display (Pastorello et al. 2007, 2008a), which might associate it with a helium core of about $51 M_{\odot}$ (Figure 5). Although very rare, other events like SN 2006jc have been observed, for example SN1999cq (Matheson et al. 2000), SN2002ao (Foley et al. 2007), SN 2010al (Pastorello et al. 2015a), and ASASS-15ed (Pastorello et al. 2015b). The models here, by design, all lack hydrogen, which may play an important role in some of these events, especially SN 2011hw (Smith et al. 2012), but hydrogen would be present in structurally similar WNL stars that would have similar light curves upon exploding.

Models heavier than $48 M_{\odot}$ have more complex light curves with several components. First comes a faint, brief transient similar to that in the lighter stars, resulting from the ejection of the outer part of the core by a single pulse. Lacking any radioactivity and neglecting circumstellar interaction, that explosion is not bright. Even in the brightest case (Figure 7), the luminosity produced as the helium expands beyond 10^{14} cm and recombines does not exceed 10^{41} erg s $^{-1}$. Because of the low luminosity and rapidly increasing radius, the transient may evolve rapidly in color. All are initially blue, but some can become red at late times, especially the more massive models. Models He54, He58, and He64 were all near 12,000 K at age 1 day, but they declined to 11,000 K, 8000 K, and 4500 K,

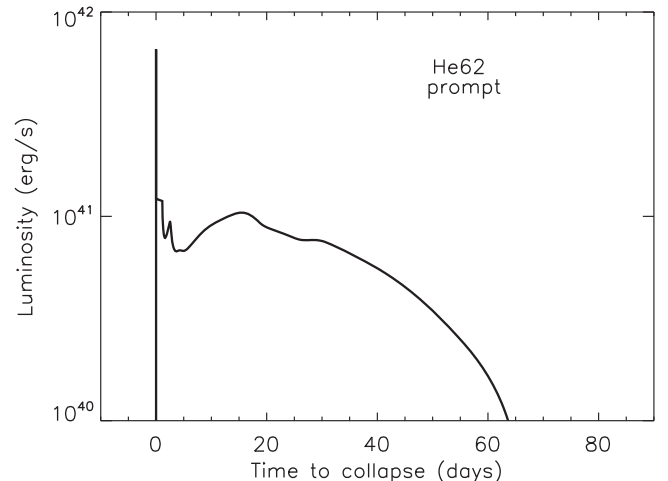


Figure 7. First explosion of Model He62. The ejection of the outer $24 M_{\odot}$ gives rise to a faint display. Lighter models from 50 to $60 M_{\odot}$ have similar but fainter and shorter initial light curves (see Figure 5). The effective temperature at peak luminosity (neglecting breakout) is about 5000 K.

respectively, at peak. Velocities were typically a few thousand km s $^{-1}$, though higher in He62 and in the outermost layers of the other models. While optically faint, these initial outbursts carry considerable kinetic energy, up to 2×10^{51} erg, and could power bright optical, radio, and X-ray transients if, as seems likely, the prepulsational star had experienced substantial mass loss.

The second pulsationally powered display from stars in this mass range is brighter (Figures 5 and 6). Two or more pulses occur in rapid succession, shortly before the iron core collapses (Figures 3 and 4). The light curve has two stages, a faint plateau as the first pulse of the delayed series (“pulse 2”) ejects more core material, and a brighter second peak as subsequent pulses collide with that ejecta and with themselves. If two pulses occur sufficiently rapidly, the first may simply inflate the star to a larger radius, while the next shock traverses that still optically thick “envelope” and produces a sharp peak due to breakout, as in Models He54 through He60. Or the shells may collide after becoming almost optically thin, producing broad peaks like in He52 and He53 (Figure 5). The light curve is blue, especially at early times. Typical temperatures at the bright peak are 10,000–12,000 K, though the photosphere is not always well defined in the heavier models where the collision happens in a medium thin to electron scattering. Velocities are 2000–4000 km s $^{-1}$, though a small amount of material moves slower and faster.

This sudden rise to a secondary maximum is similar to what has been observed in several unusual supernovae. Consider SN 2005bf (Folatelli et al. 2006) as compared with Model He52 (Figure 5). The luminosity, duration, spectral type (Ic), and “double-peaked” shape are all roughly similar. The model photospheric temperature on the first bolometric peak was 8000 K and on the second peak 10,000 K, within the bounds of the observations at similar times. Model He52 also had two velocity components, one from its first mass ejection (up to above 10,000 km s $^{-1}$ at its outer edge at $\sim 10^{17}$ cm), and a much larger mass from the later outburst that made the bright light curve move at about 4000–7000 km s $^{-1}$. This is not necessarily to say that SN 2005bf was a PPISN. A low-metallicity region would probably be required to make a

PPISN, and the metallicity of the host of SN 2005bf was not specified. The very high velocity material (over 10,000 km s⁻¹) in Model He52 only existed very far out in about 0.001 M_{\odot} of ejecta and, by design, contained no hydrogen. But if Model He52 were detected today, observers would probably call it “SN 2005bf-like.” Indeed, as will be discussed further in Sections 6 and 12, there are also several SNe IIn that display this sort of pause before dramatically brightening, among them SN 1961v (Kochanek et al. 2011; Smith et al. 2011), SN 2009ip (Fraser et al. 2015), and SN 2010mc (Ofek et al. 2013). The structural distinction between WC, WO, WNL, and LBV progenitors is not great, and this double-peaked structure may be a common signature of the PPI operating in compact progenitors.

During the long dormant phases between the initial outburst and the bright second display, the luminosity for models between 50 and 60 M_{\odot} is provided by the central star and is close to the Eddington value, approximately 10⁴⁰ erg s⁻¹. The energy comes from a combination of Kelvin–Helmholtz contraction and the fallback of incompletely ejected supernova material. Even though the energy source is not thermonuclear, such stars would have radii of a few times 10¹¹ cm, similar to WR stars, which they might closely resemble. In all likelihood, the prepulsationally unstable star had a strong wind or episodic mass loss, so these dormant supernovae could be very bright radio and X-ray sources while awaiting their next outburst.

Even lacking this prepulsational mass loss, the final explosions would eventually catch up with the mass ejected by the very first pulse. Characteristic radii would be a few thousand km s⁻¹ times the “duration” given in Table 1, or 10¹⁶–10¹⁹ cm. The collision could give a very bright, long-lasting transient with uncertain properties, especially for the lighter models, where the collision happens earlier when the density is higher. The emission might be strong in radio and X-rays.

None of the bare helium cores studied here produced an exceptionally brilliant SLSN. Models He48 and He50 (in Figure 5) had a total light output of 0.84 and 1.2 × 10⁵⁰ erg, respectively, so an upper limit of about 1 × 10⁵⁰ erg of radiated light seems reasonable for pure PPISN coming from bare helium or CO cores. Later it will be shown that full stars with hydrogen envelopes can produce appreciably brighter light curves with up to 5 × 10⁵⁰ erg of light.

4. Full Stars without Rotation: Red Supergiants

Consider now the evolution of PPI unstable helium cores evolving inside stars that have not lost their hydrogenic envelopes. Depending upon their mass loss histories, metallicities, and rotation rates, such stars will die as red or blue supergiants, LBVs, or, in the case of rapid rotation and CHE, compact WR stars. Each case will be considered, but we begin with the most common result for the mass loss rates and metallicities assumed, PPISN occurring in RSGs.

The presence of a tenuous envelope, however massive, does not greatly alter the hydrodynamic behavior of a helium core encountering the pair-instability for the first time. Once the first explosion is underway, however, the envelope has major consequences for both the light curve and the subsequent evolution. The envelope tamps the expansion of the core and absorbs momentum, resulting in more of it falling back. This increases the mass of the bound remnant over what it would have been without an envelope and hinders its expansion to

low density, thus shortening the interval between pulses. It also makes the remnant core larger and subsequent pulses more energetic. Overall, it broadens the mass range for the PPI and shifts the masses of helium cores in Table 1 where various phenomena are expected upward by a few solar masses. At the upper end, this means that helium cores that might have been completely unbound if they were bare still leave behind bound remnants when embedded in envelopes. The maximum energy produced by a PPISN is modestly increased.

With a hydrogen envelope, a greater diversity of observable transients is also possible. Assuming for now that the final core collapses to a black hole, PPISN eject no radioactive ⁵⁶Ni, so their displays are entirely a consequence of recombining pulse-ejected envelopes and colliding shells. For the lower energy pulses in light PPSN, the luminosity on the plateau may be faint since only part of the envelope is ejected, and even that at low speed. For higher energy pulses, but still with a duration of less than a few months, brighter, longer lasting, “normal” SNe IIP result. For the energetic, infrequent pulses that characterize high-mass PPISN, a mixture of SNe IIP and IIn occurs. The structure of the light curves can be complex. Each pulse can make from one to several light curve peaks as the mass it ejects expands and cools and runs into shells present from previous outbursts.

To illustrate and quantify these outcomes, the evolution of stars with a variety of masses and mass loss rates is considered. The key quantities are the helium core mass of the presupernova star and the mass and radius of the hydrogen envelope. Many uncertain factors—mass loss rates, opacities, rotational mixing, and convective overshoot mixing—enter into determining these three quantities, but to first order, two presupernova stars with the same helium core mass, hydrogen envelope mass, and radius will have similar light curves and leave similar remnant masses. The results given are thus generic for other choices of stellar parameters that give these final masses, though the main-sequence masses and metallicities responsible for these final states will shift.

Table 2 shows the results for a grid of 10% solar metallicity stars in the main-sequence mass range 70–150 M_{\odot} . For the assumed stellar physics, these give helium core masses in the range 30–70 M_{\odot} and thus span the range where PPISN are expected. Since mass loss on the main sequence is relatively small, the helium core mass for these models is mostly determined by the main-sequence mass, but the mass of the hydrogen envelope (if any) that surrounds the presupernova core depends on the mass loss rate. Here the standard mass loss rates (Section 2.2) have been multiplied by factors of 1, 1/2, 1/4, 1/8, and 0. The modified cases, with multipliers 1/2, 1/4, and so on are referred to as the “A,” “B,” “C,” and “D” series of a given mass. The models are thus named by their metallicity (“T” for a tenth of solar), their main-sequence mass, and their mass loss rate. Model T100D was a 100 M_{\odot} star on the main sequence with no rotation, a metallicity 1/10 that of the sun, and no mass loss. Smaller multipliers also correspond to the results expected for stars of lower metallicity since, for a given structure, the mass loss is just proportional to Z to some power. Very low metallicity stars might also be blue rather than red supergiants and have still lower mass loss rates.

The helium core masses and CO core masses rise roughly monotonically with main-sequence mass. Small variations are expected due to the complex interplay of mass loss, convection, convective overshoot mixing, and semiconvection. Larger

Table 2
Low-metallicity Models

Mass (M_{\odot})	Mass Loss	M_{preSN} (M_{\odot})	M_{He} (M_{\odot})	M_{CO} (M_{\odot})	M_{Si} (M_{\odot})	M_{Fe} (M_{\odot})	Duration (10^7 s)	M_{final} (M_{\odot})	KEject (10^{50} erg)
T70	1	47.31	29.42	25.62	7.58	2.54	0.00066	47	...
T70A	1/2	51.85	30.10	26.41	7.87	2.58	0.00065	52	...
T70B	1/4	59.62	30.50	26.84	8.28	2.57	0.00072	60	...
T70C	1/8	64.66	30.72	27.14	8.22	2.54	0.00068	65	0.0005
T70D	0.	70	31.57	28.00	8.41	2.57	0.0012	52	0.015
T75	1	48.46	32.47	28.36	7.41	2.54	0.00075	41	0.0028
T75A	1/2	54.24	31.90	27.97	8.64	2.52	0.0014	42	0.024
T75B	1/4	62.97	33.07	29.15	8.71	2.64	0.0015	51	0.021
T75C	1/8	68.61	33.41	29.67	8.91	2.61	0.0016	51	0.029
T75D	0.	75	33.82	30.20	8.71	2.67	0.0019	50	0.11
T80	1	50.79	34.70	30.81	7.90	2.65	0.0019	39.6	0.19
T80A	1/2	55.32	34.59	30.74	8.38	2.62	0.0061	39.2	0.39
T80B	1/4	66.04	35.30	31.37	8.44	3.00	0.0098	34.7	0.92
T80C	1/8	72.76	36.24	32.28	8.03	3.29	0.014	34.8	1.3
T80D	0	80	36.40	32.56	7.93	3.09	0.015	34.9	1.5
T90	1	55.32	38.77	34.58	7.16	2.73	0.039	37.3	2.6
T90A	1/2	60.62	39.69	35.37	9.54	2.57	0.11	35.9	4.1
T90B	1/4	72.16	40.41	36.16	9.54	2.84	0.18	36.4	5.2
T90C	1/8	80.61	40.21	36.00	6.22	2.87	0.20	37.4	4.9
T90D	0	90	40.92	36.78	8.35	2.86	0.19	37.1	4.9
T100	1	57.58	44.85	39.65	4.56	2.48	1.0	38.9	7.0
T100A	1/2	62.20	44.46	39.74	5.24	2.73	0.74	39.3	7.7
T100B	1/4	78.58	45.11	40.61	4.64	2.44	0.92	39.9	7.6
T100C	1/8	88.11	45.71	41.23	4.67	2.53	1.7	40.4	6.9
T100D	0	100	45.13	40.70	6.44	2.87	0.45	40.4	6.6
T105	1	59.54	47.52	42.00	4.78	2.79	7.34	43.6	7.8
T105A	1/2	66.88	46.04	41.45	4.78	2.62	1.22	40.8	8.0
T105B	1/4	81.18	47.34	42.55	5.75	2.92	2.20	42.5	7.8
T105C	1/8	91.94	48.33	43.56	4.70	2.73	4.38	44.2	7.0
T105D	0	105	49.45	44.67	4.87	1.97	10.7	44.8	7.8
T110	1	63.31	49.89	44.39	4.92	1.98	17	45.1	8.6
T110A	1/2	68.41	49.68	44.58	4.88	1.95	39	44.5	7.6
T110B	1/4	84.13	49.50	44.67	4.70	2.18	9.5	44.7	7.4
T110C	1/8	95.98	48.91	44.19	4.53	2.59	5.8	44.8	7.1
T110D	0	110	50.49	45.44	4.75	2.08	30	45.0	7.7
T115	1	63.23	53.09	47.11	5.51	1.85	2600	49.3	11.5
T115A	1/2	71.40	50.47	45.40	4.78	2.38	13	45.7	7.9
T115B	1/4	86.39	50.72	45.80	4.69	2.16	120	45.1	7.8
T115C	1/8	99.74	51.35	46.50	4.55	2.07	670	45.6	8.3
T115D	0	115	51.96	46.71	5.88	3.01	200	47.5	8.6
T120	1	66.99	55.01	50.10	5.75	2.61	4000	47.7	16
T120A	1/2	79.55	55.08	49.16	4.60	2.60	460	50.6	15
T120B	1/4	90.11	53.41	48.21	4.65	2.52	250	48.2	8.0
T120C	1/8	103.3	54.94	49.79	4.31	2.03	350	51.8	11
T120D	0	120	56.11	50.52	4.75	2.18	1200	51.8	14
T121A	1/2	73.09	54.67	49.14	4.74	2.03	460	50.9	11
T122A	1/2	73.94	56.06	49.76	6.05	2.24	12000	44.9	31
T123A	1/2	74.38	55.79	50.38	5.36	1.74	3900	50.2	17
T124A	1/2	74.39	56.85	50.58	6.24	2.30	12000	46.9	35
T125	1	69.21	57.49	51.75	5.49	1.78	6500	50.3	13
T125A	1/2	81.38	57.12	51.20	5.79	1.90	8600	51.8	16
T125B	1/4	92.24	57.08	51.53	5.44	1.70	4900	50.9	15
T125C	1/8	107.1	57.58	52.08	5.69	2.43	11000	49.0	14
T125D	0	125	56.20	51.75	4.89	2.58	7400	47.8	11
T130	1	71.00	60.50	54.62	6.75	2.41	15000	50.8	23
T130A	1/2	79.69	60.20	54.28	6.03	1.81	10000	51.3	33
T130B	1/4	94.26	58.28	53.48	8.16	3.75	13000	48.4	27
T130C	1/8	110.6	61.91	56.10	8.99	3.95	16000	49.0	31
T130D	0	130	59.96	54.28	2.04	2.04	25000	38.8	41
T135	1	71.37	64.04	56.60	5.43	3.83	140	18.9	42
T135A	1/2	85.71	65.42	56.36	5.56	3.27	19000	43.3	38

Table 2
(Continued)

Mass (M_{\odot})	Mass Loss	M_{preSN} (M_{\odot})	M_{He} (M_{\odot})	M_{CO} (M_{\odot})	M_{Si} (M_{\odot})	M_{Fe} (M_{\odot})	Duration (10^7 s)	M_{final} (M_{\odot})	KE^{eject} (10^{50} erg)
T135B	1/4	97.54	61.15	55.30	5.39	3.05	18000	42.9	35
T135C	1/8	107.2	60.14	54.71	2.41	2.07	4500	23.2	31
T135D	0	135	63.91	57.54	4.37	2.84	4300	35.0	39
T140	1	75.29	65.63	58.32	5.48	0	44
T140A	1/2	89.64	65.90	59.55	5.54	1.95	200	4.5	41
T140B	1/4	99.08	65.01	59.06	4.25	2.65	110	29.2	38
T140C	1/8	108.6	63.87	57.96	6.04	0	48
T140D	0	140	65.24	59.19	5.20	2.63	21000	37.4	33
T150	1	76.38	71.63	64.73	6.83	0	120
T150A	1/2	95.98	70.89	64.20	5.99	0	70
T150B	1/4	106.4	69.05	62.76	6.11	0	60
T150C	1/8	113.4	70.17	63.94	5.93	0	71
T150D	0	150	70.18	64.86	6.41	0	98

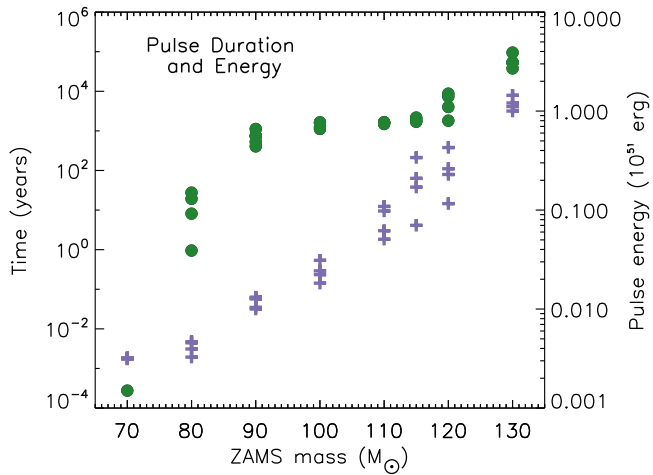


Figure 8. Pulse duration in years (blue crosses) and total kinetic energy in all of the ejected shells in units of 10^{51} erg (solid green circles) as a function of the main-sequence mass in M_{\odot} for full stars of 10% solar metallicity evolved until iron core collapse. The duration of pulsing activity and total energy are highly correlated with weak explosions also having short duration. From 90 to 120 M_{\odot} , the explosion energy is nearly constant even though the timescale varies significantly. Fewer pulses each carrying more energy happen for the heavier stars.

variations are seen for the silicon and iron core masses due to the interaction of burning of multiple convective shells of carbon, neon, and oxygen (Sukhbold et al. 2016). Major differences exist for some pulse durations and explosion energies, such as in Models T115 and T115A, because the tamping effect of the hydrogen envelope influences the expansion of the exploding core and the interval to the next pulse. The helium and CO cores are also typically a bit larger for the models with full mass loss since so much of the envelope is lost that the convective dredge-up of helium near the end of the star’s life is reduced. Generally though, explosion energies and durations increase with mass.

Table 2 and Figure 8 give the presupernova mass, prior to any pulsing activity, and the masses of helium, CO, silicon, and iron cores where they existed in hydrostatic equilibrium. The hydrogen envelope mass is the presupernova mass minus the helium core mass. Also given is the total duration of the pulses, again measured from the first pulse until core collapse, the final

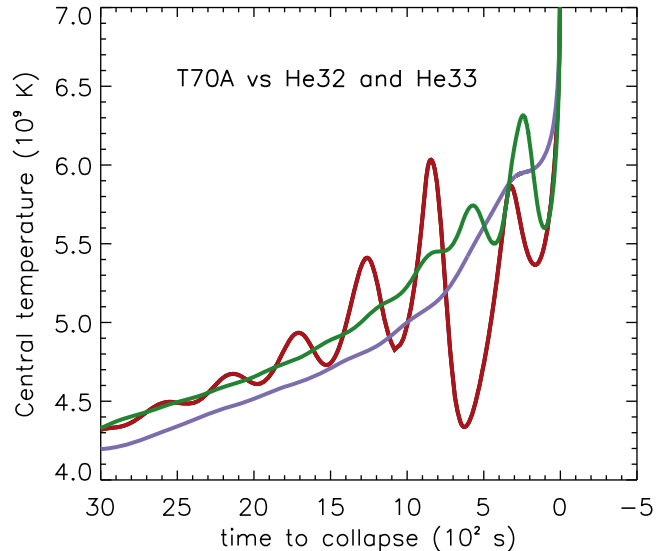


Figure 9. Central conditions during the last 3000 s before core collapse for Model T70A, which has a helium core mass of $30.1 M_{\odot}$, and the 32 and 33 M_{\odot} helium cores studied in Section 3. He33 is the red line. Blue is He32 and green is T70A.

mass of the bound remnant after all pulses ceased, and the total kinetic energy of all matter ejected by the pulses.

4.1. 70–80 M_{\odot} : Faint SNe IIP

Regardless of envelope mass, the helium core mass for nonrotating $70 M_{\odot}$ stars is in the range 29 – $32 M_{\odot}$ (Table 2). Similarly, for $75 M_{\odot}$ stars, the helium core mass is 32 – $34 M_{\odot}$. Helium cores of this mass are marginally stable (Table 1), but a more relevant quantity is the CO core mass, which is larger for Models T70 and T75 than for the equivalent helium cores evolved at constant mass. Figure 9 shows that the central temperature history for Model T70A is actually intermediate between those of Models He32 and He33 even though the actual helium core mass of T70A is $30.1 M_{\odot}$. This implies an offset in helium core mass of about $2 M_{\odot}$. The boundary pressure of the hydrogen shell is small. One must go less than $0.1 M_{\odot}$ into the core before the pressure rises by a factor of 2. The offset reflects more the growth of the helium core by hydrogen shell burning in the full stars while convective central

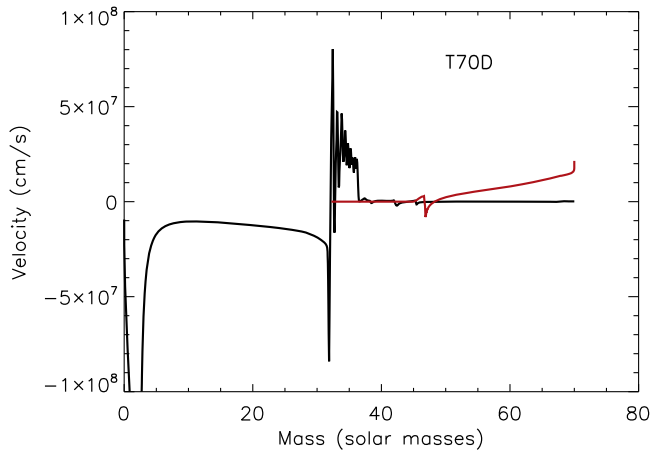


Figure 10. Velocity in Model T70D at the time the iron core collapses to a protoneutron star. Multiple pulses have resulted in the accumulation of energy and momentum in the hydrogen envelope just outside the helium core edge at $30.1 M_{\odot}$. These pulses merge into a weak shock that propagates through the envelope and ejects about $20 M_{\odot}$ of material with kinetic energy 1.5×10^{48} erg (red line).

helium burning is in progress. As a result, the helium convection zone grows and, in the end, a larger CO core mass is produced. The CO core in T70A is $26.41 M_{\odot}$, more like the CO cores in He32 and He33 ($26.3 M_{\odot}$ and $27.2 M_{\odot}$, respectively) and considerably larger than the CO core in He30 ($24.65 M_{\odot}$). Similar behavior was noted by Woosley et al. (2007).

Figure 10 shows the velocity structure in Model T70D at the time when the iron core collapses (note the high negative speed in the inner $2 M_{\odot}$). Numerous low-energy pulses have already steepened into shocks in the density gradient at the edge of the helium core and are accumulating at the base of the hydrogen shell. After the helium core collapses, presumably to a black hole, these pulses continue out through the envelope, eventually merging into a single shock wave. The momentum of the small amount of matter that initially moves with high speed must be shared with the large mass of the envelope though, so the speed slows. Peak velocities are only $\sim 100 \text{ km s}^{-1}$ (red line, Figure 10).

In Models T70A and T70B, the pulses were so weak that the shock died in the envelope without ejecting any discernible matter. The implicit hydrodynamics in KEPLER damps very weak shocks numerically, so the possibility of some small, low-velocity ejection is not ruled out. In the other two $70 M_{\odot}$ models, though, and in all of the $75 M_{\odot}$ mass models, part of the hydrogen envelope was ejected, about $1 M_{\odot}$ in Model T70C and about $18 M_{\odot}$ in Model T70D. These ejections had very little kinetic energy (Table 2), for example, 5×10^{46} erg in Model T70C and 1.5×10^{48} erg in Model T70D. These energies were far less than the binding of the entire envelope, about 3×10^{49} erg, so most of the envelope may fall into the black hole. The mass ejection did power some faint, light curves, however (Figure 11). Typical temperatures for Models T70C and T70D were 3000–4000 K on the “plateau” with photospheric speeds of only 50 – 150 km s^{-1} . For the $75 M_{\odot}$ models (Figure 12), the temperatures were more like typical SNe IIP ~ 6000 K. The light curves were also a bit brighter, though still fainter than normal SNe IIP. The expansion speeds were still very slow, 100 – 200 km s^{-1} . Similar low-energy light curves have also been studied by

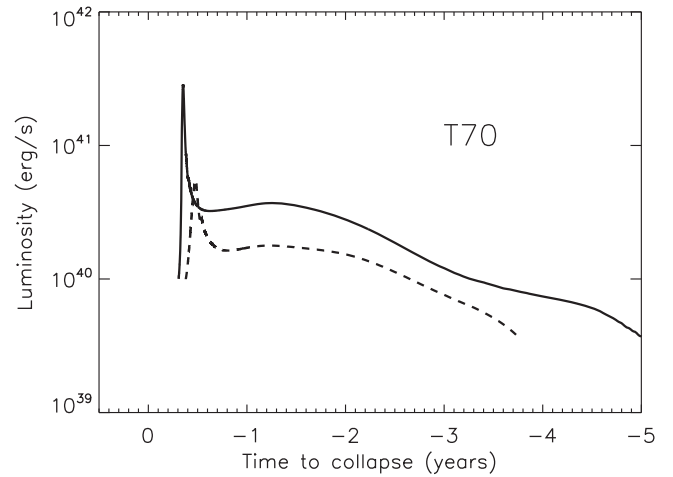


Figure 11. Light curves for two of the $70 M_{\odot}$ models (T70C and T70D). Time is measured in years relative to the time when the iron core collapses. Negative time is postcollapse. These very low energy explosions eject only a fraction of their hydrogen envelopes and have very faint light curves that, well after shock breakout, are red and have low velocities, ~ 50 – 150 km s^{-1} .

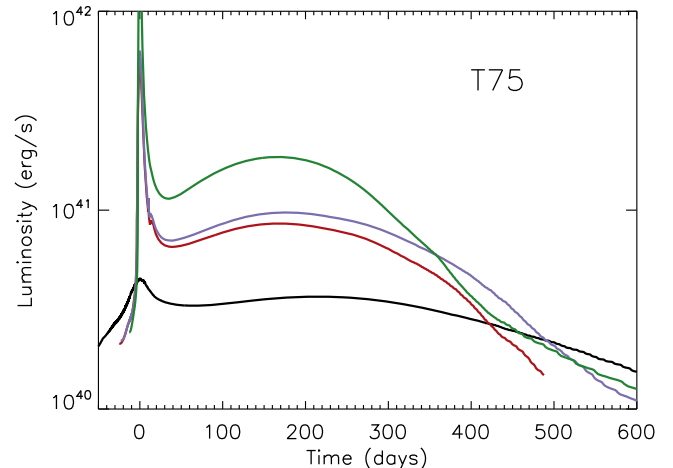


Figure 12. Light curves for the four $75 M_{\odot}$ models. The curves are for models with different mass loss rates: T75A (black), T75B (red), T75C (blue), and T75D (green). See Table 2. Slightly more energetic than the T70 models (Figure 11), these low-energy explosions still eject only a fraction of their hydrogen envelopes and have faint light curves that after shock breakout have very low velocities, ~ 100 – 200 km s^{-1} , and last a year or more. The colors on the plateaus are typical of SNe IIP, ~ 6000 K.

Lovegrove et al. (2017), especially their bright, brief, blue shock breakout phases.

The PPI is considerably stronger in an $80 M_{\odot}$ model. The total energy in pulses, $\sim 10^{50}$ erg, is still only about 10% that of an ordinary SN IIP, and the duration of the pulses, roughly a day, is short compared with the duration of the light curve. The result is a single, subenergetic SN IIP (Figure 13). Typical expansion speeds have risen to 200 – 800 km s^{-1} (T80A) and 300 – 1000 km s^{-1} (T80B, T80C, T80D). These would probably be SNe IIn.

Together, these models in the 70 – $80 M_{\odot}$ range should be roughly half as frequent in nature as the 100 – $130 M_{\odot}$ stars to be discussed later that might make SLSN. They are obviously more difficult to detect, but their very low expansion speeds, faint emission, and long duration are distinctive. Some might be even classified as “supernova impostors” (Smith et al. 2011).

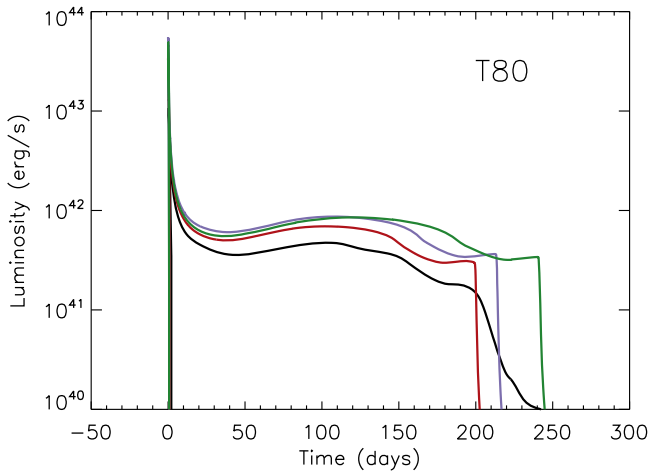


Figure 13. Light curves from the $80 M_{\odot}$ low-metallicity models. The curves are for models with different mass loss rates: T80A (black), T80B (red), T80C (blue), and T80D (green). See Table 2. All light curves are single events similar in appearance to faint SNe IIP with explosion energies $\sim 10^{50}$ erg or less (Lovegrove et al. 2017). Models with larger envelope masses have systematically longer plateaus.

The brighter ones might be SNe IIn, especially if they had appreciable mass loss before starting to pulse.

4.2. $80\text{--}90 M_{\odot}$: Ordinary SNe II

By $90 M_{\odot}$, the total energy of the pulses has become an appreciable fraction of 10^{51} erg, and that energy is still being deposited over a time short compared with the $\sim 10^7$ required for the envelope to expand and recombine (Figure 14). Shells collide while the star is still very optically thick. The result is a single ordinary-looking SN IIP, with several exceptions: (1) the duration for the PPISN may be longer than for typical SNe IIP, depending upon how much of the envelope has been lost; (2) the photospheric speed is slower, typically varying from 1000 to 2500 km s^{-1} on the plateau; (3) if the progenitor is an RSG, the initial radius is unusually large, and so too is the initial luminosity; (4) the mass loss rate may have been unusually high just before the explosion; (5) the metallicity is low; and (6) no radioactivity is ejected. The light curve thus has no ^{56}Co -powered “tail.” At the end of the plateau, the light curve plummets. Circumstellar interaction may add an appreciable late-time component, though that could mimic a tail (Section 12). Careful study of the decay timescale and a spectroscopic search for narrow lines might be necessary to distinguish this from radioactive decay.

4.3. $90\text{--}105 M_{\odot}$: Long, Irregular SNe IIP

In this interesting mass range, the duration of the pulses roughly equals or slightly exceeds the length of the plateau phase of the supernova ($\sim 100\text{--}200$ day). Depending upon the mass of the hydrogen envelope, repeated pulses can lengthen, brighten, and add noticeable structure to the light curves of some events and provide late-time activity in others, but there is still just one supernova. Figure 16 shows the light curves for four representative cases (Table 2). Some models, like T100C, are very luminous for a long time. Roughly one-quarter of the 6.9×10^{50} erg of kinetic energy in the pulses is converted into light here, and the supernova might be categorized as “superluminous.”

For perhaps the last time, the supernova has, throughout its duration, a well-defined photosphere. Typical effective temperatures, well after shock breakout, are around 6000 K.

4.4. $105\text{--}120 M_{\odot}$: Multiple Supernova and Long, Luminous Events

A further increase in mass results in energetic pulses that continue longer than the duration of any single supernova. The first pulse ejects what is left of the hydrogen envelope. Typically this matter is helium rich, and its ejection results in a light curve (Figure 17) that resembles an ordinary SNe IIP. If the envelope is massive and the pulse energy not unusually large, most of the ejecta move at a relatively slow speed, around 1000 km s^{-1} . This matter will later provide the “anvil” against which later, faster-moving ejecta will strike. Most of the emission from these later mass ejections is from the forward shock of the last shell ejected, though the reverse shock can contribute to the luminosity since the mass of the second ejection is usually less than the first. Both forward and reverse shocks cause the pileup of matter in the dense thin shell that subsequent pulses can encounter.

For example, consider Models T110B and T110C (Figure 17). For T110B, several energetic pulses in rapid succession impart a kinetic energy to the envelope of 5.1×10^{50} erg. The presupernova mass was $84.1 M_{\odot}$, and this first explosion ejects $35.3 M_{\odot}$ at an average speed of $\sim 1300 \text{ km s}^{-1}$, reducing the star’s mass to $48.8 M_{\odot}$, essentially the bare helium core.

There follows, in Model T110B, a quiescent period of about 2 yr during which no additional explosion occurs. The ejecta from the first pulse expand and thin, eventually becoming transparent. At that point, unless the formation of dust intervenes, one might see directly to the helium core, which would resemble a Wolf-Rayet star, but with several complications. First the WR star is not shining by nuclear reactions, but by gravitational contraction. The luminosity may be almost the same, near Eddington, and the star may even have a wind, but its radius, at least initially, is larger than a WR star of the same mass. Moreover, substantial matter from the first ejection falls back and accretes. This can contribute to the luminosity but also partially obscures the star. Generally though, one finds luminosities near $10^{40} \text{ erg s}^{-1}$ and radii of a few to 10×10^{11} cm. The underlying spectrum is thus very hot, $\sim 10^5$ K, and the radiation may ionize some of the surrounding material. A more physical treatment of the radiation transport problem is needed than is feasible here.

The contracting core of Model T110B encounters the PPI again 2.7 yr later, launching a second set of pulses (Figure 17). This time a smaller amount of mass, $4.1 M_{\odot}$, is ejected, but with a comparable energy, 2.3×10^{50} erg, and higher speed, $2000\text{--}3500 \text{ km s}^{-1}$. The fast ejecta overtake the previously ejected envelope and slam into it, giving rise to a second bright, collisionally powered display. The matter first impacted is the inner part of the former envelope, moving at about $500\text{--}700 \text{ km s}^{-1}$ and located at about 5×10^{15} cm, an ideal radius for converting kinetic energy into optical light and radiating it without much adiabatic degradation. Depending upon the uncertain opacity assumed for the matter external to the shock, the emitting region may be optically thin or nearly so, so the complete thermalization of the emitted light is questionable. Even more problematic is the tendency of the second mass ejection to pile up all of the matter it encounters

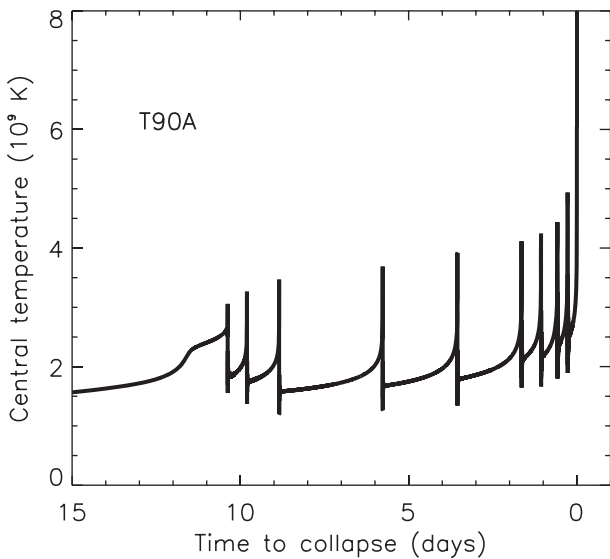


Figure 14. Left: the pulsing activity of the low-metallicity $90 M_{\odot}$ Model T90A is reflected in its central temperature. Time is in units of 10^5 s measured backward from the time the iron core collapses. The total duration of the pulsing activity is 1.1×10^6 s (Table 2), which is less than the shock crossing time for the envelope, so shock waves pile up there and eventually merge into a single explosion with a smooth plateau (Figure 15). The right frame shows the velocity structure in units of thousands of km s^{-1} at time zero in the left frame (core collapse).

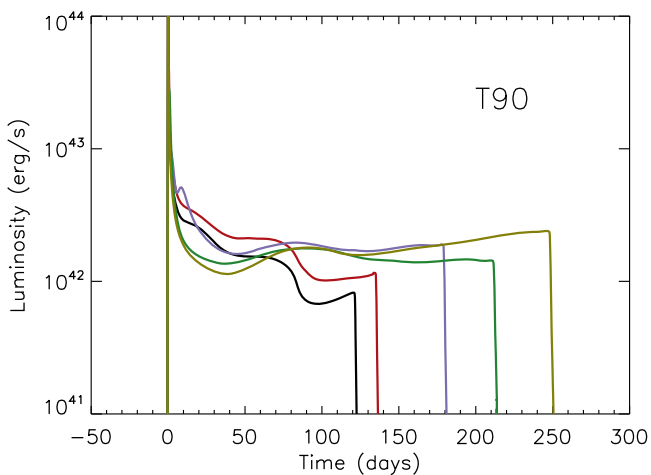
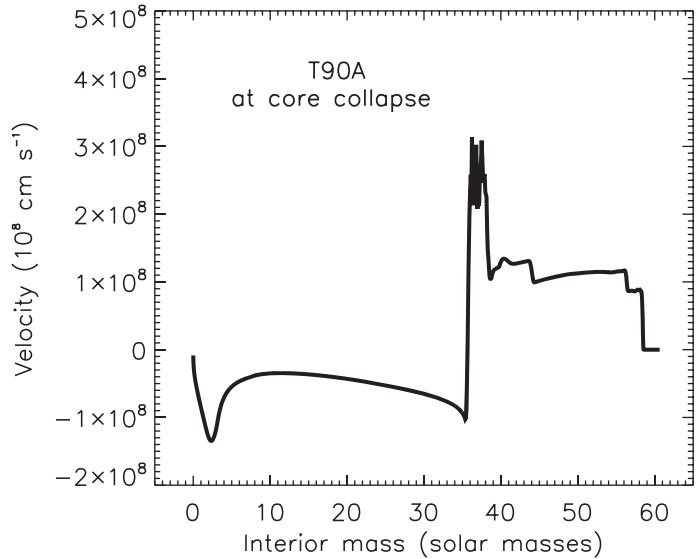


Figure 15. Light curves for the $90 M_{\odot}$ low-metallicity models. The curves are for models with different mass loss rates: T90 (black), T90A (red), T90B (blue), T90C (green), and T90D (gold). See Table 2. The luminosity on the plateau is similar to common SN IIP, although a bit faint. Models with larger envelope masses have systematically longer plateaus. There are no radioactive tails unless one results from circumstellar interaction.

into a very thin, high-density shell moving at nearly constant speed. As time passes, a large fraction of the total ejecta is contained in such shells. This is unphysical, and resolving their progress poses numerical difficulty for the 1D code. Future radiation transport calculations need to be done in 2D or with some artificial means to keep the shells from becoming unphysically thin.

Given these difficulties, the effective temperature cannot be accurately calculated for these and heavier models, though the bolometric light curve, which is essentially just $L = 2\pi R_{\text{shock}}^2 \rho v_{\text{shock}}^3$, can. Here ρ is the density ahead of the shock, a residual of the earlier mass ejection. Figure 17 shows several episodes of high luminosity, including unphysically sharp spikes as the thin shells from the last two pulses first run into each other and then into the first ejection. Additional structure

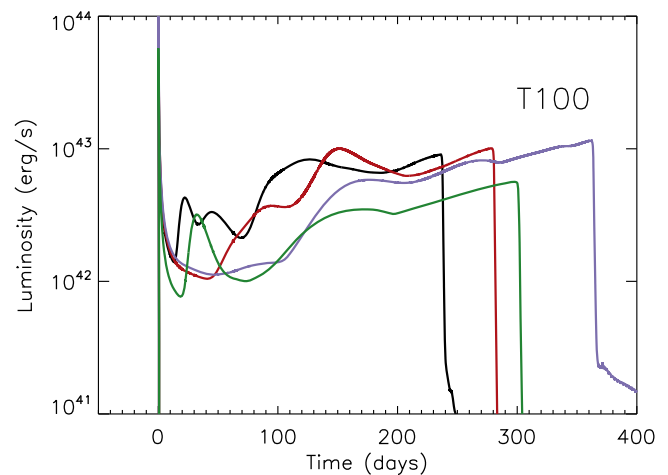


Figure 16. Light curves from the $100 M_{\odot}$ low-metallicity models. The curves are for models with different mass loss rates: T100A (black), T100B (red), T100C (blue), and T100D (green). See Table 2. The structure from individual pulses is now starting to become apparent, and the light curve is powered by a combination of recombination-released shock energy and colliding shells. Generally, models with larger envelope masses have longer plateaus, but Model T100C is exceptionally long due to the longer duration of the pulsing phase. The integrated light in these four curves is 1.2 , 1.4 , 1.7 , and 0.8×10^{50} erg for Models T100ABCD.

is imprinted by a dense shell associated with the formation of a reverse shock during the first mass ejection. Altogether 1.6×10^{50} erg of light is emitted in the lengthy second outburst shown in Figure 17. This is about one-half of the total kinetic energy of the second set of pulses.

Model T110C is qualitatively similar, suggesting that the answer is not very sensitive to the choice of mass loss rate as long as the envelope is not removed. Initial pulses eject $47.2 M_{\odot}$, including the entire hydrogen envelope, with an energy of 3.6×10^{50} erg, leaving a core of $48.8 M_{\odot}$. Another $4 M_{\odot}$ is ejected with energy 3.5×10^{50} erg 1.7 yr later. This runs into envelope material at about 10^{15} cm moving at about

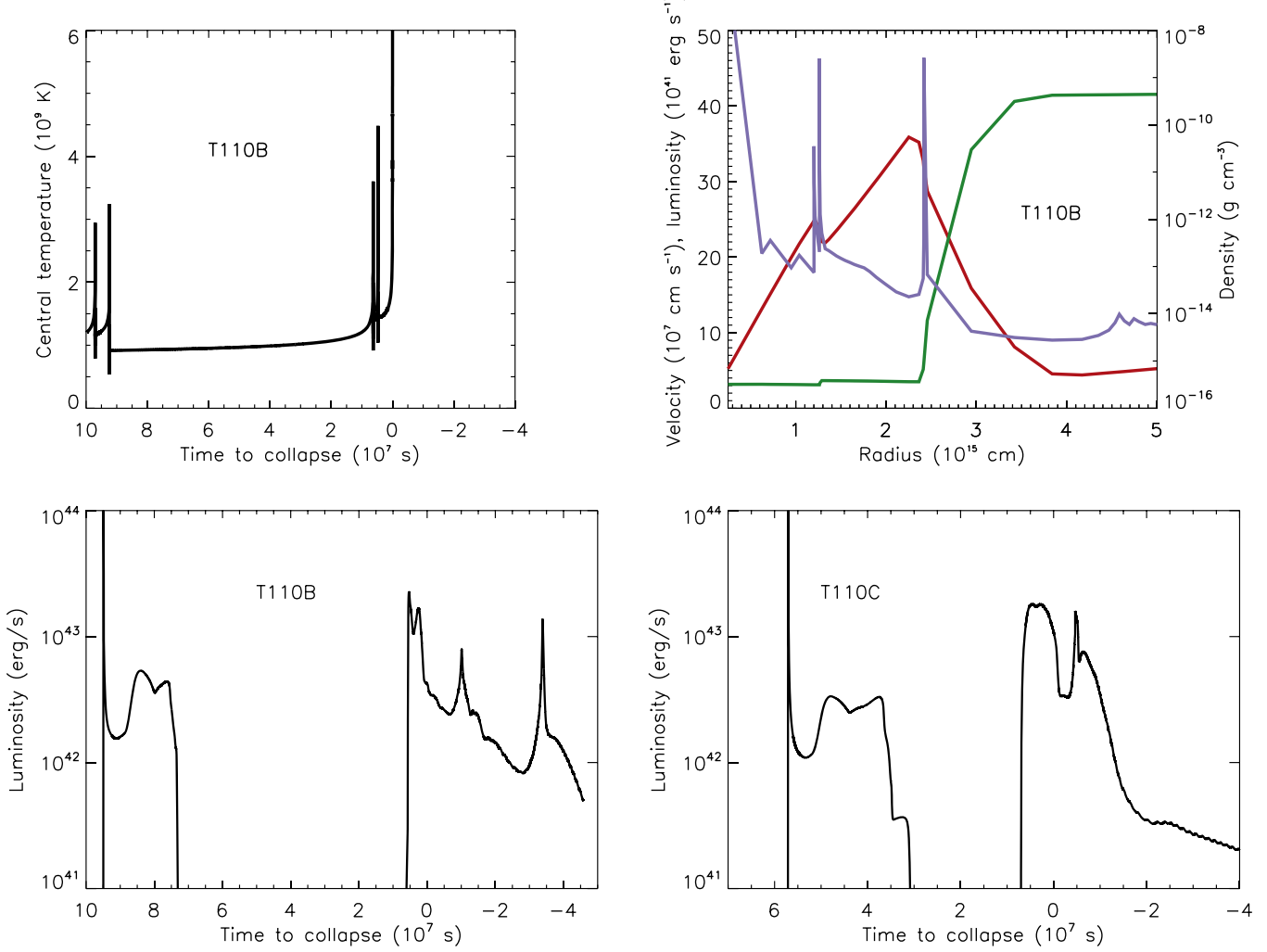


Figure 17. Pulses and light curves for Models T110B and T110C. Top left: the first two pulses in Model T110B 9.5×10^7 s before iron core collapse eject the hydrogen envelope and then impact it again, producing a structured Type IIP-like light curve with a secondary maximum (lower left). There then ensues a 2.7 yr delay as the core contracts in a Kelvin–Helmholtz phase. This is followed by several strong pulses that eject an additional $4.1 M_\odot$, mostly of helium, with an energy of 2.3×10^{50} erg and speed $2000\text{--}3500 \text{ km s}^{-1}$. A short time later the iron core collapses, though the light curve continues to be powered by collisions for a long time afterward. Lower left: the light curve reflects the interaction among the ejected shells. The emission was rising toward a third sharp peak when the code became unstable due to the thin shells. Top right: the density (blue; g cm^{-3}), velocity (red; 10^7 cm s^{-1}), and luminosity (green; $10^{41} \text{ erg s}^{-1}$) structures in the ejecta are shown at the time the iron core collapses. The luminosity chiefly originates from the collision at $2.5 \times 10^{15} \text{ cm}$. Note the unphysical pileup of most of the ejected matter in very thin, dense shells. Lower right: the light curve for Model T110C is similar, but smoother because of the larger mass ejected.

$400\text{--}1000 \text{ km s}^{-1}$, giving rise to the bright display in Figure 17. In the second display, 1.8×10^{50} erg is radiated.

Other heavier models in Table 2 with total pulsational durations less than about 10 yr show behavior and light curves similar to the $110 M_\odot$ models. For example, Model T115A resembles 110B and 110C, but has three well-spaced, strong pulses at $13.2, 7.8$, and 0.67×10^7 s before core collapse. Once again the narrow spikes in the light curve, except for the first breakout transient, would be broader but contain about the same total energy in a 2D simulation. For Model T115B though (not shown), the interval between pulses has become so long (39 yr) that the radius where the shock interaction takes place was well beyond 10^{16} cm and the efficiency for optical emission is uncertain.

Besides producing repeating supernovae, energetic pulses that happen over a time span of years are of interest for producing SLSN. With typical speeds of 1000 km s^{-1} , the first ejection moves to a few times 10^{15} cm in a year. That is an optimal radius for converting kinetic energy into a supernova-

like display. Unfortunately, while some of the light curves are indeed much brighter than common supernovae, the total light emitted was only a fraction of 10^{51} erg and did not rise to the level of the brightest “superluminous” supernovae. This is a dilemma to which we shall return in Sections 8 and 12.

PPISN in the upper end of this mass range could also give rise to supernovae of mixed typology. Since the first pulse ejects the hydrogen envelope, with a delay of years to centuries until the next outburst, the supernova might initially present as Type Ib and later turn into a IIn. An example would be Model 115B. Here, several initial pulses eject the hydrogen envelope of about $36 M_\odot$ with an energy of 3.8×10^{50} erg and typical speeds of 1000 km s^{-1} . A model with more mass loss would have ejected less mass with greater speed. Two more pulses with a combined energy of 2.2×10^{50} erg eject an additional $5.2 M_\odot$ of helium core 39 yr later. The collision of these two shells produces a supernova, presumably of Type Ib, since the photosphere and shock were in the helium layers. The merged shell then encountered the slowest-moving hydrogen at

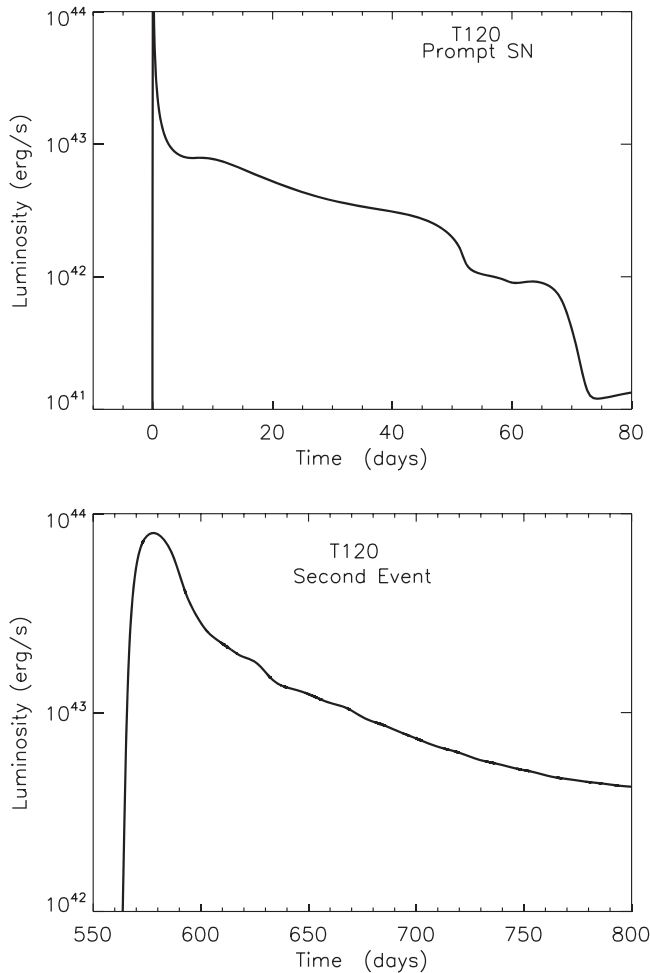


Figure 18. The first pulse in Model T120 produces an SN IIP (upper frame), which declines rapidly with time once the denser inner envelope of the presupernova star is encountered. If the presupernova star had been a BSG, this initial display would have been much fainter (Section 6). 18 months later, a second very bright supernova is produced as the ejecta of additional pulses run into the ejected envelope and reheat it. During this second outburst, 3.3×10^{50} erg is radiated. The iron core collapses 1200 yr after that.

3×10^{16} cm about 3 yr later. The peak luminosity of the Type Ib supernova was 4×10^{42} erg s $^{-1}$. These results resemble SN 2014C, which, though born a Type Ib switched to Type IIn about a year later (Milisavljevic et al. 2015), although the authors say that this particular supernova was too light to have been a PPISN.

4.5. 120–140 M_{\odot} : Bright Circumstellar Interaction and Delayed Supernovae

4.5.1. Interaction with the Ejected Envelope

For the heaviest PPISN, the interval between the ejection of the envelope and the later pulses is so long that the envelope expands out of the radial range where optically bright supernovae are expected from the interaction. Any subsequent shocks will interact with a medium that is optically thin, at least to electron scattering. The duration of the collision will be years or even centuries, so the luminosity required to emit the differential kinetic energy is lower. The collision may produce X-rays and radio emission as well as optical emission. An example of an SN IIn in this state, although not necessarily a PPISN itself, is SN 1996er (Meunier et al. 2013), which is

currently interacting with several solar masses of ejecta at about 10^{17} cm.

The qualitative nature of these events can be inferred from the timescales for pulsational duration given in Table 2. Assume the first pulse ejects the envelope at 1000 – 2000 km s $^{-1}$ and later pulsations eject shells of helium and heavy elements at 4000 km s $^{-1}$. The collision with the envelope then happens at $\sim 10^{18}$ cm when the timescale is centuries and at $\sim 10^{19}$ cm when it is millennia. To dissipate a kinetic energy of 10^{51} erg, a characteristic shock luminosity would be 10^{40} – 10^{41} erg s $^{-1}$. The emission might resemble what is presently transpiring in SN 1987A, where the material ejected in the equatorial ring about $\sim 10,000$ yr ago is being impacted by high-velocity matter (e.g., Sugerman et al. 2005). The display from a PPISN would differ in that it would be approximately spherically symmetric and the velocities slower. The supernova remnant would also contain the central star, still glowing with a luminosity comparable to the circumstellar interaction.

Consider, for example, Model T123A. The first pulse in this model ejected the star’s envelope, producing a typical SN IIP that lasted ($L > 10^{42}$ erg s $^{-1}$) for roughly 120 days. The mass of the ejected material was $17.8 M_{\odot}$, and its kinetic energy was 1.1×10^{51} erg. Velocities ranged from 1000 to 3000 km s $^{-1}$ in most of the ejecta. A bound remnant of $56.6 M_{\odot}$ was left, the outer few tenths M_{\odot} of which still contained appreciable hydrogen. The central temperature of the remaining star, after a few brief oscillations, was 5.4×10^8 K. Over the next 1010 yr, the core contracted, eventually encountering the PPI a second time. By then, most of the former envelope had coasted to between 1 and 10×10^{18} cm, with about $10 M_{\odot}$ inside 5×10^{18} cm. This second pulse ejected $6.4 M_{\odot}$, consisting chiefly of helium, with an energy of 6×10^{50} erg, that ran into the ejected envelope. The collision produced a low-luminosity, $\sim 10^{40}$ – 10^{41} erg s $^{-1}$ event that continued for centuries until most of the kinetic energy of the second pulse was radiated away. Some 220 yr after the second pulse, the iron core collapsed, presumably to a black hole. There were no later pulses. This behavior was typical for stars in the 120–130 M_{\odot} range, especially for those models with total explosion energies (Table 2) below 3×10^{51} erg.

4.5.2. Late Pulsations and Bright Supernovae

In addition to enduring circumstellar interaction, some of the models in this mass range also produced a second bright supernova after a very long delay. Their evolution was similar to the heaviest helium cores discussed in Section 3.2 that also produced delayed supernovae, but here the initial explosion was brighter and there would be hydrogen in the spectrum. A strong initial pulse ejects the envelope, and, after a long delay, two or more pulses, shortly before the star dies, collide with one another, powering a second supernova. Model T130D is a particularly energetic example. The large envelope mass in this model (Table 2) is due to the complete neglect of mass loss, but other combinations of main-sequence mass and mass loss give a similar core structure and late-time light curve. Three of the four $135 M_{\odot}$ models were similar, as well as some of the more energetic cases between 120 and 130 M_{\odot} (T122A and T124A for example). Model T130D had three strong pulses, the first of which ejected the $70.0 M_{\odot}$ envelope, giving the usual SN IIP (Figure 19). This first pulse was quite strong, 1.5×10^{51} erg, and almost unbound the star. Following relaxation to hydrostatic equilibrium after the pulse, the central temperature was

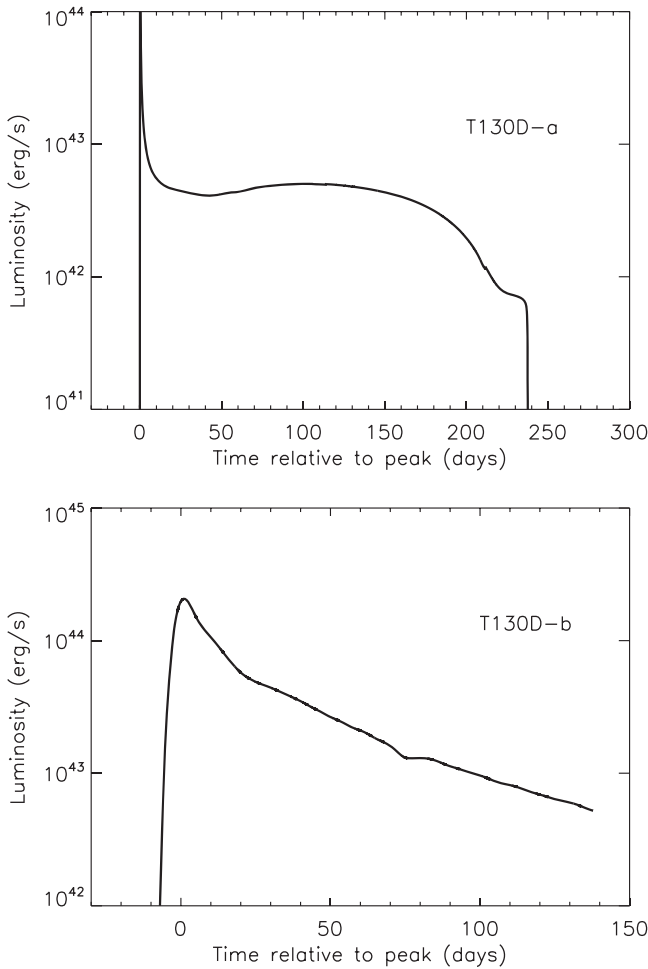


Figure 19. Light curves from Model T130D. The top frame (Model T130D-a) gives the bolometric light curve resulting from the first pulse and envelope ejection. Some 3260 yr later, pulses 2 and 3 in rapid succession collided with one another, producing the bright light curve shown in the lower panel, Model T130D-b.

only 2.8×10^8 K. Some 3300 yr later, the core experienced a second instability and ejected $7.7 M_\odot$ of helium, C, and O with an additional 1.1×10^{51} erg of kinetic energy. Eight months after that, a third and final very deep bounce ejected $13.5 M_\odot$ with 1.5×10^{51} erg. The peak central temperature reached during this last pulse was very hot, 5.95×10^9 K, sufficient to produce $1.8 M_\odot$ of ^{56}Ni (that was not ejected). This $13.5 M_\odot$ collided with the shell ejected by the second pulse at a radius of $\sim 10^{15}$ cm, producing a very luminous supernova, T130D-b in Figure 19. Because the collision was between two shells mostly devoid of hydrogen, this would probably have been an SN Ibn or SN Icn, though perhaps with some hydrogen lines from the outer edge of the second mass ejection. The total energy in light was 4.5×10^{50} erg, or about one-third of the energy in the last pulse. This was the most energy in light found for any PPISN in the present study that did not invoke magnetar formation.

The postexplosion structure of Model T130D was affected by its large ^{56}Ni production. After a brief stage of adjustment to hydrostatic equilibrium following the last pulse, the iron core mass, including the $1.8 M_\odot$ of ^{56}Ni , was $3.54 M_\odot$, and the silicon plus iron core was $5.82 M_\odot$. The time since the onset of

Table 3
Solar Metallicity Models

Mass (M_\odot)	Mass Loss	M_{preSN} (M_\odot)	M_{He} (M_\odot)	M_{CO} (M_\odot)
S80B	1/4	40.47	34.71	30.25
S80C	1/8	55.95	36.48	32.00
S90B	1/4	48.01	40.07	35.29
S90C	1/8	65.30	41.06	36.00
S100B	1/4	48.92	44.90	38.86
S100C	1/8	72.59	41.00	41.00
S110C	1/8	63.70	50.85	45.16
S120C	1/8	71.31	53.67	47.27

pulsing activity was 1.0×10^{11} s. Over the next 1.5×10^{11} s, the core experienced a lengthy Kelvin–Helmholtz contraction. During the first few months, the decay of ^{56}Ni to ^{56}Fe powered extensive convection. This resulted in the full mixing of material from $2.04 M_\odot$ out to $29.4 M_\odot$, that is, almost the entire remaining star. As a result, the compositional distinction between “iron core,” “silicon core,” and “oxygen core” became blurred. Several other massive models also produced a lot of ^{56}Ni and experienced extensive mixing powered by radioactive decay, Model T120A for example.

5. Stars with Solar Metallicity

A smaller grid of solar metallicity models was also calculated (Table 3). In order to leave helium cores sufficiently massive that the PPI is encountered, a substantial reduction in the mass loss rate was required (Section 2.2), roughly a factor of 4–8. Given the low mass loss and a nontrivial hydrogen envelope at the end, the outcome for nonrotating solar metallicity models is similar to those with lower metallicity (Table 2). For example, Models T80 leave a helium core mass of $35 \pm 1 M_\odot$, the same as Models S80C and S80D. The CO core masses are also similar. Since the final evolution for nonrotating stars depends chiefly on the helium core mass, the outcome will be the same.

There are interesting differences in the envelope structure, however. The effect of the “iron bump” on the opacity is more pronounced in the solar metallicity models. This gives them larger radii and, in some cases, makes the models difficult to converge. Large density inversions develop when the mass of the convective envelope is small and the local luminosity is close to Eddington (e.g., Sanyal et al. 2015). These difficulties inhibited the study of masses above $120 M_\odot$ or mass loss rates so large that most or all of the hydrogen envelope was lost. Models S110B and S120B (not given in the table) had mass loss rates so high, even with 25% of the standard value, that they would have lost their envelopes and become Wolf–Rayet stars. Some of these cores might become PPISN, but most would have continued to lose so much mass that they would have died short of the $30 M_\odot$ required for the PPI.

6. Luminous Blue Progenitors

The “T” series (Table 2) and “S” series (Table 3) models ended their lives as RSGs with photospheric radii $\sim 10^{14}$ cm. Other recent theoretical studies (e.g., Chen et al. 2015) also show stars with 10% solar metallicity and masses up to $150 M_\odot$ ending their lives as RSGs. These results might be regarded as inconsistent, however, with observations showing that stars

Table 4
Blue Star Models

Mass (M_{\odot})	M_{He} (M_{\odot})	M_{H} (M_{\odot})	L_{preSN} ($10^{40} \text{ erg s}^{-1}$)	T_{eff} (10^3 K)	Duration (10^7 s)	M_{final} (M_{\odot})	KE_{eject} (10^{50} erg)
B80	35.1	10.5	0.62	23.9	0.0016	44.1	0.042
B90	39.2	10.6	0.71	25.0	0.102	36.4	4.1
B95	43.0	10.8	0.80	26.1	0.215	38.8	5.6
B100	44.8	10.8	0.83	26.6	1.11	39.2	8.1
B105	47.4	10.8	0.89	27.5	6.32	43.5	6.3
B110-5	49.8	6.0	0.92	45.8	33.2	44.9	7.9
B110	49.8	10.9	1.01	31.1	13.9	45.1	8.7
B110-20	49.9	21.0	1.06	26.3	16.4	45.5	7.6
B115-5	51.8	4.9	0.97	48.9	17.7	45.9	7.3
B115	51.9	11.0	1.01	29.4	14.6	45.3	11.5
B115-20	52.0	19.3	1.11	31.8	45.4	46.3	8.6
B120	55.1	10.8	1.06	30.7	199	50.9	11.8

above about $35 M_{\odot}$, the “Humphreys–Davidson limit” (Humphreys & Davidson 1979), do not spend a significant part of their lifetime as RSGs, even in the SMC (Massey & Olsen 2003; Levesque et al. 2007), where the metallicity is about one-seventh solar. Given the possible tension between theory and observations, it is worth exploring the consequences of both BSG and RSG progenitors for PPISN.

While technically RSGs, many of the T-series models with high mass loss rates actually had an envelope structure that, except for a relatively small amount of mass near the surface, was “BSG-like.” Presupernova Model T120, for example, had a hydrogen envelope of $11.98 M_{\odot}$ and a photospheric radius of $9.5 \times 10^{13} \text{ cm}$, but only the outer $0.83 M_{\odot}$ of that envelope was convectively unstable and had a low density. The radius at the base of this surface convective shell was $4.5 \times 10^{12} \text{ cm}$. Most of the hydrogen envelope was thus structurally like a BSG. This was why the light curve in Figure 18 declined rapidly on the plateau after shock breakout. In other models with mass loss “1” in Table 2, the low-density convective shell was also a small fraction of the mass of the hydrogen envelope. Those with lower mass loss rates had more extended convective shells, but rarely more than one-half the envelope was involved. The time spent as an RSG by those high mass loss models was also quite short. Most reached helium core depletion ($X(^4\text{He}) = 0.01$) while still “yellow” supergiants ($T_{\text{eff}} = 5500\text{--}7000 \text{ K}$). This was particularly true for the models over $90 M_{\odot}$. The final expansion to the red sometimes took as little as 10,000 yr.

Still, observations hint that luminous blue stars, LBVs in particular, may be the immediate precursors of some unusual SNe IIn (Gal-Yam & Leonard 2009; Mauerhan et al. 2013; Smith et al. 2007; Taddia et al. 2013). Because of the smaller initial radius, the early light curves of these stars would be distinctively different. To explore this possibility, a set of blue models, the “B series” (Table 4), was artificially constructed from a subset of the T series. The stars chosen had main-sequence masses of $80\text{--}120 M_{\odot}$. It was assumed that mass loss, perhaps episodic by processes not considered here, had removed most of the envelope and left behind a helium-rich composition. All of the matter outside the desired fiducial envelope was removed from an RSG with greater mass at the time of helium depletion ($X_{\text{cen}}(^4\text{He}) = 0.01$). Reinflation was inhibited by applying a surface boundary pressure of $10^6\text{--}10^7 \text{ dyne cm}^{-2}$. Most of the resulting models had, by design, hydrogen envelopes of approximately $10 M_{\odot}$. In two cases,

B110 and B115, the effect of varying the envelope mass to $\sim 5 M_{\odot}$ or $\sim 20 M_{\odot}$ was examined. Prescribing the envelope mass precisely proved difficult because of a small amount of dredge-up that occurred after helium depletion. The resulting star was allowed to relax, both hydrodynamically and thermally, to its new structure. Well before the new star ignited carbon burning, the energy generated by helium core and hydrogen shell burning was once again in a steady state with the surface luminosity, and the star was in tight hydrostatic equilibrium. Typical photospheric radii at carbon ignition were $(2\text{--}7) \times 10^{12} \text{ cm}$ and luminosities were $6 \times 10^{39} \text{ erg s}^{-1}$ to $1.1 \times 10^{40} \text{ erg s}^{-1}$; see Table 4. Effective temperatures were thus 25,000–35,000 K. These properties overlap with common definitions for both BSGs and LBVs. The composition in the envelope was helium enriched with only about 20%–30% of hydrogen remaining by mass fraction.

The stars so generated were then allowed to evolve through their PPI and core collapse, as before, and their light curves were calculated. Significant differences were noted. Not only was the initial light curve fainter because of the small initial radius, but pulsational mass loss was weaker in the lighter stars because less envelope mass was situated at a large radius where the binding energy was low. Below about $80 M_{\odot}$, no matter was ejected. Even at $80 M_{\odot}$, only a small fraction of the outer envelope, $1.4 M_{\odot}$ out of $10 M_{\odot}$, was ejected in a weak explosion with a faint light curve (Figure 20). Typical speeds were around 500 km s^{-1} . After shock breakout, the temperature declined to near 6500 K, where it remained on the plateau. Thus an observer would see an unusually faint SN IIn.

By $90 M_{\odot}$, the situation had changed appreciably (Figure 20). The first few pulses ejected most of the hydrogen envelope with a kinetic energy near 10^{50} erg , producing a brief, faint outburst. After the ejected envelope expanded to $5 \times 10^{13} \text{ cm}$ (2 days), subsequent pulses launched strong shocks into a more extended stellar structure. The new shocks took about a day to traverse the expanded star before breaking out and initiating a much brighter transient that lasted about 80 days. Typical velocities on the plateau were $1500\text{--}2500 \text{ km s}^{-1}$, and the temperature was again near 7000 K. Keeping in mind that the LBV may have had considerable low-velocity mass loss just prior to the supernova that could contribute to both the spectrum and a “tail” on the light curve, this explosion might resemble a “normal” Type IIn, but with some “precursor activity” lasting a few days. Except for this faint precursor,

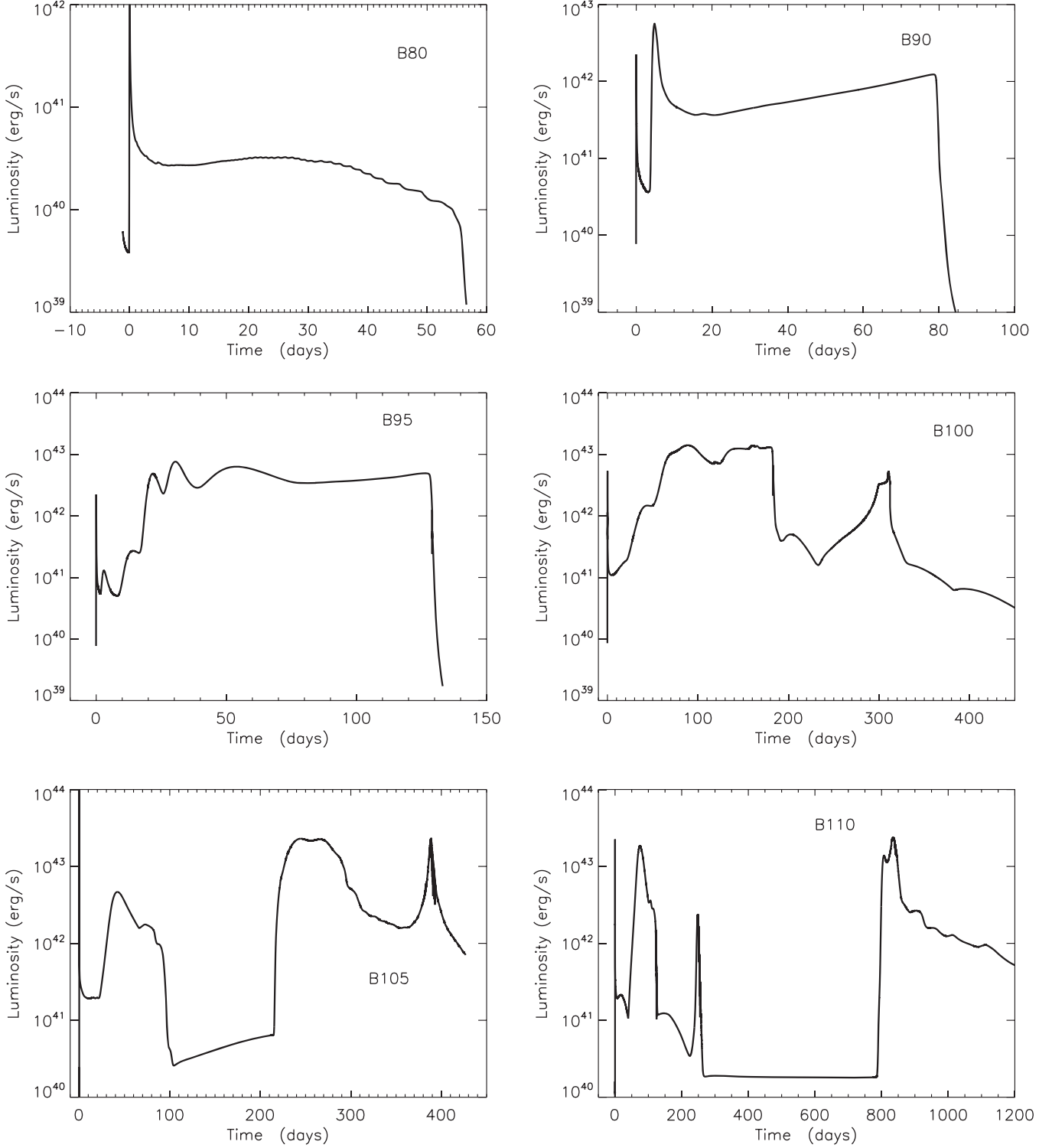


Figure 20. Light curves for blue progenitor stars with presupernova radii $(2\text{--}5) \times 10^{12}$ cm. Zero time here corresponds to shock breakout following the first pulse. On this scale, iron core collapse occurs at a time given by “duration” in Table 4. Any temporal structure after envelope recombination would be smoother in nature than in this 1D simulation. Any interaction with a presupernova wind is omitted. Luminosities in the low-luminosity dormant phases of Models B105 and B110 are partly due to fallback and are poorly determined. During these inactive periods, a constant of 10^{40} erg s $^{-1}$ might be more appropriate.

Model B90 is similar to Model T90 (Figure 15), for an appropriately small envelope mass ($\sim 10 M_\odot$).

The same trend continued for the 95 and 100 M_\odot models. The initial transient was faint because of the small presupernova radius, but after a month or so of expansion, the light curves were similar, for example, for B100 (Figure 20) and

T100 (Figure 16). Typical velocities were 2000–4000 km s $^{-1}$. The spike in emission in Model B100 at ~ 300 days was not the result of a new pulse. In fact, the iron core already collapsed in this model at day 130. The spike was instead due to matter ejected by the last pulse colliding with a dense, thin shell at 5×10^{15} cm that came from the snowplowing of earlier pulses

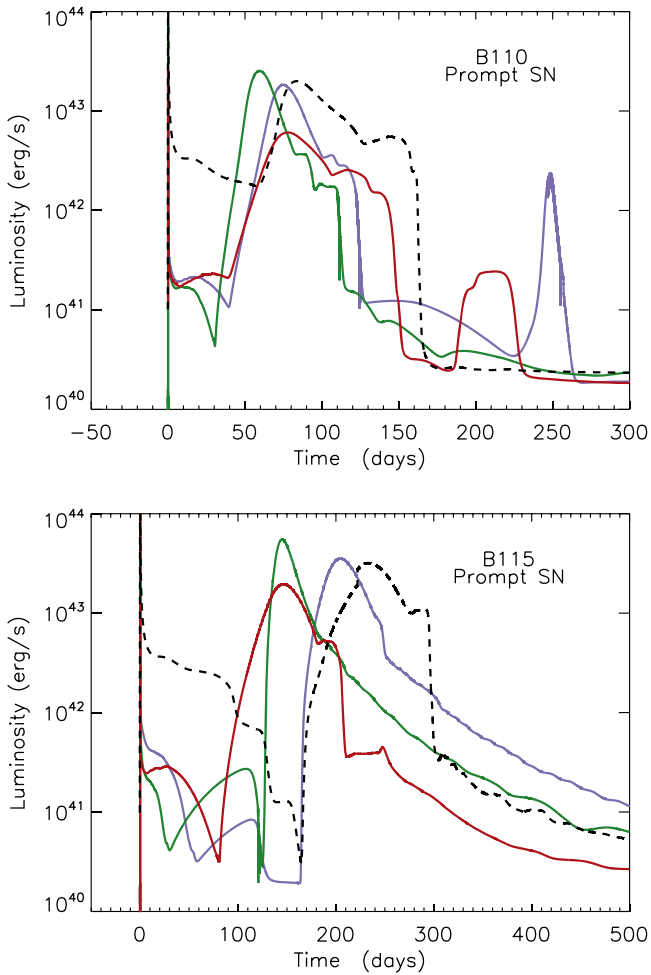


Figure 21. Bolometric light curves for the first 500 days for the explosions of two hot, blue massive stars with zero-age main-sequence masses of $110 M_{\odot}$ (top) and $115 M_{\odot}$ (bottom). The three solid curves show results for the same helium core exploding inside compact hydrogenic envelopes with masses of $5 M_{\odot}$ (green), $10 M_{\odot}$ (blue), and $20 M_{\odot}$ (red). Time is normalized to zero at shock breakout. During the first few days, the explosion emits chiefly in the ultraviolet and would be optically faint. The emission during the first faint peak is the recombination of the BSG envelope ejected in the first pulse. All subsequent emission is collisionally powered. For comparison, the light curves of RSG models T110 and T115A are shown as dashed lines. These are about 20 times brighter than during the early “plateau” stage, but similar afterward. Rapid time variations in all light curves are artifacts of the 1D nature of the calculation, and all curves would be much smoother in reality.

into the original envelope after it was ejected. This shell would have been broadened by mixing in a more realistic 2D or 3D study and not so prominent. A similar caveat applies to the spike at day 390 for Model B105.

The early light curves of the $110 M_{\odot}$ and $115 M_{\odot}$ models are particularly interesting (Figure 21). For this mass range, the interval between the first strong pulse that ejects most of the hydrogen envelope and subsequent pulses that slam into it is of order months, that is, the duration of a typical SN IIP. The light curve thus exhibits a characteristic “double peak” structure. Given the large bolometric correction near shock breakout, the first optical peak would be a faint plateau resulting from the expansion and recombination of the BSG envelope. During this time, the supernova, though less energetic, would resemble SN 1987A before radioactivity became important. The second and subsequent pulses result in a dramatic brightening due to

collision with the previously ejected envelope, which now has a large radius. For the models examined, this brightening amounted to a factor of about 30–100. The duration of the first peak was shorter for smaller hydrogen envelope masses and lower mass helium cores. Velocities in the ejected envelope were 500 – 2000 km s^{-1} for the higher mass envelopes, but extended beyond 4000 km s^{-1} for the lower mass ones.

RSG T models with the same-mass helium cores (the dashed lines in Figure 21) showed a similar but less dramatic brightening. The hydrogen envelopes for Models T110 ($13 M_{\odot}$) and T115A ($20 M_{\odot}$) had masses similar to the B models, and the core structures were identical. The different light curves thus reflected chiefly the different radii for the presupernova stars and, to a lesser extent, the different binding energies of those envelopes.

These light curves, with an initial faint “plateau” dramatically brightening on a timescale of weeks, resemble what has been reported for a number of SNe IIn. SN 1961v (Kochanek et al. 2011; Smith et al. 2011), an enigmatic event, which may have resulted from the explosion of a low-metallicity star over $80 M_{\odot}$, showed a similar light curve morphology and peak brightness. So did the 2012 outburst of SN 2009ip (Fraser et al. 2015). So did SN 2010mc (Ofek et al. 2013). At least two of these events are thought to have come from LBV stars.

Interestingly, though, and perhaps difficult to hide, the surviving stars in the B110 and B115 models all experienced a second major outburst 1.2–14 yr after the initial display shown in Figure 21. The lighter models had shorter delay times. Some of these secondary explosions in Figure 22 also show a characteristic “double hump” structure with a substantial brightening after several weeks. It might be easier to miss a previous supernova than a subsequent one.

Three factors might act to mitigate the high predicted luminosities of these second events. First, the collisions with the longest delay times happened in a medium that was becoming thin to electron scattering. Perhaps a significant fraction of the radiation would be in nonoptical wavelengths. Second, the peak brightness of the display is possibly exaggerated by the pileup of matter from previous mass ejections in a thin shell in the 1D study. Finally, the emission from interaction with any circumstellar wind emitted prior to the onset of the PPI is ignored here and might help obscure faint outbursts. Still, the total amount of energy radiated should be close to correct and is large ($5 \times 10^{49} \text{ erg}$ for the brighter B115 models, $1.3 \times 10^{50} \text{ erg}$ for the most luminous B110 model), suggesting that the location of events like these should be revisited for at least several years after the initial outburst. Chugai et al. (2004) have inferred the ejection of a massive circumstellar shell 1.5 yr before the explosion of Type IIn SN 1994W. The unshocked gas is inferred to have a velocity $\sim 1000 \text{ km s}^{-1}$ and shocked gas, $\sim 4000 \text{ km s}^{-1}$ (Kiewe et al. 2012), consistent with the models here. Similar conditions could also be created, however, by the ejection of the envelope of a $\sim 10 M_{\odot}$ star due to a silicon flash (Smith 2013; Woosley & Heger 2015b; Dessart et al. 2016).

By $120 M_{\odot}$ the rebrightening from the second pulse occurs well after the initial plateau is already over. Collectively, the blue models are similar to the red ones, but with a fainter initial display. The hydrodynamics of interacting with a compact envelope is somewhat different from interacting with an extended one through, for example, a stronger reverse shock

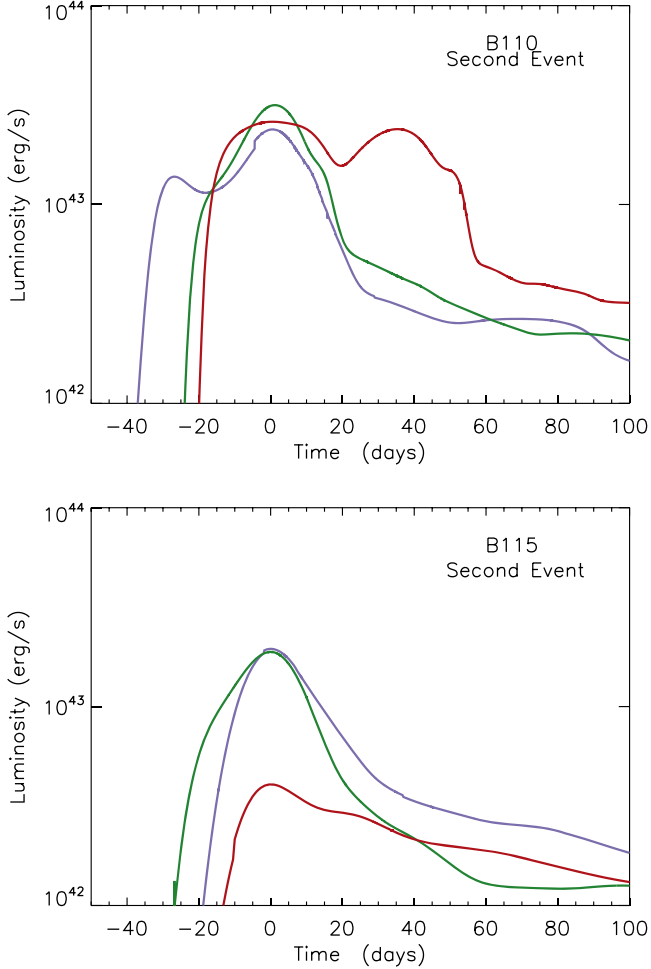


Figure 22. Bolometric light curves for the second (and final) major peaks arising from the $110 M_{\odot}$ and $115 M_{\odot}$ progenitors (see also Figure 21). The green curves are for the models with the $5 M_{\odot}$ envelope; the blue curves, for $10 M_{\odot}$; and the red curves, for $20 M_{\odot}$. Time is approximately zero at the peak. For the $110 M_{\odot}$ models, these peaks correspond to a time 2.4, 2.3, and 1.2 yr after the first supernova for models with envelopes of approximately $5, 10$, and $20 M_{\odot}$, respectively. For the $115 M_{\odot}$ models, the corresponding times are 5.7, 4.7, and 14.3 yr after the first outburst. The interaction radii vary from about 10^{15} cm to a few times 10^{16} cm, and the optical depth of the shock for the $120 M_{\odot}$ models is small, and the fraction of the emission that is in optical wavelengths is uncertain.

in the red star (Herant & Woosley 1994), and this complicates a direct comparison of the late-time evolution of models with the same mass. For example, the second explosion of Model B120 makes a light curve very much like Model T120 in Figure 18, but the interval between the first and second event is 20 yr in Model B120 and 18 months in T120.

7. Stars with Rotation

Rotation induces chemical mixing that increases the helium core mass for a given main-sequence mass, reducing the threshold for the PPI (Chatzopoulos & Wheeler 2012). If sufficiently rapid, rotation can also dramatically affect the outcome of iron core collapse, perhaps driving a final explosion. In order to examine the effects of rotation, a smaller grid of rotating stars was calculated. The nuclear and stellar physics was the same, save for the addition of rotational mixing and the transport of angular momentum as a tracer quantity. A centrifugal term was not included in the force equation, but the

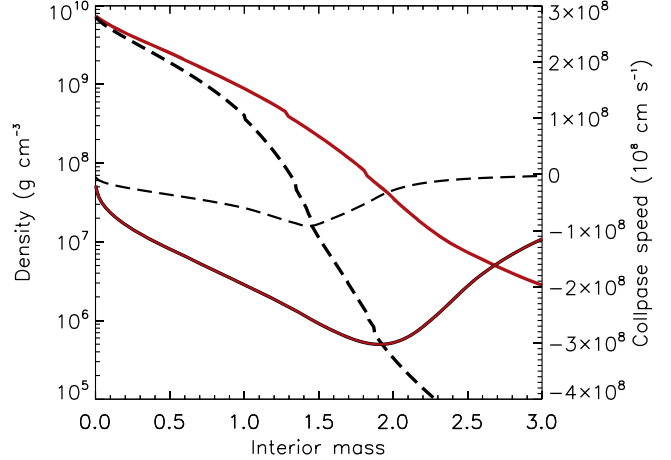


Figure 23. Density and velocity at the time of final collapse for Model T115A (solid red lines) and a typical $15 M_{\odot}$ presupernova star (dashed black lines; Woosley & Heger 2007). Both are evaluated at a central density of $7.5 \times 10^9 g cm^{-3}$ at which time the maximum collapse speed is $1000 km s^{-1}$ for the $15 M_{\odot}$ model but $3 \times 10^8 cm s^{-1}$ for Model T115A. The iron core masses at this time are $1.48 M_{\odot}$ and $2.46 M_{\odot}$ for the 15 and $115 M_{\odot}$ models, respectively, but more important is the lack of any appreciable density decline at the edge of the iron core in the $115 M_{\odot}$ model. The radius enclosing $2.5 M_{\odot}$ is $1.4 \times 10^9 cm$ for the $15 M_{\odot}$ model and $2.8 \times 10^8 cm$ for the $115 M_{\odot}$ model, implying a compactness parameter of 0.89 (O'Connor & Ott 2011) for the latter. The core of Model T115A, which is typical of the stars in this study, will be very difficult to explode using neutrinos alone. The net binding energy external to the iron core in Model T115A is $4.1 \times 10^{51} erg$.

ratio of centrifugal force to gravity was small at all times. The same metallicity (10% solar) was employed, and magnetic torques were included in all models (Heger et al. 2005).

Two sets of models were calculated to illustrate the effect of rotation in “ordinary” slowly rotating stars (the “R series”) that make red giants, and in more rapidly rotating stars that experience CHE (the “C series”) and remain compact throughout their evolution. For stars of $60, 70, 80, 90, 100$, and $110 M_{\odot}$, the R series had initial angular momenta on the main sequence of $1.1, 1.6, 2.0, 2.5, 3.0$, and $3.4 \times 10^{53} erg s$, respectively. One model, R80Ar, rotated a bit faster, $J_{init} = 2.2 \times 10^{53}$, and bordered on CHE. The surface rotational speeds on the main sequence, when the central hydrogen mass fraction had declined to 0.4, are given in Table 5 and cluster around $180 km s^{-1}$. Increasing these speeds by about 50% led to CHE. The C-series models had initial masses of $50, 60, 70, 80$, and $90 M_{\odot}$ and angular momenta of $1.5, 1.9, 2.3, 2.7$, and $3.2 \times 10^{53} erg s$, respectively. The rotational mixing parameters employed were those of Heger et al. (2000), that is, $f_c = 0.0333$ and $f_{\mu} = 0.05$. If the more recent calibration of Brott et al. (2011) is employed, $f_c = 0.0228$ and $f_{\mu} = 0.1$, which implies more inhibition to mixing. Qualitatively similar results are then obtained for the CHE models for an equatorial speed about 20% larger than in Table 5, that is, $300-320 km s^{-1}$.

For the CHE models, all hydrogen was burned or lost before any pulsations began, and a different mass loss prescription was required. For surface mass fractions of hydrogen in excess of 0.4, the mass loss rate of Nieuwenhuijzen & de Jager (1990) continued to be used (Section 2.2), appropriately scaled for metallicity. The mass lost during this stage was relatively unimportant, however. For surface hydrogen mass fractions less than 0.4, the treatment was the same as that by Woosley & Heger (2006), including a metallicity scaling of $Z^{0.66}$. The mass

Table 5
10% Z_{\odot} Models with Rotation

Model (M_{\odot})	\dot{M} (mult.)	v_{rot} (km s $^{-1}$)	M_{presN} (M_{\odot})	M_{He} (M_{\odot})	M_{Si} (M_{\odot})	M_{Fe} (M_{\odot})	J_{He} (10^{50} erg s)	J_{rem} (10^{50} erg s)	J_{Fe} (10^{48} erg s)	Duration (10^7 s)	M_{rem} (M_{\odot})	Kin. Energy (10^{50} erg)
R60A	0.5	160	46.58	30.85	8.18	2.64	6.7	29	5.2	0.0047	46.6	...
R70A	0.5	175	54.41	41.68	6.35	2.92	11	8.8	6.4	0.52	37.0	8.6
R80A	0.5	175	62.20	47.78	4.06	2.00	15	12	3.3	26	43.6	8.6
R80Ar	0.5	195	62.47	55.96	4.89	2.74	24	14	7.2	7600	47.8	22
R90A	0.5	180	68.84	56.04	5.21	1.83	21	13	3.0	7400	48.1	24
R100A	0.5	185	75.32	62.37	4.67	2.40	28	8.1	5.4	17000	44.8	38
R110A	0.5	180	80.91	65.68	26	0	62
C60A	0.5	260	26.30	...	5.54	2.09	...	6.5	3.9	...	26.3	...
C60B	0.25	270	35.40	...	8.30	2.49	...	37	15	0.0047	35.3	0.0086
C60C	0.1	275	46.45	...	7.42	2.35	...	105	37	0.76	41.2	4.9
C70A	0.5	250	28.35	...	6.21	2.22	...	6.6	3.9	...	28.4	...
C70B	0.25	260	40.72	...	8.80	2.88	...	24	14	0.061	38.1	1.7
C70C	0.1	260	53.24	...	6.02	2.31	...	16	7.5	8900	41.7	8.8
C80A	0.5	240	30.46	...	7.00	2.35	...	6.9	4.1	...	30.5	...
C80B	0.25	250	44.88	...	7.35	2.67	...	21	11	0.39	40.4	4.0
C80C	0.1	250	59.69	...	5.53	2.27	...	17	4.6	12900	46.3	14
C90A	0.5	235	31.43	...	7.27	2.39	...	7.1	4.1	0.0013	31.4	0.0072
C90B	0.25	245	49.39	...	4.12	2.60	...	17.5	8.1	41	43.4	4.0
C90C	0.1	250	65.81	0	76

loss rate was

$$\log_{10} \dot{M} = -12.43 + 1.5 \log_{10} \left(\frac{L}{10^6 L_{\odot}} \right) - 2.85 X_H + 0.66 \log_{10} \left(\frac{Z}{Z_{\odot}} \right). \quad (4)$$

This implies a loss rate at $10^6 L_{\odot}$, $X_H = 0.15$, and solar metallicity of $1.4 \times 10^{-4} M_{\odot} \text{ yr}^{-1}$. This is large compared with modern estimates (see, e.g., Figure 1 of Yoon & Langer 2005), so this rate was multiplied by factors of 0.5 (Models CxxB), 0.25 (Models CxxC), and 0.1 (Models CxxD), with 0.5 and 0.25 perhaps being most appropriate, but 0.1 within the realm of possibility.

Table 5 gives the major results and shows a strong dependence of the supernova progenitor mass of the CHE models on the uncertain mass loss rate. No helium core mass is given since the presupernova mass was less than the maximum helium core mass. All C-series stars ended their lives as Wolf-Rayet stars with surfaces containing mostly carbon and oxygen with some helium, but devoid of hydrogen. Their explosions would produce supernovae of Type I. Typical presupernova radii were $\sim 50 R_{\odot}$, and effective temperatures were $\sim 10^5$ K. In contrast, the R-series models ended their lives as RSGs with similar luminosities (within a factor of 2 of $10^{40} \text{ erg s}^{-1}$), but with extended atmospheres that still contained appreciable hydrogen and had radii near $1.5 \times 10^{14} \text{ cm}$.

Also given in the table are J_{He} , J_{rem} , and J_{Fe} , the angular momentum of the helium core at carbon depletion, the angular momentum of the final star after any pulsational activity is over (and hence the angular momentum of the black hole formed if no matter is ejected), and the angular momentum of the iron core at the time it collapses. Some possible implications for the explosion and for black hole properties are discussed in Sections 8 and 10.

Even a moderate amount of rotation substantially decreases the initial masses necessary to form helium and CO cores of a given mass (Chatzopoulos & Wheeler 2012), thus lowering the

threshold for encountering the PPI. Model R90A shows that a $56 M_{\odot}$ helium core is now made in a star with a main-sequence mass of only $90 M_{\odot}$, whereas without rotation it took $120 M_{\odot}$ (Table 2). For CHE models, the threshold for making PPISN is, in principle, even lower. Once the PPI is encountered, the cores of these rotating stars evolve similarly to their nonrotating counterparts with the same CO mass. Because of rotationally induced mixing, the helium and nitrogen abundances in the winds and presupernova atmosphere of these stars are increased. For example, the helium mass fraction in the envelope of R100A is 90%.

The Kerr parameters of the black holes formed from the collapse of the remaining cores can be calculated from the quantities in Table 5 using $a = J_{\text{rem}} c / GM_{\text{rem}}^2$ and are typically of order 0.01–0.1, though larger values are possible for the CHE models with small mass loss. If no further mass ejection occurred during the collapse, Model C60D would leave a $41 M_{\odot}$ black hole with $a = 0.7$. These large values of the Kerr parameter might be an observable signature of CHE.

8. Superluminous Supernovae

While some of the models in Section 4 were unusually bright (Figures 18 and 19), none of them emitted as much light as the brightest SLSN—events like SN 2003ma (Rest et al. 2011), SN 2006gy Smi10, SN 2005ap (Quimby et al. 2011), and SN 2008es (Miller et al. 2009). If stars in this mass range are to explain such events, it seems likely that something beyond purely thermonuclear explosions—PISN and PPISN—is necessary. The natural time for any additional energy input is when the iron core collapses, or shortly thereafter, but the large iron core masses and binding energies outside those cores, $\sim 5 \times 10^{51}$ erg, preclude neutrinos acting alone from powering an explosion (Figure 23; Wilson et al. 1986; Fryer 1999; Fryer & Kalogera 2001; Ugliano et al. 2012; Pejcha & Thompson 2015). This leaves rotation as the likely alternative.

The rotation could be so extreme as to form a disk around the black hole, a collapsar (Woosley 1993), though none of the models in Table 5 rotated that fast, or a “millisecond magnetar”

(Usov 1992; Metzger et al. 2011). In either case, conditions different from those required to make a GRB might produce a more isotropic but still very energetic supernova. In the case where a neutron star remained, the magnetar could power a prompt explosion with an energy as great as 2×10^{52} erg (Mazzali et al. 2014) and might even contribute later to the light curve itself (Kasen & Bildsten 2010; Woosley 2010; Chatzopoulos et al. 2016; Sukhbold & Woosley 2016). But would the magnetar survive the explosion? Munoz et al. (2006) reported the discovery of an X-ray pulsar with magnetar-like properties in a region where only stars with main-sequence masses greater than about $40 M_{\odot}$ had died. If one includes the mass loss appropriate to solar metallicity stars, however, the mass at death of such initially massive stars was probably substantially less than $12 M_{\odot}$ (Ekström et al. 2012). This is far lighter than the $32 M_{\odot}$ threshold for helium cores that encounter the PPI, suggesting that the vast majority of magnetars are probably made in lighter, more abundant stars.

On the positive side, even with magnetic torques and mass loss included, the short lifetimes of the stars considered here result in considerable angular momentum remaining trapped in the presupernova core. Typical angular momenta for the iron cores inside the giant star models are $(3\text{--}7) \times 10^{48}$ erg s (Table 5), and some of the CHE models rotate even faster. For a variety of equations of state, Lattimer & Prakash (2007) suggest a moment of inertia, I , for a neutron star of $I/M^{3/2} = 35\text{--}45 \text{ km}^2 M_{\odot}^{-1/2}$, where M is the gravitational mass. For a fiducial gravitational mass of $2.0 M_{\odot}$, which may be near the maximum in nature, this implies a moment of inertia near $2 \times 10^{45} \text{ cm}^2 \text{ gm}$. This, in turn, implies an angular velocity for the cold pulsar of $1500\text{--}3500 \text{ rad s}^{-1}$, or a period of 2 to 4 ms and a rotational energy of $(2\text{--}12) \times 10^{51}$ erg. Still more energy is available from some of the CHE models. Models C60C and C60D would produce submillisecond pulsars (magnetars?), so substantial deformation and gravitational radiation would be expected in their collapse.

This energy could be difficult to extract, however, since the final rotational energy of the neutron star is only available once its binding energy has been radiated as neutrinos. This takes of order of seconds, which, given the expected high accretion rate from the dense silicon shell, may not be available before an event horizon forms. The black hole masses inferred from the recent detection of gravitational radiation in the event GW 150914 also suggest that black hole formation from these sorts of stars is a common event (Section 10).

An intermediate possibility is that the star only partly explodes, with strong bipolar outflows accompanied by appreciable fallback and accretion in the equatorial plane. The final product would still be a black hole, but its birth need not be quiet. Evolution as a protoneutron star always precedes the formation of an event horizon for stars that develop iron cores in hydrostatic equilibrium. Multidimensional studies of MHD core collapse (LeBlanc & Wilson 1970; Meier et al. 1976; Müller & Hillebrandt 1979; Akiyama et al. 2003; Ardeljan et al. 2005; Burrows et al. 2007; Dessart et al. 2008; Takiwaki & Kotake 2011; Mösta et al. 2014, 2015) universally show jets or strong bipolar outflows developing during the protoneutron star stage. So far, these studies have been for lighter, less tightly bound stars and are not directly applicable here. They suggest, however, that, even if most of the helium and heavy element core does collapse to a black hole, a mildly collimated polar outflow might emerge. This outflow could

have dramatic consequences when interacting with the shells previously ejected by the PPI. The objects considered would be intermediary between those that make the powerful, tightly focused, relativistic jets seen in long, soft GRBs from massive stars and the roughly spherical explosions of ordinary supernovae.

To illustrate the possible consequences, consider Model T110C. When its iron core collapses, its mass is $2.59 M_{\odot}$, external to which the net binding energy is 4.6×10^{51} erg. A bipolar outflow focused into a solid angle of π steradians ($\pi/2$ in each hemisphere) would only need an energy slightly greater than 10^{51} erg to eject or to push aside the matter in its path. A more energetic explosion at larger angles would require more rapid rotation than calculated for the giant star models in Table 5 but is not ruled out.

Using a piston, an explosion was launched at the edge of the iron core of T110C with sufficient energy to provide the still-bound material with a final kinetic energy of 2.2×10^{51} erg at infinity. Since the star's binding energy must also be provided, this amounts to the central engine doing about 7×10^{51} erg of work, more than the total rotational energy of even a 2 ms cold neutron star. Even with this large assumed energy input, about half of the core eventually reimploded, leaving a black hole mass of about $22 M_{\odot}$. For an asymmetric explosion, fallback and accretion would probably be greater and the remnant mass larger.

The matter that was ejected interacted with the existing circumstellar shells, producing a very luminous supernova that lasted hundreds of days (Figure 24). The initial rise to peak was given by the interaction with the more recently ejected shell of helium, but a long "tail" resulted from interaction with the previously ejected hydrogen envelope with a structure imposed by different shells. The abundance of hydrogen in this envelope was low, ranging from 5% by mass at its base to 20% farther out. Most of the rest was helium and nitrogen. As the light curve developed, the effective temperature declined from 7000 K near the peak to 4000 K out on the tail.

Figure 24 also shows the results of using a parametric representation of the shell structure, which allows more control of the shell masses, densities, speeds, and radii. Varying the hydrogen envelope mass in this model affects the light curve duration, but not so much the rise to peak. The slope during the decay phase and the abrupt termination of light when the shock reaches the edge of the ejected envelope are sensitive to the assumed density structure, which was assumed to be constant.

Pulling out all the stops, the results of forcing a much more energetic isotropic explosion of $\sim 2 \times 10^{52}$ erg in three models are shown in Figure 25. These models were selected on the basis of having experienced a major mass ejection roughly a year prior to iron core collapse. A longer wait and the ejected matter would have moved to such a large radius (well beyond 10^{16} cm) that the interaction would be too faint, though longer lasting, and perhaps not an optical supernova. A shorter wait, and the ejected matter would still have been very optically thick and the energy from the collision subject to adiabatic degradation. Model He50 ejected a total of $6.3 M_{\odot}$ during six pulses spanning the last 0.35 yr before its iron core collapsed (Figure 3); Model R80Ar ejected $8.2 M_{\odot}$ 1.0 yr earlier; and Model T105C ejected $47.7 M_{\odot}$ 1.4 yr earlier. The kinetic energies of these ejected shells were 0.86, 0.55, and 0.70×10^{51} erg, respectively. Typical shell velocities were 3500, 2500, and 1200 km s^{-1} for Models He50, R80Ar, and

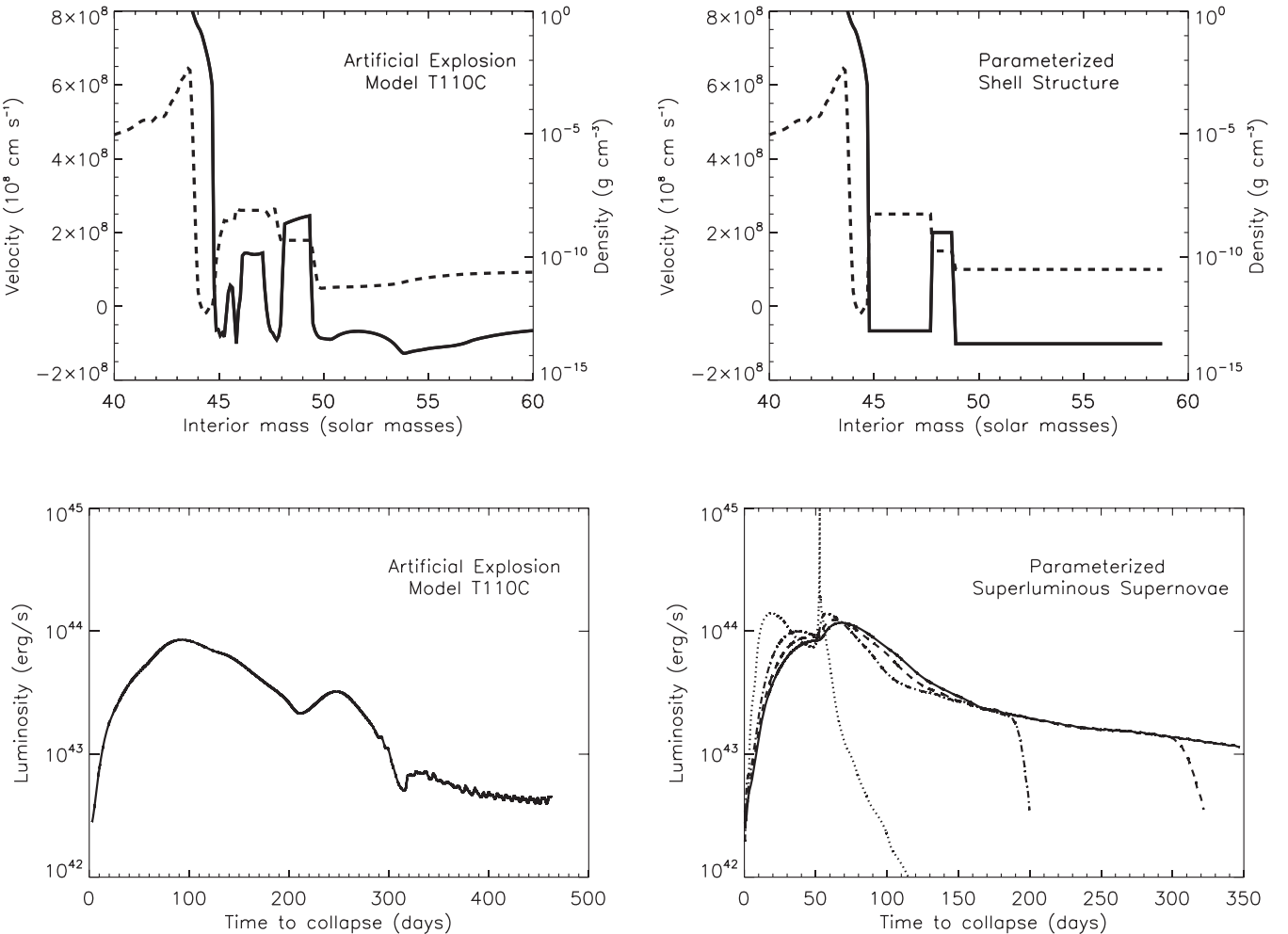


Figure 24. Artificial explosions in Model T110C. Top left: density (solid line) and velocity (dashed line) of Model T110C at the time the shock wave from an artificially induced explosion arrives at the edge of the bound remnant at $44.7 M_\odot$, 100 s after core collapse. Outside the core are several shells of matter ejected by previous pulses. The boundary of the large density spike at $49 M_\odot$ is at $2.07 \times 10^{15} \text{ cm}$. The ejected matter actually extends to $96 M_\odot$, though only the inner $60 M_\odot$ is shown. Bottom left: bolometric light curve resulting from the evolution of the velocity and density structure shown in the top left panel. At the end of the curve shown, the external shock had reached $76.7 M_\odot$ and $1.1 \times 10^{16} \text{ cm}$ and had a speed of 1900 km s^{-1} . Top right: parameterized density and velocity profiles are adopted outside the core, including one major shell at $47.7 - 48.7 M_\odot$, radius $2.4 \times 10^{15} \text{ cm}$, and speed 1500 km s^{-1} . The profile qualitatively resembles that for Model T110C shown on the left, but with only one major shell. The densities, speeds, and masses are now user-adjustable parameters. Bottom right: the bolometric light curve resulting from the configuration shown in the upper right panel. Several light curves were calculated in which the mass of the ejected envelope exterior to $48.7 M_\odot$ was 0, 10, 20, and $30 M_\odot$. The results are shown as the dotted, dash-dotted, dashed, and solid lines, respectively. The dip at about 50 days is artificial and reflects the arrival of the main shock at the inner edge of the dense shell at $47.7 M_\odot$. The energy emitted in light for the four models is 0.54, 0.92, 1.09, and $1.12 \times 10^{51} \text{ erg}$.

T105C, respectively. For R80Ar, this final shell ejection came after losing its hydrogen envelope to pulses 2400 yr earlier. Models He50 and R80Ar would thus be of Type I, while T105C would be Type II. Because these are a small subset of all PPISN, which itself is already a rare class (Section 12), they would be exceedingly infrequent events, less than 1% of core collapses, even in metal-poor regions.

Explosions in these three stars were simulated by removing the iron core and placing a piston at the inner boundary that imparted a large explosion energy to the external matter. For He50, the kinetic energy before radiative losses was $2.1 \times 10^{52} \text{ erg}$. Since the binding of the matter external to the core was $4.6 \times 10^{51} \text{ erg}$, this implies a total energy delivered by the central engine of about $2.6 \times 10^{52} \text{ erg}$, close to the upper bound on rotational energies for pulsars. For Models R80Ar and T105C, the kinetic energies, before radiative losses, were 1.4×10^{52} (plus $4.7 \times 10^{51} \text{ erg}$ for the binding energy) and 2.0×10^{52} (plus $4.6 \times 10^{51} \text{ erg}$ for the binding energy). No matter fell back. A large amount of ^{56}Ni

was synthesized, $2.7 M_\odot$, $1.8 M_\odot$, and $2.5 M_\odot$, respectively, for He50, R80Ar, and T105C, but this had little effect on the light curve. Typical expansion speeds for the interacting matter behind the shock were $10,000 \text{ km s}^{-1}$, declining with time due to shock interaction to about 4000 km s^{-1} .

The resulting light curves approached $10^{45} \text{ erg s}^{-1}$ at maximum in all three cases, but the duration and hence the total emitted power were very sensitive to the speed, mass, and radius of the shell that was being impacted (Figure 25). Integrated luminous powers were 1.2, 2.5, and $6.6 \times 10^{51} \text{ erg}$. The latter, from Model T105C, is probably close to the maximum that can be attained in any PPI plus magnetar-powered explosion since the mass of the shell was approximately equal to the mass of the exploding core and the shell speed was low.

When two masses m_1 and m_2 with speeds v_1 and v_2 experience an inelastic collision and radiate all dissipated energy, conservation of momentum and energy implies that the fraction of the initial kinetic energy radiated is $f(1+f)^{-1}(1-g)^2$,

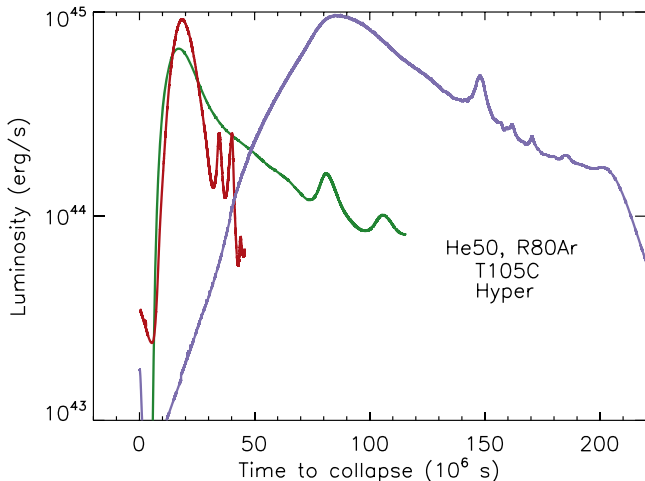


Figure 25. Results of artificial “hyperenergetic” explosions, at the time of iron core collapse, of Models He50 (red), R80Ar (green), and T105C (blue). The three models emitted 1.2×10^{51} erg (He50), 2.1×10^{51} erg (R80Ar), and 6.6×10^{51} erg (T105C) of light. Time is measured in days since the simulated explosion. The postpeak variability is artificially exaggerated in this 1D calculation.

where f is the ratio of the two masses, $f = m_2/m_1$, and g is the ratio of the initial speeds, $g = v_2/v_1$. Here m_1 is the part of the core mass that collides with the shell of mass m_2 during the time the light curve is mostly generated. The most efficient production of light then occurs when $f < 1$, that is, the shell is more massive than that part of the core with which it interacts, and $g = 0$, that is, the shell is initially stationary. For models with envelopes comparable to the core mass (it can hardly be much bigger), $f \approx 1$ and g is at best $1/10$, so no more than 40% of the kinetic energy is radiated. For models without envelopes, the efficiency is smaller. For typical shell masses of, at most, $5\text{--}10 M_\odot$, a core mass of $40 M_\odot$, and shell speed one-third of the edge of the exploding core, the maximum efficiency is closer to 10%. These estimates of upper bounds, 2×10^{51} for Type I and 8×10^{51} , agree reasonably well with the results for Models He50, R80Ar, and T105C. They are also consistent with observations of the brightest SLSN, for example, SN 2003ma, SN 2006gy, SN 2005ap, and SN 2008es.

Still more luminous supernovae are possible, in principle, if a magnetar contributes directly to the light curve (Kasen & Bildsten 2010; Woosley 2010; Chatzopoulos et al. 2016; Sukhbold & Woosley 2016). While it seems increasingly likely that many SLSN are indeed illuminated by magnetars (Inserra et al. 2013, and references therein), that possibility is not explored here because of the additional complexity and uncertain parameters required for a model that provides both a prompt hyperenergetic explosion ($\sim 10^{52}$ erg) and a large amount of electromagnetic energy at late times.

9. Eta Carinae

One of the most enigmatic of astronomical icons, Eta Carinae is also one of the most massive stars in our galaxy (Davidson & Humphreys 1997). Depending upon its mass loss history, Eta Carinae seems likely to encounter, or to have encountered, the PPI at the end of its life. Indeed, the generally accepted mass, $\sim 120 M_\odot$ (Hillier et al. 2001), places it squarely in the range treated in this paper. But at what stage in its life are we viewing the star? Will mass loss ultimately remove the

Table 6
125 M_\odot Models for Eta Carinae

Model	M_{ej1}	E_1	t_{1-2}	M_{ej2}	E_2	t_{PreSN}	M_{now}
T125A	22.5	8.3	70	7.1	8.0	2650	51.8
T125B	34.0	9.6	470	7.4	5.8	1100	58.2

hydrogen envelope and shrink the core so much that the PPI is avoided?

Eta Carinae’s last millennium has been complicated. There is evidence for unusual mass ejections starting at least 700 yr ago (Walborn et al. 1978; Davidson & Humphreys 1997; Kiminki et al. 2016). Beginning around 1837, the star underwent a major structural change known as the “Great Eruption” that lasted roughly 20 yr with frequent large variations in brightness during that period (Smith & Frew 2011) that are sometimes counted as separate eruptions. In 1843, the star’s apparent magnitude briefly increased to approximately -1 , making it the second brightest extrasolar object. A lesser eruption occurred in the 1890s. The current luminosity of Eta Carinae is about 1.9×10^{40} erg s $^{-1}$ (Hillier et al. 2001), which is being emitted mostly in the infrared (de Koter et al. 2005). Smith et al. (2003) estimate a mass for the material that was ejected in the major outburst, a portion of the “Homunculus,” of more than $10\text{--}15 M_\odot$. Smith et al. (2003) further estimate that this matter carries a kinetic energy of $10^{49.6}\text{--}10^{50}$ erg. Smith (2008) and Smith (2013) have made a compelling case that the production of the Great Eruption required an explosive event, not just a strong wind. The duration of the major mass ejection was less than 5 yr (Smith 2006) and the velocity and energy in the ejecta are quite asymmetric (Smith 2006), with $\sim 90\%$ of the explosion energy concentrated at latitudes above 45 degrees. Velocities as high as $3500\text{--}6000$ km s $^{-1}$ have been reported, though a more typical speed is 650 km s $^{-1}$ (Smith 2008).

These energies, masses, and a star that survives for centuries after the first explosive outburst with a luminosity of $\sim 10^{40}$ erg s $^{-1}$ are just what one might expect for a PPISN (Woosley et al. 2007; Smith 2008) with a helium core mass near $55 M_\odot$ (Table 2). This would be derived from a main-sequence star of $\sim 125 M_\odot$, if rotation is not included, and about $90 M_\odot$ if it is. Though there is no reason to assume that Eta Carinae has low metallicity, it is the helium core and envelope mass that matter most, so the T models can be a useful guide. Making Eta Carinae as described here in a solar metallicity star would require a significant reduction in currently favored mass loss rates though.

Consider the two models, T125A and T125B. Some relevant properties are given in Table 6. Here M_{ej1} and M_{ej2} are the masses in solar masses ejected in pulses 1 and 2, and E_1 and E_2 are their kinetic energies in units of 10^{50} erg. There are only two pulses: t_{1-2} is the time between the first pulse (nominally $t = 0$) and the second, and t_{PreSN} is the time between the second pulse and the collapse of the iron core. Both are measured in years. Here, M_{now} is the mass of the primary star in Eta Carinae today, which should be in the range $50\text{--}60 M_\odot$. Most of the mass ejected in the first pulse is envelope, although helium is its dominant constituent. Most of the mass ejected in the second pulse is helium and carbon. Nitrogen is overabundant in both pulses because of extensive CNO processing. Both models leave Wolf-Rayet stars in the present-day remnant. These WR stars have a luminosity near 10^{40} erg s $^{-1}$, as is observed. Both

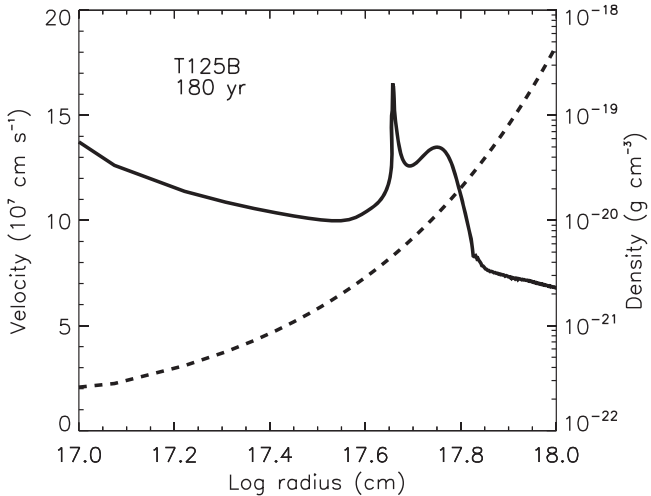


Figure 26. Density (solid line) and velocity (dashed line) 180 yr after the first pulse (i.e., at the present epoch) in the ejecta of Model T125B. Velocity is in 100 km s^{-1} , and the density ranges from 10^{-22} to $10^{-18} \text{ g cm}^{-3}$. Roughly $13 M_{\odot}$ of the $34 M_{\odot}$ ejected is currently in a thin shell between 4 and $6 \times 10^{17} \text{ cm}$. The dense concentration is a result of the reverse shock operating as the forward shock plowed through an envelope of nearly constant density during the explosion.

models explosively eject a mass comfortably above the lower limit for the observed mass of the Homunculus.

Assuming that the first pulse and the ejection of the envelope occurred around 1837, Model T125A has a second pulse that, within the generous error bars of the models, might coincide with the 1890 outburst. This model is too energetic, however. By now the ejecta of the two pulses would have merged, and most of the matter would have a speed near 2000 km s^{-1} , well above the observed average 650 km s^{-1} (Smith 2008). Model T125B fares somewhat better if only one pulse has happened so far. One-half of the ejected mass is moving slower than 1100 km s^{-1} (Figure 26). In this case, though, the pulsing is not over, and another Great Eruption is due in the next few centuries. It could of course be that the actual pulses were somewhat weaker than in Model T125A, for example, because of a lower mass helium core or larger hydrogen envelope mass. The two models do not fully explore the range of possibilities.

This hypothesis has two major difficulties though. One is the expected brightness of the first mass ejection, which, if the progenitor was an RSG, would have exceeded $4 \times 10^{42} \text{ erg s}^{-1}$ for roughly 100 days, that is, resembled an ordinary SN IIP, not an “impostor.” The other is the gross asymmetry of the observed ejecta. The latter might relate to the well-established presence of a binary companion with a current mass of $\sim 30 M_{\odot}$ (Madura et al. 2012), period 5.54 yr, semimajor axis 16.64 au, and eccentricity 0.9 (Hillier et al. 2001; Daminel et al. 2008; Parkin et al. 2011). The large eccentricity implies that at closest approach the stars are separated by only 1.5 au. Given that the radii of all the RSGs studied here, both solar and low metallicity, are over 10 au, the companion has spent a lot of the time inside the primary. Some sort of direct interaction would have been unavoidable (Smith 2011). This might be avoided or lessened if the primary were a BSG or LBV. A dramatic expansion of the solar metallicity stars frequently occurs at the end of helium burning (Section 5) when the core is contracting to ignite carbon, a process that takes about 10,000 yr. If so, a substantial fraction of the primary’s envelope might be ejected in the plane of the orbit (e.g., Nordhaus &

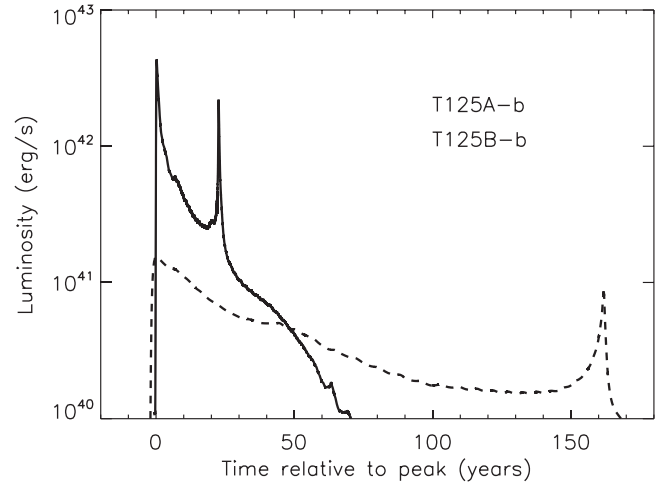


Figure 27. Bolometric light curve resulting from the collision of the second mass ejection in Models T125A (solid line) and T125B (dashed line) with the first. Relative to zero here, the first pulse happened 70 yr earlier (T125A) and 470 yr earlier (T125B). If these models were taken to represent Eta Carina, the solid line would be the expected light curve for the second eruption in the 1890s, and the dashed line would still lie two centuries in the future. The sharp spikes in luminosity are artificial and would be smoothed by mixing in a 2D simulation or by additional opacity. The second outburst in both models happens as the second pulse sweeps over the density enhancement left by the reverse shock in the first pulse (see Figure 26). The collision giving the light curves shown happens between roughly 5 and $10 \times 10^{17} \text{ cm}$, and the radiation might be emitted in wavelengths other than optical.

Blackman 2006; Morris & Podsiadlowski 2009; Smith 2011) just before the pulses begin.

A bigger problem may be how to hide the 100-day light curve from the first pulse. Someone probably would have noticed the sudden appearance of a magnitude-6 star, even in the southern hemisphere in 1830. One possibility is that the progenitor was a blue star and not an RSG (see Section 6). Another is that the Great Outburst was heavily extinguished by dust. The latter seems unlikely, however, since historical observations of Eta Carinae itself, well before the Great Eruption (Smith & Frew 2011) do not indicate a large amount of extinction.

Another possibility is that the first pulse in Model T125B and its bright supernova happened in the distant past, centuries *before* the Great Outburst (Table 6), and that the bright episode in the 1830s was the *second* pulse running into the first. The dashed line in Figure 27 is the resulting light curve. A second delayed brightening occurs about 150 yr later as the shock wave encounters a density spike left behind by the reverse shock in the first eruption. The sharpness of the spikes in the light curve in Figure 27 are an artifact of the 1D calculation and would be smoothed out in 2D. Again though, the velocity of the average ejecta 170 yr after the second pulse produced the Great Eruption (i.e., today) is about 2000 km s^{-1} , larger than what is presently seen.

The future will tell, though not right away, if either of these scenarios is correct. Eta Carinae could experience another great eruption in the next few centuries (Model T125B) or disappear in a thousand years. Eta Carinae itself is not a star in the regular sense. It is shining by gravitational contraction on its way to a final episode of core silicon burning. Eventually the primary “star” in Eta Carinae will collapse, probably to a black hole. If rotation and magnetic fields generate a strong bipolar explosion,

Table 7
Nucleosynthesis In Low-metallicity Models

Species	0.1 Z_{\odot} X	T80A (M_{\odot})	T90A (M_{\odot})	T100A (M_{\odot})	T110A (M_{\odot})	T120A (M_{\odot})	T130A (M_{\odot})	T140A (M_{\odot})	T150A (M_{\odot})
^1H	0.721	-9.2	-15.3	-17.7	-18.9	-19.2	-23.7	-62.4	-70.8
^4He	0.278	9.2	15.2	16.6	18.3	19.2	20.2	6.7	5.8
^{12}C	2.5(-4)	-3.5(-4)	2.0(-2)	1.3(-1)	9.0(-2)	5.0(-4)	2.9(-1)	1.4	1.4
^{13}C	3.0(-6)	8.2(-5)	7.4(-5)	5.6(-5)	4.9(-5)	4.6(-5)	3.6(-5)	-8.2(-5)	-1.1(-4)
^{14}N	8.1(-5)	4.1(-3)	3.3(-3)	2.1(-3)	2.3(-3)	3.2(-3)	-3.2(-4)	-4.9(-2)	-5.7(-2)
^{15}N	3.2(-7)	-1.2(-6)	-7.3(-7)	-4.8(-7)	-1.2(-7)	2.8(-7)	5.8(-7)	2.9(-4)	3.6(-4)
^{16}O	6.7(-4)	-4.3(-3)	6.0(-2)	9.1(-1)	4.7(-1)	-5.1(-3)	3.0	44.8	45.6
^{17}O	2.7(-7)	-5.0(-6)	-6.6(-6)	-6.9(-6)	-6.9(-6)	-6.8(-6)	-7.4(-6)	-1.3(-5)	-1.4(-5)
^{18}O	1.5(-6)	-2.2(-6)	6.8(-4)	7.8(-4)	8.9(-4)	9.4(-4)	1.1(-3)	1.9(-3)	2.3(-3)
^{19}F	4.7(-8)	-6.1(-8)	2.7(-7)	2.4(-7)	3.7(-7)	1.9(-7)	4.0(-7)	1.7(-5)	1.2(-5)
^{20}Ne	1.2(-4)	-7.5(-4)	-8.3(-4)	2.9(-2)	1.1(-2)	-1.7(-3)	2.2(-1)	2.2	2.3
^{21}Ne	3.0(-7)	-2.5(-6)	-2.6(-6)	8.4(-6)	2.5(-6)	-3.0(-6)	1.4(-5)	1.6(-4)	1.3(-4)
^{22}Ne	9.6(-6)	-8.5(-6)	1.1(-3)	1.3(-3)	1.4(-3)	5.2(-4)	1.3(-3)	1.3(-4)	1.2(-5)
^{23}Na	3.9(-6)	1.4(-4)	7.8(-5)	6.5(-5)	8.2(-5)	1.2(-4)	9.2(-5)	4.6(-3)	4.8(-3)
^{24}Mg	5.7(-5)	7.6(-4)	1.3(-3)	4.3(-3)	2.6(-3)	1.8(-3)	3.6(-2)	1.7	1.6
^{25}Mg	7.6(-6)	-8.9(-5)	-1.1(-5)	8.0(-4)	3.9(-4)	-2.1(-5)	3.0(-3)	2.0(-2)	2.0(-2)
^{26}Mg	8.7(-6)	-2.1(-4)	-2.8(-4)	5.9(-4)	5.2(-5)	-4.5(-4)	2.9(-3)	2.3(-2)	2.3(-2)
^{27}Al	6.7(-6)	3.2(-4)	5.0(-4)	5.8(-4)	6.4(-4)	6.7(-4)	8.0(-4)	3.9(-2)	3.5(-2)
^{28}Si	7.7(-5)	7.0(-6)	1.1(-5)	-7.0(-6)	6.0(-6)	1.8(-5)	-4.2(-5)	4.0	8.5
^{29}Si	4.0(-6)	-5.9(-7)	1.3(-6)	1.8(-5)	9.4(-6)	-4.0(-7)	6.2(-5)	2.6(-2)	2.2(-2)
^{30}Si	2.7(-6)	...	2.6(-6)	2.9(-5)	1.5(-5)	9.0(-7)	9.3(-5)	1.5(-2)	1.0(-2)
Total	1.0	41.0	54.1	60.7	65.5	69.4	78.7	135.6	150

it could become an SLSN, but at least as likely, it will not. It will become a black hole of about $50 M_{\odot}$. Given the persistence of the close binary companion, Eta Carinae would then possibly become a very luminous X-ray source.

If not Eta Carinae itself, the class of PPISN with its broad range of luminosities and durations with the possibility of recurrent supernovae probably relates to some other supernova “impostor” (e.g., Smith et al. 2011).

10. GW 150914

The detection of gravitational radiation from two merging black holes in GW 150914 (Abbott et al. 2016b) offers new insights into the evolution of stars in the mass range that might make PPISN. The inferred masses, 36^{+5}_{-4} and $29^{+4}_{-4} M_{\odot}$, are what one would expect from the evolution of low-metallicity, nonrotating stars with masses near 70 and $90 M_{\odot}$ (Table 2 in Woosley 2016). If rotation is included, the inferred main-sequence masses are closer to 60 and $70 M_{\odot}$ (Table 5). Model R60A is a special case with a residual hydrogen envelope of about $16 M_{\odot}$ that would have been lost in a close binary capable of merging in a Hubble time. The estimated black hole masses for Models R60A and R70A in a close binary are thus 30.9 and $41.7 M_{\odot}$.

Models from CHE can also, given a freely adjustable mass loss rate, produce the observed black hole masses for any progenitor mass above the masses of the black holes themselves; for example, Model C90B makes a black hole of $31.4 M_{\odot}$ (all masses might be reduced by a few tenths of M_{\odot} to account for neutrino losses during the protoneutron star stage). A possible discriminant is the rotation rate of the black hole. More mass loss means greater braking and a slower spin for the black hole. Model C90B has a Kerr parameter of 0.08; Model C60C, which makes a similar $35.3 M_{\odot}$ black hole, gives a Kerr parameter of 0.34. Given the small radii of the CHE models throughout their evolution, it might be possible that a close

binary could merge in a Hubble time without experiencing a common envelope phase (Mandel & de Mink 2016).

An important inference from GW 150914 is that stars in the mass range that makes PPISN must at least occasionally, and probably frequently, collapse to black holes. Though low-mass jet-like outflows cannot be excluded (Section 8), the cores cannot always explode completely in rotationally powered supernovae that leave neutron star remnants. The calculations presented here also have implications for the kind of black holes that might be discovered in the future. It has long been known that there should be a gap in black hole production between 64 and $133 M_{\odot}$ (Heger & Woosley 2002). The hydrogen envelope is loosely bound in stars that have helium cores in this mass range, and such stars robustly explode as PISN, leaving nothing behind. This paper extends that range downward from $64 M_{\odot}$ to $52 M_{\odot}$. No matter what the star’s mass when it encounters the PPI, it will pulse until sufficient mass is lost for the star to complete its silicon-burning evolution in hydrostatic equilibrium. The heaviest such core in Table 2 is $52 M_{\odot}$. There can be lighter black holes, but none heavier until a helium core mass of $133 M_{\odot}$ is reached. Single stars like Model T70B could, in principle, make a black hole of over $52 M_{\odot}$ if the envelope as well as the core participated in the collapse. For zero mass loss, this mass could be as large as $70 M_{\odot}$. Given how loosely bound the envelope is, getting it to collapse might prove difficult (Weinberg & Quataert 2008; Lovegrove & Woosley 2013), but this cannot be ruled out. The close binaries that make X-ray sources or merge in a Hubble time are a different issue, however. There the envelope will be lost in a common envelope or by mass exchange. There should be no black holes in close binary systems with masses between 52 and $133 M_{\odot}$. CHE models will also lack any loosely bound envelope and will not produce black holes in this mass range, even as single stars.

As with all rules, there are exceptions. Two black holes might merge in a triple system, to make a black hole of up to

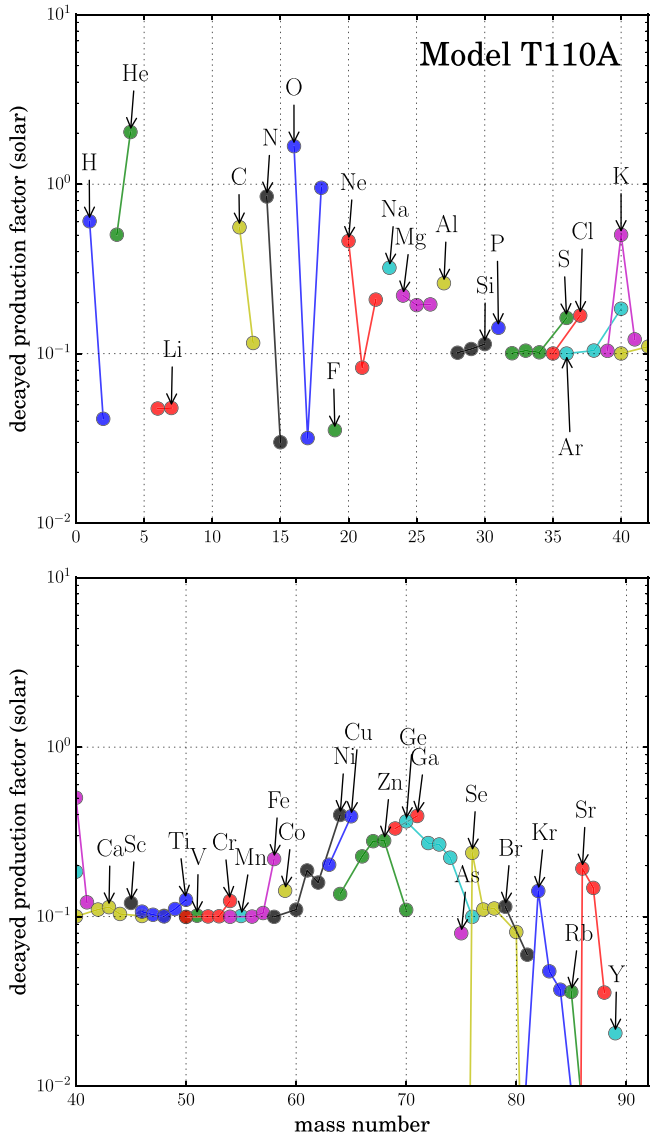


Figure 28. Nucleosynthesis in Model T110A. Production factors for the isotopes of a given element are connected by lines. A value of 1 in the ejecta would correspond to a solar mass fraction. The concentration of points around a production factor of 0.1 between $A = 28$ and 58 reflects unchanged abundances in a star that had 0.1 solar mass fractions of these species to begin with; that is, the metallicity of the initial star was 0.1 solar. Species above 0.1 thus have a net creation in the event, and those below are at least partly destroyed. Species with production 0.1, like ^{56}Fe , would have a much lower production factor in a lower metallicity star. The abundances of ^{40}K and species above $A = 58$ show the operation of a limited s-process in the helium shell prior to the PPI. ^{14}N is produced by the CNO cycle and would be smaller in a star of lower metallicity. ^{12}C and ^{16}O are mostly primary, produced by helium shell burning.

100 M_{\odot} that later merged with a third, or the black hole binary might form in a dense cluster by dynamical processes (Abbott et al. 2016a). Which is to say the discovery of a black hole of say 60 or 70 M_{\odot} would have profound implications.

11. Nucleosynthesis

Nucleosynthesis for a representative series of models is given in Table 7 and Figure 28. The models given are the “A” series of low-metallicity, nonrotating stars for which a standard mass loss prescription was used. The “Total” in columns 3

through 10 is the total mass ejected in winds and in pulses by the given model. The quantity $0.1 Z_{\odot}$ times the “total” in each column is the starting composition for that material. Column 2 is the starting composition for all of the low-metallicity, full star models, given by mass fraction. The other numbers in other columns give the changes from these initial values. While the network in all cases extended to above germanium, only the species below titanium are tabulated. There was little contribution to heavier elements, except for a mild s-process (Figure 28). Except for the last two cases, in which nearly (T140A) or all (T150A) of the star exploded, the nucleosynthesis is evaluated at the time of carbon depletion just before pulses started. In those cases, subsequent nuclear burning farther in did not affect the ejecta, and presumably all ended up in black holes. In those cases where nuclear processing after helium burning is negligible, the pulses, nucleosynthetically, merely act to augment mass loss.

The main products of PPISN are thus helium, carbon, nitrogen, and oxygen. Small amounts of fluorine through silicon are also ejected and some s-process up to mass $A = 80$. No appreciable primary iron-group synthesis occurs in any model. Even in T150A, a full-up PISN, only 0.045 M_{\odot} of iron is ejected, and most of that is ^{54}Fe , not ^{56}Ni . In the same model, 8.5 M_{\odot} of ^{28}Si and 45.6 M_{\odot} of ^{16}O are produced, so this small iron production is nearly negligible.

The nucleosynthesis of Models 120A and 140A is anomalous compared with the rest because of the large remnant mass in the former and the small remnant mass in the latter. T140A in fact closely resembles Model T150A. If the initial mass function for some reason resulted in the production of no stars above 130 M_{\odot} , then CNO would be the principal nucleosynthetic contribution of this mass range. However, just a few stars of 150 M_{\odot} and more would quickly come to dominate. Given the relatively small amount of iron made all the way up to mass 200 M_{\odot} , one would expect from a generation of such stars (truncated below 200 M_{\odot}) a composition rich in the elements carbon through magnesium with an increasing concentration of silicon through calcium at higher masses. It would be quite deficient in iron-group species.

While not presented in this paper, zero-metallicity models have also been calculated and have similar nucleosynthesis, with the notable exception of large quantities of primary nitrogen made in the very low metallicity stars.

12. Conclusions

The PPI, operating in stars with various final helium core masses, envelope masses, and radii, gives rise to a broad range of observable phenomena. These include single supernovae ranging from very faint to very bright; supernovae with complex, distinctive light curves and multiple peaks; recurrent supernovae; bright, enduring radio and X-ray sources; and supernova remnants that contain luminous WR stars. This paper has been a first attempt to characterize these diverse possibilities and describe their observable properties.

PPISN occur when mass loss does not shrink the final helium core below 30 M_{\odot} (40 M_{\odot} for the more luminous events). They are thus favored by low metallicity, and a threshold value of about one-third Z_{\odot} is estimated here (Section 2.2). Uncertain mass loss rates make this limit very approximate, however, and PPISN are not excluded even at solar metallicity. For bare helium cores above 62 M_{\odot} , the pair instability is so violent that

the entire star is disrupted in a single pulse, that is, a PISN. Slightly larger cores, up to $65 M_{\odot}$, can still be PPISN if that core is embedded in a massive hydrogen envelope (Table 2).

For the stellar physics used, this range of helium core mass is produced by single, nonrotating stars of 10% solar metallicity with main-sequence masses between 70 and $140 M_{\odot}$. This same mass range would yield PPISN for other nonrotating stars in which mass loss failed to uncover the helium core before the star died. In particular, the same limit would apply to stars with less metallicity, including Pop III stars, and to solar metallicity stars with unusually low mass loss rates (Table 3). For a moderate amount of rotation, the threshold main-sequence mass for the PPI is reduced to $60 M_{\odot}$, or even less in the case of CHE (Table 5). On the other hand, ending life as a nonrotating BSG can raise the lower bound for a faint optical display to $80 M_{\odot}$. Regardless of radius, the presupernova stars will have bolometric luminosities in the range 0.5 to $1.3 \times 10^{40} \text{ erg s}^{-1}$. These progenitors may be RSG, BSG, LBV, or WR stars, and all four possibilities were explored here.

The fraction, by number, of core-collapse supernovae (all stars above $8 M_{\odot}$) in the range $70 M_{\odot}$ to $140 M_{\odot}$ for a Salpeter IMF with $\Gamma = -1.35$ is small. Taking an upper limit on the stellar mass of, for example, $150 M_{\odot}$ (the answer is not sensitive to this limit), we get

$$f_{\text{PPISN}} = \frac{70^{\Gamma} - 140^{\Gamma}}{8^{\Gamma} - 150^{\Gamma}} = 0.033. \quad (5)$$

The fraction in the more restricted mass range, $90 M_{\odot}$ to $140 M_{\odot}$, that makes optically bright events is smaller still, about 1.7%. These estimates might be multiplied by 2 or so since a substantial fraction of core collapses below $70 M_{\odot}$ go directly to black holes with no bright display and the IMF is not precisely Salpeter-like, but the fraction of bright supernovae from PPISN is probably no more than a few percent. On top of that, PPISN probably only happen in metal-poor regions. If, as appears likely, PPISN often end up looking like SNe Ibcn and SNe IIn, they can only explain a small fraction of the observed events. SNe IIn alone are estimated to be 2%–9% of core-collapse events (Kiewe et al. 2012). PPISN might, however, account for some of the more unusual cases.

Provided a helium core in the unstable mass range survives to the presupernova stage, the PPI and its consequences are unavoidable, and its qualitative features are robust and simple to calculate (Section 3.1). For low-mass cores the PPI is weak, lasts a short time, and is characterized by many low-energy pulses that, in total, release only a small amount of energy. For more massive cores, the converse is true (Table 1, Section 3.2). Fewer pulses, separated by longer intervals, eject more mass with greater energy. The maximum duration of any PPI episode is close to the Kelvin–Helmholtz time for the typical helium core mass starting from a loosely bound state, about 10,000 yr, and the maximum explosion energy is a fraction of the binding energy of that core, $\sim 4 \times 10^{51} \text{ erg}$. Full stellar models (Tables 1, 2) demonstrate these characteristics.

Once the pulsational episode is ended, which typically requires the exhaustion of oxygen in the inner $6 M_{\odot}$ of the more massive stars, silicon burning ignites, either centrally or in a shell, and the star forms an iron core in hydrostatic equilibrium that collapses in the usual way. Unlike supernovae in lighter stars, however, the iron core is very massive, and the density outside declines slowly with radius (Figure 23). Such a star is

virtually impossible to explode with neutrinos and difficult to completely explode even with rotation. It may thus be that the pulsations and the colliding shells they produce are the sole optical and chemical manifestations of star death in the mass range that makes PPISN (though see Section 8).

Some PPISN progenitors will have lost most or all of their hydrogenic envelopes, or will have experienced CHE and will be Wolf–Rayet stars. Their surface abundances will reflect the extent of that mass loss and rotational mixing. Here, all of these compact progenitors were approximated by pure helium stars of constant mass. The structure and explosive characteristics of the PPI will not be greatly modified by changing the surface composition of the star, or by adding a low-mass extended envelope. Pulses in the lightest of these helium cores produced short, faint blue transients (Section 3.3, Figure 5) that ejected a small amount of mass and lasted only a week or so. Slightly heavier stars made SNe Ibn or SNe Icn as bright as a typical Type Ia, but with more structured, irregular, longer-lasting light curves. These light curves, produced by colliding shells, could have “tails” of a sort, especially if they interacted with prepulsational mass loss (not included here), but the explosions ejected no radioactivity. The colliding shells were usually more massive than an SN Ia and had less kinetic energy, so the velocities were slower. The colors were bluer, and the initial display from the matter ejected by the first pulse was faint.

Particularly intriguing are the helium cores between 52 and $62 M_{\odot}$ that give supernovae separated by long delays. Following an initial mass ejection that, if circumstellar interaction is ignored, is faint (Figure 7), the star becomes a “dormant supernova,” a compact star shining with approximately the Eddington luminosity (near $10^{40} \text{ erg s}^{-1}$), embedded in a supernova remnant. If there was prepulsational mass loss, the remnant could also be a bright radio or X-ray source. This dormant phase lasts from several years to several thousand years. Light from the central star is provided by its Kelvin–Helmholtz contraction and the accretion of matter that falls back from the first mass ejection. The latter may occur at an irregular rate, since the shells are not perfect spheres and produce some variability in the emission. Finally, just before the star truly dies, several pulses in rapid succession produce a bright optical display (Figures 5 and 6). These secondary light curves often exhibit a characteristic “double peak,” a rise to a ledge or first peak lasting 10–20 days, followed by a dramatic brightening to $\sim 10^{43} \text{ erg s}^{-1}$. This light curve morphology, as well as the color and multiple velocity components, resembles what was seen in SN 2005bf (Folatelli et al. 2006), and further study of this event as the possible explosion of a WN star of around $55 M_{\odot}$ is warranted (Section 3.3). The matter ejected by these final pulses will also interact for a long time afterward with the matter ejected by the first pulse, powering again a bright radio and X-ray source with, perhaps, some optical emission. The physical conditions and appearance might be similar to what is happening now in the rings of SN 1987A (Manchester et al. 2005; Helder et al. 2013; Zanardo et al. 2014).

Circumstellar interaction with a presupernova wind can complicate and enrich the possible outcomes of PPISN in all of the models. Consider, for example, the case of SN 2009ip, nominally a “supernova impostor” that only became a “real supernova” (of Type IIn) in 2012. The spectrum of the 2009 outburst showed hydrogen lines with a characteristic speed of 550 km s^{-1} , but with evidence for a high-velocity component

up to 3000–5000 km s^{−1} (Smith et al. 2010b) or even 7000 km s^{−1} (Foley et al. 2011). The peak luminosity in 2009 was $\sim 10^{41}$ erg s^{−1}, but in 2012, a second brighter outburst occurred. The second light curve had a ledge at 10^{41.5} erg s^{−1} that lasted for roughly a month, followed by a rapid rise to 10⁴³ erg s^{−1} (Fraser et al. 2015). Interaction continues today in SN 2009ip (Kiminki et al. 2016). Qualitatively at least, this history resembles what would be expected for a 52 M_{\odot} helium core blowing up inside a shell of preexplosive, hydrogen-rich mass loss with a mass loss rate of about $5 \times 10^{-4} M_{\odot}$ yr^{−1} and a characteristic wind speed of 500 km s^{−1} (Figures 5 and 21). The first mass ejection in Model He52 ejects 1.0 M_{\odot} with an energy of 7×10^{49} erg and a velocity that peaks at about 8000 km s^{−1} (average about 2500 km s^{−1}, but the highest speed would collide with the wind first). Interacting with the wind would give a peak luminosity of $\sim 10^{41}$ erg s^{−1}. Time structure could be added if the wind were clumpy or unsteady. In Model He52, 4.6 yr later, a second eruption makes the light curve in Figure 5 as two more shells collide. While He52 was a pure helium star and was incapable of making an SN II, similar dynamics would result for a WN star or a compact LBV with the same helium core mass. A slight change in core parameters might make a fainter first peak like for Model He58 in Figure 21. More study is warranted.

The study of bare helium cores also provides insight into the energetics and luminosity of the brightest Type I PPISN. In no case did the total kinetic energy in the pulses exceed 2.3×10^{51} erg, and this was for a rare case on the verge of becoming a PISN. A more common limit was 10⁵¹ erg, and that energy was shared among several pulses. Because of the low energies in individual pulses and the large masses ejected in the more energetic models, typical velocities are less than 4000 km s^{−1}, except in a small amount of material near the outer edge. These events might thus be classified as Type Ibn or Icn (Foley et al. 2007; Pastorello et al. 2008a, 2008b; Smith et al. 2012). Given that only a fraction of this energy can be converted to light, PPISN from compact progenitors should not exceed a few $\times 10^{50}$ erg. The brightest helium core explosions here (e.g., Models He48 and He50) radiated a total energy close to 1×10^{50} erg. This omits the considerable energy radiated by any star during the dormant stage and any interaction with preexplosive mass loss.

Stars that retain an appreciable hydrogen envelope, that is, a mass greater than the mass ejected by the first pulse in a bare helium core explosion, have different dynamics and light curves. Because the envelope tamps the expansion of the helium core, recurrence times can be shorter, and a greater fraction of kinetic energy is turned into light. The explosions can be more luminous. Two possibilities were explored: red supergiants (Section 4) and BSGs or LBVs (Section 6). For the physics assumed, hydrogenic stars with 10% solar metallicity most naturally ended their lives as RSGs. Only a fraction of their envelope was convective though, and throughout most of their mass and lifetimes, the stars with appreciable mass loss resembled BSGs. The final helium core mass for a given ZAMS mass did not vary greatly for a large range of mass loss rates, though the size of the CO core for a given helium core was slightly larger in these stars that retained envelopes. This affected the comparison between the results of helium cores evolved at constant mass and of full star models.

That part of the envelope contained in the surface convection zone of an RSG is very loosely bound and easily ejected. Even

a weak shock can eject a mass typical of an SN II. The velocity of the ejected matter, however, is very low, ~ 100 km s^{−1} in the lightest cases, so the transients for lowest-mass PPISN in stars with envelopes are long and faint and have low characteristic speeds (Figures 11 and 12). They would be classified as Type IIn. Discovering such events will be challenging though. Even at peak, they are only about 10 times brighter than the star that made them. They occur only at low metallicity, so they perhaps are far away and occur only in star-forming regions where other bright stars might be present.

PPISN happening in RSGs over 90 M_{\odot} are brighter and easier to discover, but could easily be confused with ordinary SNe IIP (Figures 13 and 15). The light curves from the heavier ones are distinctly overluminous and structured (Figure 16), but the duration, energetics, color, and luminosity are not out of bounds for what is observationally a diverse class anyway. In cases where the envelope mass is large, the light curves also last longer than is typical for Type IIP. Another discriminant might be the lack of a radioactive tail on the light curves. It may be difficult to distinguish a radioactivity-powered tail from circumstellar interaction though. For a presupernova mass loss rate of $10^{-4} M_{\odot}$ yr^{−1}, a shock speed of 5000 km s^{−1}, and a wind speed of 50 km s^{−1}, the contribution of circumstellar interaction to the luminosity would be $L_{\text{CSM}} \approx 0.5 \dot{M} v_{\text{shock}}^3 / v_{\text{wind}} = 8 \times 10^{40}$ erg s^{−1}. Given the uncertainty in late-time mass loss rates and wind speeds for presupernova stars, this could easily be an underestimate by 10 or more. Circumstellar interaction with presupernova mass loss was omitted here because of the uncertain parameters and a desire to highlight what the PPI, acting alone, would do.

Observationally, there is no clear evidence for an SN IIP with no tail. There are cases of faint supernovae with very faint tails, requiring as little as 0.005 M_{\odot} of ⁵⁶Ni for their explanation (see Table 6 of Pejcha & Prieto 2015), but these are probably the neutrino-powered explosions of lower-mass stars. An interesting case is supernova LSQ13fn (Polshaw et al. 2016). This unusual event resembles Model T90A (Figure 15). It had about the same luminosity, a duration longer than most SNe IIP (though somewhat less than T90), and an unusually slow velocity, and it exhibited a dramatic drop to an unresolved tail and was inferred, spectroscopically, to have low metallicity. Further modeling of this specific event might be desirable.

For main-sequence masses above about 100 M_{\odot} , the interval between pulses becomes longer than the duration of any single event, and there can be multiple supernovae and dormant supernovae. If the star is an RSG, the first event resembles a normal Type IIP as the envelope is ejected, but the later displays powered by colliding shells can be especially bright and long lasting and have multiple maxima. The brightest supernovae from PPISN are produced by secondary pulses in the 100–130 M_{\odot} mass range. Activity there can continue for years (Section 4.4, Figures 17 and 18), centuries (Figure 27), or even millennia (Figure 19). Typically, these explosions have only one or two violent episodes of pulsing activity after the first pulse ejects the envelope. Structure is added to the light curves by the collision of thin high-density shells resulting from reverse shocks. These shells are artificially thin in 1D calculations and, in addition to causing unrealistic short excursions to very high luminosity, pose computational difficulties. Further two-dimensional studies that include radiation transport are needed to properly simulate the mixing that goes on and the modification to the light curve. Until

such calculations have been done, a more realistic prediction would come from drawing the best smooth line through the calculated light curve. The smoothing length $\Delta t/t$ is set by the degree to which the shells are spread by mixing and might be $\Delta r/R \sim 10\%-20\%$ (Chen et al. 2014, 2016). The smoothing should preserve energy emitted, that is, the area under the curve.

A potential observational counterpart to explosions in this $100\text{--}130 M_{\odot}$ range is SN 2008iy, an exceptionally luminous SNe IIn with a very long rise time of 400 days that showed evidence for a major mass loss about 55 yr before (Miller et al. 2010). Compare this with the second outburst in Model T125A in Figure 27, which took place 70 yr after the first pulse ejected $23.5 M_{\odot}$. The rise time from $5 \times 10^{41} \text{ erg s}^{-1}$ to a peak of $4 \times 10^{42} \text{ erg s}^{-1}$ in Model T125A was only about 200 days and the peak luminosity half that of SN 2009iy, but the width of shells is very uncertain in these 1D models, and the masses and speeds are model sensitive. Perhaps more problematic for any collisional model is that the collision takes place in an optically thin medium, and it is not obvious that most of the power would come out as optical light.

The light curves and, to a lesser extent, the dynamics of PPISN will be different if the presupernova star is a BSG or an LBV (Section 6) rather than an RSG. The blue progenitors here had properties that overlapped with both BSGs and LBVs. Envelopes of approximately 5, 10, and $20 M_{\odot}$ (Table 4) had radii of a few $\times 10^{12} \text{ cm}$ and effective temperatures of 25,000–50,000 K. Because of the lack of weakly bound matter in the convective RSG envelope, the threshold for making faint supernovae was increased to above $80 M_{\odot}$. The smaller initial radius of blue progenitors also made the initial display much fainter. Apart from affecting the lighter, fainter events and the light curve resulting from the first pulse, blue progenitors in the more massive stars resembled their RSG counterparts. Compare, for example, Models T110B and B110 in Figures 17, 20, and 21. Some variation in shell mass and thickness is expected, but the duration, interval, peak brightness, and structures are qualitatively similar, especially if the sharp time structure in T110B is smoothed.

Some of the prompt light curves of the blue progenitors are especially interesting though, given both the lack of any compelling evidence for RSGs at such high masses, regardless of metallicity, and observations of supernovae that resemble the models. SN 2005gl (Gal-Yam & Leonard 2009), for example, had a roughly month-long “precursor” at $\sim 10^{41} \text{ erg s}^{-1}$ before abruptly rising to a peak luminosity of $5 \times 10^{42} \text{ erg s}^{-1}$. Compare that with the models in Figure 21. Gal-Yam et al. estimated that a mass of only $\sim 0.01 M_{\odot}$ was necessary to power the light curve at peak, but this estimate overlooks the velocity gradient in the ejected matter. The mass could be several solar masses, but the maximum luminosity comes from interacting with only the innermost, slowest moving, highest density part of that shell. A similar dramatic rise from a faint initial outburst was seen in SN 1961v (Kochanek et al. 2011; Smith et al. 2011), SN 2010mc (Ofek et al. 2013), the 2012 outburst of SN 2009ip (Fraser et al. 2015), and SN 2015bh (Elias-Rosa et al. 2016). There is also some evidence that these events came from the explosion of very massive stars (Foley et al. 2011) and, at least in the case of 2009ip, that the star was an LBV. Strong radio and X-ray emission has continued for years after the 2012 explosion of SN 2009ip (Smith et al. 2016). These light curves with ledges and second peaks are also similar to the previously mentioned Type Icn SN 2005bf,

and one cannot help but feel that PPISN are responsible for at least some events with this double-peaked morphology. Further detailed study of individual events is clearly warranted. On the more negative side though, all of the blue models that produced these interesting initial displays became bright supernovae again shortly afterward. It seems doubtful that these subsequent events would have been missed. Some of the *later* explosions (Figure 22) also exhibit double maxima, however, and there the converse problem arises from hiding an *earlier* supernova.

There is also substantial observational evidence for other explosions in LBVs producing SNe IIn from one to several years after a major mass ejection. SNe 2006aa, 2006jd, 2006qq, and 2008fq may be examples (Taddia et al. 2013). Compare with Models B110 and B115 (Figure 22). SN 1994W, a Type IIn, also ejected a circumstellar shell 1.5 yr before explosion. The interaction there produced a luminosity of $10^{43} \text{ erg s}^{-1}$ at about 10^{15} cm (Chugai et al. 2004; Kiewe et al. 2012). SN 2015U lost of order of a solar mass during the last few years before exploding (Shivvers et al. 2016). It is unlikely that all these events were PPISN, but further individual study could be warranted.

Hydrogenic stars above $120 M_{\odot}$ produce some interesting transients that may not all be particularly optically bright (Section 4.5). The star’s core survives hundreds to thousands of years after the first mass ejection, mostly in a dormant state, but occasionally experiencing additional pulsational mass ejection. These ejections collide with previously ejected shells at such large radii ($> 10^{16} \text{ cm}$) that the display lasts a long time and is optically thin to electron scattering. Radiative powers are $\sim 10^{40} - 10^{41} \text{ erg s}^{-1}$. These might resemble what is happening now as the supernova collides with its ring in SN 1987A (Larsson et al. 2011) and SN 2009ip (Smith et al. 2016). Another feature is the dormant central star itself, shining with a luminosity of about $10^{40} \text{ erg s}^{-1}$ and a hot spectrum.

A possible example of a dormant PPISN could be Eta Carinae (Section 9), though the high metallicity, gross asymmetry, and long history of recurrent faint outbursts (Kiminki et al. 2016) argue against such an interpretation. If a PPISN, Eta Carinae is best modeled as a star near $125 M_{\odot}$ on the main sequence. Near death, the helium core mass was $57 \pm 2 M_{\odot}$. A residual core of $50\text{--}60 M_{\odot}$ has survived previous outbursts (Table 6) and is currently radiating near its Eddington luminosity. This star would resemble an ordinary massive Wolf-Rayet star, but perhaps with an extended atmosphere from the fallback of previous explosions and a wind. In order that the event has a timescale of centuries, a PPISN explanation requires that the total kinetic energy be closer to 10^{51} erg than the previously claimed 10^{50} erg . The unusual asymmetry of the object is not explained in this model, but might involve interaction with its binary companion.

A possible problem with this speculation is that the first pulse and envelope ejection should have produced a supernova that was brighter than was seen in the 1830s. This could be alleviated, in part, if the progenitor was a compact blue star and not an RSG. The luminosity from the first pulse of Model B120 (not illustrated) was only a few times $10^{41} \text{ erg s}^{-1}$ after the first week (and the bolometric correction was large during that first week). Or the first pulse may actually have happened several centuries earlier, and the supernova it produced, despite being bright for several months, was not recorded in the southern hemisphere where it was visible. The second pulse, happening in the 1830s, would then be responsible for the Great Eruption.

Eta Carinae would then have had two outbursts in the past but, unfortunately, not three as inferred by Kiminki et al. (2016). If this speculative scenario is valid, Eta Carinae should transition into a black hole in the next few millennia (Table 6). The PPI seems unlikely to explain all of the complex history of Eta Carinae, but it could be playing a partial role, and further study is definitely warranted.

Part of the motivation for this study was the hope that PPISN would provide a robust explanation for SLSN (Woosley et al. 2007). The results here confirm that the colliding shells made by PPISN can indeed make supernovae that are very bright for extended periods (e.g., Figures 5, 16, 18, 19, and 20), but none approach the level of, for example, SN 2003ma, which may have emitted 3.6×10^{51} erg of light (Rest et al. 2011). The most luminous events here, T120 (Figure 18) and T130 (Figure 19), emitted less than 5×10^{50} erg and only briefly exceeded 10^{44} erg s⁻¹. Most models emitted less than 10^{50} erg. While not all possibilities have been explored, it seems unlikely that thermonuclear PPISN, unassisted, can explain the integrated light of events like SN 2006gy (2.4×10^{51} erg of light; Smith et al. 2010a), SN 2005ap (1.7×10^{51} erg of light; Quimby et al. 2011), and SN 2008es (1.1×10^{51} erg of light; Miller et al. 2009). This is disappointing. SN 2006gy was the first PPISN identification suggested in the literature (Woosley et al. 2007). Later, Smith et al. (2010a) showed that this event required a kinetic energy of 5×10^{51} erg, which may be just out of reach. Indeed, Woosley et al. had to artificially enhance the collision velocity by a factor of 2 (and hence the explosion energy by a factor of 4) in their model in order to get a good fit to the light curve. Further study, especially of 2006gy, is certainly needed.

A more energetic outcome is possible if, contrary to current opinion, the helium and heavy element core of these very massive stars does not go quietly into a black hole (see also Yoshida et al. 2016). The observation of gravitational radiation from two merging black holes with masses 29 and 36 M_{\odot} shows that PPISN of moderate metallicity do frequently make black holes (Woosley 2016), but collapse to a black hole does not necessarily exclude making a supernova. The rotation rates of the iron cores for the rotating models here are large (Section 7, Table 5), corresponding to a cold pulsar rotation period of 2–3 ms for stars with hydrogenic envelopes and possibly faster for CHE. These periods imply rotational energies up to $\sim 4 \times 10^{51}$ erg for stars with envelopes and $\sim 2 \times 10^{52}$ erg for CHE. Much more work is needed to determine the outcome here. Are there jets? What is their energy? Are they broad or narrow? Does a neutron star survive?

Lacking adequate theoretical guidance, the effect of very energetic central explosions happening at the time of iron core collapse in PPISN was explored in a parametric way (Section 8). The most interesting cases had pulses that ejected many solar masses approximately one year before collapse. Helium cores near $50 M_{\odot}$ had pulsing activity that spanned about one year and were candidates. Some heavier stars also had late-stage pulsations that lasted months to years after previously ejecting their hydrogen envelopes centuries or more before. The collision of the rapidly expanding core with the massive shell at 10^{15} – 10^{16} cm produced very luminous supernovae potentially capable of explaining even the brightest SLSN (Figures 24, 25). For “moderate” kinetic energies of a few $\times 10^{51}$ erg (plus the nontrivial binding energy of the

disrupted star), large amounts of matter fell back, and the final remnant was a black hole. For more energetic explosions, $\sim 2 \times 10^{52}$ erg, the light curves were brighter, no matter fell back, and up to several solar masses of ^{56}Ni were ejected. Even this large amount of nickel had no effect on the light curve. The results of 10^{52} erg explosions in stars that retain extended hydrogenic envelopes should be treated with special caution though. Not only is the explosion mechanism unspecified, but retaining so much rotation in the core of a giant star has been an enduring theoretical problem in the context of GRB models and may be why GRBs are associated with SNe I and not Type II. Be that as it may, the brightest explosions, and the only ones producing over a few times 10^{51} erg of light, required a very massive shell for the impact, that is, the hydrogen-rich envelope of the presupernova star, and thus would be SNe IIn. Somewhat more realistic models derived from CHE that avoided ever becoming giants gave SNe I that radiated up to $\sim 2 \times 10^{51}$ erg. If these MHD explosions in PPISN exist, they would be close cousins to GRBs, but lacking in their final ejecta any strong relativistic component.

It has been known for some time that normal PISN leave no bound remnants. A helium core over $133 M_{\odot}$ is required for the direct production of a black hole, and for some range of masses below that no black hole is made, but how far down in mass does this void extend? This study answers that question (Section 10; see also Woosley et al. 2007; Woosley & Heger 2015a, p. 199). PISN will occur down to helium core masses of about $64 M_{\odot}$, but the PPI will eject any mass in excess of $52 M_{\odot}$ (Tables 1, 2, and 5). A generation of bare helium cores or of CHE models that managed to span all masses at death would not produce any black holes between 52 and $133 M_{\odot}$. But what about lighter stars that retained some hydrogen envelope? There the answer is more nuanced and depends upon the mass loss history of the star. Consider Model T70B (Table 2), for example, which has a helium core of $30.5 M_{\odot}$ when it dies and thus avoids the PPI. Will only the helium core collapse to a black hole, or will the hydrogen envelope also participate in the collapse? If the envelope collapses and there has been no mass loss, a black hole of $70 M_{\odot}$ could result.

If the mass loss rate (i.e., metallicity) is high enough, then the envelope will have little or no mass and the $52 M_{\odot}$ limit will not be violated. If late-time mass ejection removes the envelope (Weinberg & Quataert 2008; Lovegrove & Woosley 2013), the limit will also hold. More importantly, since black hole mass determinations, including those from gravitational radiation, come from interacting binaries, a companion star may have robbed the PPI candidate of its envelope, perhaps through common envelope evolution. Systems that produce binary black holes that must merge in a Hubble time by emitting gravitational radiation do not accommodate RSGs, BSGs, or even LBVs in their final stages (Peters 1964; S. de Mink 2017, private communication). Either the envelope is removed through common envelope evolution or it never was there (CHE). So if the black hole pairs seen in gravitational radiation experiments have been produced by the evolution of a single stellar system and not, for example, by dynamical merger in a dense cluster, they will exhibit the predicted gap from 52 to $133 M_{\odot}$. In reality, since $133 M_{\odot}$ helium cores require extremely massive stars for their production ($260 M_{\odot}$?), the “gap” will probably be seen as a “cutoff” above which no black holes are found in merging systems.

In addition to limiting the range of black hole masses that exist in nature, the present study also limits the mass of ^{56}Ni ejected in a core-collapse supernova. As Tables 1 and 2 show, there can be no CO core mass bigger than $51 M_{\odot}$ at the time of iron core collapse, even in stars that avoid the PPI, that is, the minimum of M_{preSN} and M_{final} . Most likely these cores collapse to black holes, but even if they are artificially exploded with very high energy, the ^{56}Ni production is limited. Model He50, with a CO core of $42 M_{\odot}$ exploded with a central energy deposition of 2.6×10^{52} erg (Figure 25), only made $2.7 M_{\odot}$ of ^{56}Ni . It thus seems unlikely that credible models can produce more than about $4 M_{\odot}$ of ^{56}Ni without encountering the PPI and shrinking in mass first (though see Umeda & Nomoto 2008).

Since the matter ejected in PPISN experiences no explosive nuclear processing, the nucleosynthetic yields are the same as if, toward the end of its life, the star had very rapid mass loss. Assuming the collapse of the entire core to a black hole, most of the elements heavier than magnesium, and all appreciable radioactivities, are lost. The nucleosynthesis for a representative set of nonrotating models is given in Table 7 and shows the appreciable nucleosynthesis of helium and CNO, with traces of neon and magnesium. One has to go to a full PISN before the ejection of intermediate-mass elements competes in solar proportions with oxygen, and even then very little iron-group elements are made until the star's helium core exceeds about $90 M_{\odot}$ (stellar mass about $190 M_{\odot}$). At very low metallicity, rotating models may also copiously produce primary ^{14}N (Meynet & Maeder 2002; Heger & Woosley 2011; Yoon et al. 2012). A first generation of such stars might thus contribute a composition rich in either CO or CNO, with a trace of neon and magnesium and very little silicon and iron (Woosley & Heger 2015a, p. 199). Stars with this sort of composition have been seen (Frebel et al. 2005; Keller et al. 2014). Given that a single one of the more massive stars discussed here could produce, for example, 1% solar oxygen for thousands of solar masses of second-generation stars, the nucleosynthetic role of Pop III PPISN deserves greater attention. This is also an interesting topic for future work.

This work, which spanned many years, has profited from conversations with many people, especially Alex Heger, Nathan Smith, Jorick Vink, Selma de Mink, and Thomas Janka. Alex Heger also contributed important parts of the KEPLER code that were necessary to this study, such as the physics used in the rotating models, the adaptive network for nuclear burning, and many other features that made the code easier to use and the results easier to analyze. Early on, the research was supported by the NSF (ARRA AST-0909129) and by NASA (NNX09AK36G). More recently it has been supported solely by NASA (NNX14AH34G).

References

- Abbott, B. P., Abbott, R., Abbott, T. D., et al. 2016a, *ApJL*, **818**, L22
 Abbott, B. P., Abbott, R., Abbott, T. D., et al. 2016b, *PhRvL*, **116**, 061102
 Akiyama, S., Wheeler, J. C., Meier, D. L., & Lichtenstadt, I. 2003, *ApJ*, **584**, 954
 Ardeljan, N. V., Bisnovatyi-Kogan, G. S., & Moiseenko, S. G. 2005, *MNRAS*, **359**, 333
 Barkat, Z., Rakavy, G., & Sack, N. 1967, *PhRvL*, **18**, 379
 Bestenlehner, J. M., Gräfener, G., Vink, J. S., et al. 2014, *A&A*, **570**, A38
 Blinnikov, S. I. 2010, *PAN*, **73**, 604
 Bond, J. R., Arnett, W. D., & Carr, B. J. 1984, *ApJ*, **280**, 825
 Brott, I., Mink, S. E., Cantiello, M., et al. 2011, *A&A*, **530**, 115
 Buchmann, L. 1996, *ApJL*, **468**, L127
 Burrows, A., Dessart, L., Livne, E., Ott, C. D., & Murphy, J. 2007, *ApJ*, **664**, 416
 Chatzopoulos, E., & Wheeler, J. C. 2012, *ApJ*, **748**, 42
 Chatzopoulos, E., Wheeler, J. C., Viko, J., et al. 2016, *ApJ*, **828**, 94
 Chen, K.-J., Woosley, S., Heger, A., Almgren, A., & Whalen, D. J. 2014, *ApJ*, **792**, 28
 Chen, K.-J., Woosley, S. E., & Sukhbold, T. 2016, *ApJ*, **832**, 73
 Chen, Y., Bressan, A., Girardi, L., et al. 2015, *MNRAS*, **452**, 1068
 Chevalier, R. A. 1982, *ApJ*, **259**, 302
 Chevalier, R. A., & Irwin, C. M. 2012, *ApJL*, **747**, L17
 Chugai, N. N., Blinnikov, S. I., Cumming, R. J., et al. 2004, *MNRAS*, **352**, 1213
 Damineli, A., Hillier, D. J., Corcoran, M. F., et al. 2008, *MNRAS*, **384**, 1649
 Davidson, K., & Humphreys, R. M. 1997, *ARA&A*, **35**, 1
 de Koter, A., Min, M., van Boekel, R., & Chesneau, O. 2005, in ASP Conf. Series 332, The Fate of the Most Massive Stars, ed. R. Humphreys & K. Stanek (San Francisco, CA: ASP), 313
 Dessart, L., Burrows, A., Livne, E., & Ott, C. D. 2008, *ApJL*, **673**, L43
 Dessart, L., Hillier, D. J., Audit, E., Livne, E., & Waldman, R. 2016, *MNRAS*, **458**, 2094
 Eastman, R. G., Woosley, S. E., Weaver, T. A., & Pinto, P. A. 1994, *ApJ*, **430**, 300
 Ekström, S., Georgy, C., Eggenberger, P., et al. 2012, *A&A*, **537**, A146
 Elias-Rosa, N., Pastorello, A., Benetti, S., et al. 2016, *MNRAS*, **463**, 3894
 Folatelli, G., Contreras, C., Phillips, M. M., et al. 2006, *ApJ*, **641**, 1039
 Foley, R. J., Berger, E., Fox, O., et al. 2011, *ApJ*, **732**, 32
 Foley, R. J., Smith, N., Ganeshalingam, M., et al. 2007, *ApJL*, **657**, L105
 Fowler, W. A., & Hoyle, F. 1964, *ApJS*, **9**, 201
 Fraser, M., Kotak, R., Pastorello, A., et al. 2015, *MNRAS*, **453**, 3886
 Frebel, A., Aoki, W., Christlieb, N., et al. 2005, *Natur*, **434**, 871
 Fryer, C. L. 1999, *ApJ*, **522**, 413
 Fryer, C. L., & Kalogera, V. 2001, *ApJ*, **554**, 548
 Gal-Yam, A., & Leonard, D. C. 2009, *Natur*, **458**, 865
 Georgy, C., Ekström, S., Eggenberger, P., et al. 2013, *A&A*, **558**, A103
 Glatzel, W., Fricke, K. J., & El Eid, M. F. 1985, *A&A*, **149**, 413
 Groenewegen, M. A. T., Sloan, G. C., Soszyński, I., & Petersen, E. A. 2009, *A&A*, **506**, 1277
 Heger, A., Langer, N., & Woosley, S. E. 2000, *ApJ*, **528**, 368
 Heger, A., & Woosley, S. E. 2002, *ApJ*, **567**, 532
 Heger, A., & Woosley, S. E. 2011, *ApJ*, **724**, 341
 Heger, A., Woosley, S. E., & Spruit, H. C. 2005, *ApJ*, **626**, 350
 Helder, E. A., Broos, P. S., Dewey, D., et al. 2013, *ApJ*, **764**, 11
 Herant, M., & Woosley, S. E. 1994, *ApJ*, **425**, 814
 Hillier, D. J., Davidson, K., Ishibashi, K., & Gull, T. 2001, *ApJ*, **553**, 837
 Humphreys, R. M., & Davidson, K. 1979, *ApJ*, **232**, 409
 Iglesias, C. A., & Rogers, F. J. 1996, *ApJ*, **464**, 943
 Inserra, C., Smartt, S. J., Jerkstrand, A., et al. 2013, *ApJ*, **770**, 128
 Kasen, D., & Bildsten, L. 2010, *ApJ*, **717**, 245
 Kasen, D., Woosley, S. E., & Heger, A. 2011, *ApJ*, **734**, 102
 Keller, S. C., Bessell, M. S., Frebel, A., et al. 2014, *Natur*, **506**, 463
 Kiewe, M., Gal-Yam, A., Arcavi, I., et al. 2012, *ApJ*, **744**, 10
 Kiminki, M. M., Reiter, M., & Smith, N. 2016, *MNRAS*, **463**, 845
 Kochanek, C. S., Szczygiel, D. M., & Stanek, K. Z. 2011, *ApJ*, **737**, 76
 Langer, N., Norman, C. A., de Koter, A., et al. 2007, *A&A*, **475**, L19
 Larsson, J., Fransson, C., Östlin, G., et al. 2011, *Natur*, **474**, 484
 Lattimer, J. M., & Prakash, M. 2007, *PhR*, **442**, 109
 LeBlanc, J. M., & Wilson, J. R. 1970, *ApJ*, **161**, 541
 Levesque, E. M., Massey, P., Olsen, K. A. G., & Plez, B. 2007, *ApJ*, **667**, 202
 Lovegrove, E., & Woosley, S. E. 2013, *ApJ*, **769**, 109
 Lovegrove, E., Woosley, S. E., & Zhang, W. 2017, *ApJ*, submitted
 Madura, T. I., Gull, T. R., Owocki, S. P., et al. 2012, *MNRAS*, **420**, 2064
 Manchester, R. N., Gaensler, B. M., Staveley-Smith, L., Kesteven, M. J., & Tzioumis, A. K. 2005, *ApJL*, **628**, L131
 Mandel, I., & de Mink, S. E. 2016, *MNRAS*, **458**, 2634
 Massey, P., & Olsen, K. A. G. 2003, *AJ*, **126**, 2867
 Matheson, T., Filippenko, A. V., Chornock, R., Leonard, D. C., & Li, W. 2000, *AJ*, **119**, 2303
 Mauerhan, J. C., Smith, N., Filippenko, A. V., et al. 2013, *MNRAS*, **430**, 1801
 Mauron, N., & Josselin, E. 2011, *A&A*, **526**, A156
 Mazzali, P. A., McFadyen, A. I., Woosley, S. E., Pian, E., & Tanaka, M. 2014, *MNRAS*, **443**, 67
 Meier, D. L., Epstein, R. I., Arnett, W. D., & Schramm, D. N. 1976, *ApJ*, **204**, 869
 Metzger, B. D., Giannios, D., Thompson, T. A., Bucciantini, N., & Quataert, E. 2011, *MNRAS*, **413**, 2031
 Meunier, C., Bauer, F. E., Dwarkadas, V. V., et al. 2013, *MNRAS*, **431**, 2453

- Meynet, G., & Maeder, A. 2002, *A&A*, **390**, 561
- Milisavljevic, D., Margutti, R., Kamble, A., et al. 2015, *ApJ*, **815**, 120
- Miller, A. A., Chornock, R., Perley, D. A., et al. 2009, *ApJ*, **690**, 1303
- Miller, A. A., Silverman, J. M., Butler, N. R., et al. 2010, *MNRAS*, **404**, 305
- Moriya, T. J., Blinnikov, S. I., Tominaga, N., et al. 2013, *MNRAS*, **428**, 1020
- Morris, T., & Podsiadlowski, P. 2009, *MNRAS*, **399**, 515
- Mösta, P., Ott, C. D., Radice, D., et al. 2015, *Natur*, **528**, 376
- Mösta, P., Richers, S., Ott, C. D., et al. 2014, *ApJL*, **785**, L29
- Müller, E., & Hillebrandt, W. 1979, *A&A*, **80**, 147
- Müller, P. E., & Vink, J. S. 2008, *A&A*, **492**, 493
- Muno, M. P., Clark, J. S., Crowther, P. A., et al. 2006, *ApJL*, **636**, L41
- Nieuwenhuijzen, H., & de Jager, C. 1990, *A&A*, **231**, 134
- Nordhaus, J., & Blackman, E. G. 2006, *MNRAS*, **370**, 2004
- Ober, W. W., El Eid, M. F., & Fricke, K. J. 1983, *A&A*, **119**, 61
- O'Connor, E., & Ott, C. D. 2011, *ApJ*, **730**, 70
- Ofek, E. O., Sullivan, M., Cenko, S. B., et al. 2013, *Natur*, **494**, 65
- Owocki, S. P. 2015, in *Astrophysics and Space Science Library*, Vol. 412, Very Massive Stars in the Local Universe, Vol. 412, ed. J. S. Vink (Cham: Springer), 113
- Parkin, E. R., Pittard, J. M., Corcoran, M. F., & Hamaguchi, K. 2011, *ApJ*, **726**, 105
- Pastorello, A., Benetti, S., Brown, P. J., et al. 2015a, *MNRAS*, **449**, 1921
- Pastorello, A., Mattila, S., Zampieri, L., et al. 2008a, *MNRAS*, **389**, 113
- Pastorello, A., Prieto, J. L., Elias-Rosa, N., et al. 2015b, *MNRAS*, **453**, 3649
- Pastorello, A., Quimby, R. M., Smartt, S. J., et al. 2008b, *MNRAS*, **389**, 131
- Pastorello, A., Smartt, S. J., Mattila, S., et al. 2007, *Natur*, **447**, 829
- Pejcha, O., & Prieto, J. L. 2015, *ApJ*, **799**, 215
- Pejcha, O., & Thompson, T. A. 2015, *ApJ*, **801**, 90
- Peters, P. C. 1964, *PhRv*, **136**, 1224
- Petrov, B., Vink, J. S., & Gräfener, G. 2016, *MNRAS*, **458**, 1999
- Polshaw, J., Kotak, R., Dessart, L., et al. 2016, *A&A*, **588**, A1
- Quimby, R. M., Kulkarni, S. R., Kasliwal, M. M., et al. 2011, *Natur*, **474**, 487
- Rakavy, G., & Shaviv, G. 1967, *ApJ*, **148**, 803
- Rest, A., Foley, R. J., Gezari, S., et al. 2011, *ApJ*, **729**, 88
- Rogers, F. J., & Iglesias, C. A. 1992, *ApJS*, **79**, 507
- Sanyal, D., Grassitelli, L., Langer, N., & Bestenlehner, J. M. 2015, *A&A*, **580**, A20
- Scannapieco, E., Madau, P., Woosley, S., Heger, A., & Ferrara, A. 2005, *ApJ*, **633**, 1031
- Shivvers, I., Zheng, W. K., Mauerhan, J., et al. 2016, *MNRAS*, **461**, 3057
- Smith, N. 2006, *ApJ*, **644**, 1151
- Smith, N. 2008, *Natur*, **455**, 201
- Smith, N. 2011, *MNRAS*, **415**, 2020
- Smith, N. 2013, *MNRAS*, **429**, 2366
- Smith, N., Andrews, J. E., & Mauerhan, J. C. 2016, *MNRAS*, **463**, 2904
- Smith, N., Chornock, R., Silverman, J. M., Filippenko, A. V., & Foley, R. J. 2010, *ApJ*, **709**, 856
- Smith, N., & Frew, D. J. 2011, *MNRAS*, **415**, 2009
- Smith, N., Gehrz, R. D., Hinz, P. M., et al. 2003, *AJ*, **125**, 1458
- Smith, N., Li, W., Foley, R. J., et al. 2007, *ApJ*, **666**, 1116
- Smith, N., Li, W., Silverman, J. M., Ganeshalingam, M., & Filippenko, A. V. 2011, *MNRAS*, **415**, 773
- Smith, N., Mauerhan, J. C., Silverman, J. M., et al. 2012, *MNRAS*, **426**, 1905
- Smith, N., Miller, A., Li, W., et al. 2010, *AJ*, **139**, 1451
- Smith, N., & Owocki, S. 2006, *ApJL*, **645**, L45
- Spera, M., Mapelli, M., & Bressan, A. 2015, *MNRAS*, **451**, 4086
- Sugerman, B. E. K., Crotts, A. P. S., Kunkel, W. E., Heathcote, S. R., & Lawrence, S. S. 2005, *ApJS*, **159**, 60
- Sukhbold, T., Ertl, T., Woosley, S. E., Brown, J. M., & Janka, H.-T. 2016, *ApJ*, **821**, 38
- Sukhbold, T., & Woosley, S. E. 2016, *ApJL*, **820**, L38
- Svirski, G., Nakar, E., & Sari, R. 2012, *ApJ*, **759**, 108
- Taddia, F., Stritzinger, M. D., Sollerman, J., et al. 2013, *A&A*, **555**, A10
- Takiwaki, T., & Kotake, K. 2011, *ApJ*, **743**, 30
- Ugliano, M., Janka, H.-T., Marek, A., & Arcones, A. 2012, *ApJ*, **757**, 69
- Umeda, H., & Nomoto, K. 2002, *ApJ*, **565**, 385
- Umeda, H., & Nomoto, K. 2008, *ApJ*, **673**, 1014
- Usov, V. V. 1992, *Natur*, **357**, 472
- Vink, J. S., & de Koter, A. 2005, *A&A*, **442**, 587
- Vink, J. S., de Koter, A., & Lamers, H. J. G. L. M. 2001, *A&A*, **369**, 574
- Vink, J. S., Muijres, L. E., Anthonisse, B., et al. 2011, *A&A*, **531**, A132
- Voors, R. H. M., Waters, L. B. F. M., de Koter, A., et al. 2000, *A&A*, **356**, 501
- Walborn, N. R., Blanco, B. M., & Thackeray, A. D. 1978, *ApJ*, **219**, 498
- Weaver, T. A., & Woosley, S. E. 1993, *PhR*, **227**, 65
- Weaver, T. A., Zimmerman, G. B., & Woosley, S. E. 1978, *ApJ*, **225**, 1021
- Weinberg, N. N., & Quataert, E. 2008, *MNRAS*, **387**, L64
- Wilson, J. R., Mayle, R., Woosley, S. E., & Weaver, T. 1986, *NYASA*, **470**, 267
- Woosley, S. E. 1993, *ApJ*, **405**, 273
- Woosley, S. E. 2010, *ApJL*, **719**, L204
- Woosley, S. E. 2016, *ApJL*, **824**, L10
- Woosley, S. E., Blinnikov, S., & Heger, A. 2007, *Natur*, **450**, 390
- Woosley, S. E., & Heger, A. 2006, *ApJ*, **637**, 914
- Woosley, S. E., & Heger, A. 2007, *PhR*, **442**, 269
- Woosley, S. E., & Heger, A. 2015a, in *Astrophysics and Space Science Library*, Vol. 412, Very Massive Stars in the Local Universe, ed. J. S. Vink (Cham: Springer), 199
- Woosley, S. E., & Heger, A. 2015b, *ApJ*, **810**, 34
- Woosley, S. E., Heger, A., & Weaver, T. A. 2002, *RvMP*, **74**, 1015
- Woosley, S. E., & Weaver, T. A. 1986, in *IAU Coll. 89, Radiation Hydrodynamics in Stars and Compact Objects*, ed. D. Mihalas & K.-H. A. Winkler (Berlin: Springer), 91
- Yoon, S.-C., Dierks, A., & Langer, N. 2012, *A&A*, **542**, A113
- Yoon, S.-C., & Langer, N. 2005, *A&A*, **443**, 643
- Yoshida, T., Umeda, H., Maeda, K., & Ishii, T. 2016, *MNRAS*, **457**, 351
- Yusof, N., Hirschi, R., Meynet, G., et al. 2013, *MNRAS*, **433**, 1114
- Zanardo, G., Staveley-Smith, L., Indebetouw, R., et al. 2014, *ApJ*, **796**, 82